國立交通大學

應用化學研究所

博士論文

多層化結構高分子薄膜之製備與特性分析之研究

A Study on Preparation and Characteristics of Laminar Polymeric Film

研究生：黃啟賢

指導教授：吳建興 教授

共同指導教授：黃俊欽 教授

中 華 民 國 九 十 三 年 五 月

Abstract (in English)

Laminar polymeric films are usually fabricated by coextrusion and blending processes. In a coextrusion process, a laminar polymeric film is formed into multilayer and parallel structures. In a blending process, on the other hand, the laminar polymeric film formed has laminar morphology of dispersed phases in its blend film. Because of the wide range of applications of laminar polymeric films as packaging materials, studies of the processes for forming, and the characteristics of, laminar polymeric films have become increasingly important. In this study, the aims are to predict the properties of the multilayer film and investigate the effect of adhesive on the laminar polymeric film.

In Chapters 2 and 3, we successfully fabricated three-layer (A/B/C) films, comprising high-density polyethylene (HDPE), tie layer [high-density polyethylene-grafted maleic anhydride (HDPE-g-MAH]], and polyamide-6 (PA-6), by a coextrusion blown-film process. The tensile behavior of the three-layer film can also be predicted from its component layers by using an additive rule and an empirical constitutive equation — $\sigma_T = K \cdot \exp\left(\dfrac{\gamma_\varepsilon}{2} \cdot \varepsilon_T{}^2\right) \cdot \dot{\varepsilon}_T{}^m$, where σ_T, ε_T, and $\dot{\varepsilon}_T$ are the true stress, the true strain, and the true strain rate, respectively, K and γ_ε are constants, and m is the strain rate sensitivity — and a simplified constitutive equation — $\sigma_T = \sigma_0 \exp(\gamma \cdot \varepsilon_T)$, where ε_T, σ_0, and γ are the true strain, true yield stress and the strain hardening parameter, respectively — over the range of plastic deformation. There exists a good agreement between the experimental and predicted data at low crosshead speeds, but there is a relatively large discrepancy between them at high speeds, for both constitutive equations, because of the heat generated during

deformation. The valid strain range for the latter is smaller, however, than that for the former. On the other hand, the series model was examined to predict permeability of HDPE/tie/PA-6 three-layer film; there exists a good agreement between experimental data and this model for predicting both gas and water vapor permeabilities of three-layer films containing various volume fractions of PA-6.

Conventionally, one or more tie layers are used in coextrusion processes, e.g., in the preparation of HDPE/tie/PA-6 mentioned above, but having additional tie layers in a coextruded film makes the fabrication process more complex and expensive. To eliminate the need for tie layer(s) and to reduce the number of layers, we have also successfully fabricated three-layer (A/B/A) films, comprising a varying content of ethylene–vinyl alcohol copolymer (EVOH) as the internal layer and blends of low-density polyethylene (LDPE) and adhesive [low-density ethylene grafted with maleic anhydride (LDPE-g-MAH]] as the external layers, by a coextrusion blown-film process. In Chapter 4 ,we describe our investigation of the mechanical properties and compare their oxygen and water vapor permeabilities to a series model reflecting the content of adhesive. The peel strength increased sharply at LDPE-g-MAH content > 12.5 wt%; we associate this increase with a promotion of adhesion between layers that arises from the formation of ester bonds, as determined by FTIR spectroscopy, between EVOH and LDPE-g-MAH. The tensile strength did not change significantly upon increasing the LDPE-g-MAH content, but it had a small effect on elongation and modulus in both the machine and transverse directions. Tear strength decreased continuously, in both directions, upon increasing the LDPE-g-MAH content. The oxygen permeabilities of the three-layer films remained almost constant upon varying the amount of LDPE-g-MAH and all followed the series model. The water vapor permeabilities of the three-layer films, however, were affected by the degree of hydrogen bonding, which we analyzed by FTIR

spectroscopy, to result in a discrepancy between the experimental findings and the series model, especially when the EVOH content was increased.

An alternative process to fabricate laminar polymeric film is the blending process. In Chapter 5, we investigated the morphological, thermal, barrier, and mechanical properties of low-density polyethylene/ethylene–vinyl alcohol blend (LDPE/EVOH; 85/15 wt%) in highly and biaxially oriented blown films. We used linear low-density polyethylene-grafted maleic anhydride (LDPE-g-MAH) in various amounts as the compatibilizer for this immiscible system. Thermal analyses of the blend films indicated that their melting temperatures, crystallization temperatures, and heats of fusion remain almost constant upon varying the amount of compatibilizer. The addition of the compatibilizer did not adversely affect the inherent properties of the blends, especially their barrier properties, through constraint effects of the grafted EVOH (EVOH-g-LD). The heat of fusion of EVOH obtained during the first heating was much higher than that of the second as a result of the stress-induced crystallization that occurs during the blown-film process. Oxygen permeation measurements demonstated that the oxygen barrier properties of both highly and biaxially oriented blown films decrease upon increasing the amount of compatibilizer, although morphological analysis indicated that the blends exhibit better laminar dispersion of the EVOH phase in the LDPE. The increase in oxygen permeability results from the formation of microvoids at the interface between the two phases during the blown-film process. Mechanical measurements indicated that there exists an optimal amount of LDPE-g-MAH at which both the tensile and tear properties are maximized in both the machine and transverse directions.

Abstract (in Chinese)

　　多層化結構高分子薄膜是一種單一結構的薄膜產品,包含了兩種或兩種以上的高分子,彼此之間形成多層化且平行的結構。高分子薄膜通常用於包裝用途,例如食品包裝、藥品包裝及化妝品包裝,這些用途的包裝膜特性需求通常不只一種,而單一材料所製備的高分子薄膜又無法提供多樣化的性質。因此將兩種或兩種以上高分子結合成多層化結構的薄膜產品就應運而生了。多層化結構高分子薄膜的製備方式通常有兩種,一種為共擠押製備,另一種為混鍊製程,本研究將對這兩種製程所製備的薄膜特性做分析研究。

　　由共擠押製程所製備具有多重性質的多層化結構高分子薄膜,其整體性質的表現則是來自於各層性質的貢獻。本研究以 HDPE/tie/PA-6 為例,來驗證性質預估的方法,由各層的性質來預估任何不同厚度組成三層薄膜的拉伸性質及氣體穿透速率,若這預估的方法有效,對於在薄膜組成的設計與搭配上,將會是一個非常經濟及有效率的方法。用 series model 來預估氣體穿透率(包含氮氣、氧氣、二氧化碳及水蒸氣),與實驗值有非常好的吻合性。在拉伸性質方面,首先找到適當的構成方程式來描述薄膜的拉伸行為,而構成方程式中用來描述三層薄膜拉伸行為的各個參數,可經由各層參數及 additive rule 來進行預估,從實驗值與預估值的比較結果來看,在低速的拉伸測試時,有很好的吻性,但在高速拉伸時,由於黏滯熱(viscous dissipation)的產生,導致了實驗值與預估值之間的不一致。

　　在一般的共擠押製程中,由於黏著層的層數佔將近一半的層數,如五層薄膜 LDPE/tie/EVOH/tie/LDPE,而黏著層的主要功能為界面黏著,對整體的性質表現無實值的貢獻,因此在本研究中,將黏著層的

塑料混鍊至 LDPE 塑料中而當成混鍊層（blend layer），如此不僅可增加 LDPE 與 EVOH 的接著性，並藉此將原有的五層減少為三層薄膜，而形成 blend/EVOH/blend 的三層高分子薄膜，如此也可降低共擠押模具的設計成本，簡化製程上的操作。在固定混鍊層與 EVOH 的厚度比例下，界面黏著力，隨著黏著塑料在 LDPE 中含量的增加，黏著力愈強，由 FTIR 的分析圖來看，這是由於黏著劑的馬來酸酐與 EVOH 的氫氧基反應形成化學鍵-酯基（ester band）所造成的結果。而在拉伸強度的表現上，黏著塑料含量的改變並沒有造成明顯的變化，在撕裂強度，卻隨著黏著劑含量的增加，而明顯的下降。在氧氣穿透率方面，在固定黏著劑的含量下，改變混鍊層與 EVOH 的厚度比例，氧氣穿透率有很明顯的下降。而在水蒸氣穿透率方面，則是呈現持平，而並沒有如預期般的上升，這是由於在 EVOH 中氫鍵的產生，由 FTIR 中可知，隨著 EVOH 的增加，氫鍵的逐漸的增強，因此造成水分子不易穿透，因此呈現持平的結果。

另外在本研究中，欲利用另一種製程，製備具有多層化形態的高分子薄膜，使這單一薄膜同時具有各成份的特性，此種製程為混鍊製程。欲混鍊的材料為高阻氧性的材料-EVOH、高阻水氣材料-LDPE 以及相容劑-LDPE-g-MAH，經由單螺桿塑化後進入吹袋模具，而製備成薄膜。由 SEM 圖來看，隨著相容劑含量的增加，分散相 EVOH 的長度逐漸的變短，但層化的數目也愈多。另外由 OM 圖來看，分散相 EVOH 的形狀則是逐漸由類似長條纖維狀而變成小顆粒的圓球狀。由 DSC 的分析圖得知，在第一次升溫掃描時所求得的熔化熱比第二次高了許多，這是由於在製備薄膜的程中造成了順向結晶（stress-induced crystallization）所造成。在氧氣阻隔性方面並不如預期般的有明顯的下降，這是由於在製備薄膜的過程中，因為高度的雙延伸，造成

分散相與連續相之間產生微微孔洞（microvoid）所導致的結果。在拉伸性質方面，縱向（MD）的拉伸強度在相容劑為 1phr 時，有一極大值，這是由於此時較為剛性的 EVOH 的形狀呈現長條狀，因此具有纖維強化（fiber-reinforcement）的作用，隨著相容劑的增加，EVOH 的形狀呈現圓球會，此作用便消失，再加上兩相的界面產生了微孔洞，因此強度便下降。在 TD（縱向）的拉伸強度，應會隨著相容劑的增加而逐漸的增加，但是在高含量的時候，卻呈現持平的趨勢，這是由於微小孔洞將強度有所抵消所致。

Acknowledge

誌謝

漫長的求學生涯終於畫下句點了，回顧過去的求學時光，許許多多的回憶便湧上了心頭，其中的酸甜苦辣便成為此生中最寶貴的經驗。

首先感謝啟蒙恩師吳建興教授的引領，讓我進入了高分子加工這個實用性相當高的領域。再來感謝高雄應用科技大學黃俊欽研發長在實驗上的全力協助，讓學生能順利的完成研究內容，而黃研發長的專業知識及工作效率更是學生值得學習的典範。

感謝廖士興、陳成寶、戴郡良、錢峰明、陳志倫、李曄旭、朱明毅等諸位學長，讓我度過了剛進研究所生活的不適應期。再來感謝同學尤均文及歷屆學弟妹在研究上及生活上的幫忙，尤其是陳勇志學弟，是我在研究過程中的最佳幫手。

最後謹以此論文獻給我最親愛的家人，尤其是父母親無怨無悔的支持，才能讓我毫無後顧之憂下，順利的取得博士學位。

感謝一同走過這段歲月與支持我的所有朋友。

Contents

List of Tables

List of Figures

Chapter 1

Introduction

1.1 Laminar Polymeric Films

Polymeric films comprise one of the most important types of products created in the polymer industry. A large percentage of these films are used in the packaging industry. A very wide range of criteria must be applied when considering the type of film to be used for a particular purpose. In general, however, these criteria fall into three broad groups. The first group is basically concerned with the strength of the films, such as their tensile, impact, and tear strengths and their stiffnesses. The second group of properties may be classed broadly as the films' transmission properties, which include their permeabilities toward gases, vapors, and odors. Light transmission is also included here; it covers properties such as the "see-through" clarity and haze. For convenience, other optical properties, such as a film's gloss, also are dealt with in this section. These first two groups deal with those properties that are important to the final end-use performance. The third and final group includes the properties that are more concerned with the performance of the films during the converting and packaging processes; these properties include the film's coefficient of friction, blocking, heat sealability, and crease-of-flex resistance [1].

One of the most important requirements for the use of plastics as packaging films is their impermeability to gases and hydrocarbons. Their mechanical properties should also meet product specifications. In most cases, one polymeric material cannot offer

all of the properties required; therefore, a combination of polymers is employed to produce polymeric films that have laminar structures. Usually, the laminar polymeric film is prepared by either a coextrusion or blending process; the details of the two processes are described in the following sections.

To explain the versatility of laminar polymer films, it is convenient to provide an example here. Polyethylene is an excellent moisture barrier for packaging and its low cost, strength, and ease of processing make it suitable for many applications. Its inability, however, to act as a barrier for oxygen, aromatics, and oils limits its potential applications. On the other hand, ethylene–vinyl alcohol copolymer (EVOH) possesses excellent barrier properties toward oxygen, aromatics, and oils [2–5]. Unfortunately, EVOH is highly sensitive to moisture, which alters its ability to act as an oxygen barrier [6,7]. A laminar film processed from these two films through a coextrusion or blending process would possess a combination of the advantageous properties of each material. The word "laminar", which originates from studies of transport phenomena, describes a smooth, uniform, non-turbulent flow of a gas or liquid in two or more parallel layers, with little mixing between layers. For films possessing laminar structures, the term describes component polymers that are positioned in uniformly parallel arrangements with respect to one another without intermixing.

1.2 The Coextrusion Process

1.2.1 Introduction

Conventionally, polymeric films having laminar structures are fabricated by either a coextrusion or lamination process. The attractions of the coextrusion process lie on both economic and technical grounds. It is a single-step process that starts from two

or more polymers that are simultaneously extruded and shaped in a single die to form a laminar polymeric film or sheet. The laminar polymeric films produced by the coextrusion process may also be called multilayer films. Figure 1-1 displays a typical laminar polymeric film fabricated by a coextrusion process; it comprises a functional layer, a bonding (or tie) layer, and a support layer [8]. The functional layers, ethylene-vinyl alcohol copolymer (EVOH) and Poly(vinylidene chloride) (PVDC), provides excellent oxygen barrier properties; the bonding layer is a thermoplastic, extrudable polymer that adheres to the otherwise incompatible polymers; the tasks of support layers in the coextrusion process are to achieve good mechanical strength, weldability, moisture barrier, transparency or colorability, and printability properties in the final laminar film, as well as to improve the conversion behavior. Each layer contributes different properties that improve the overall performance of the film. Table 1-1 lists the material combinations and special properties of important of coextruded blown films.
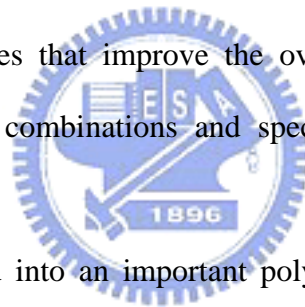
Coextrusion has developed into an important polymer fabrication process and it provides large growth opportunities for the polymer industry. The applications of coextruded multilayer polymers are challenging those of such traditional materials as metals, glasses, papers, and textiles. Coextrusion allows the ready manufacture of products having layers thinner than can be made and handled from their individual layers. Consequently only the necessary thickness of a high-performance polymer is required to meet the particular specifications of the product. Layers may be used, for example, to place colors, bury recyle, screen ultraviolet radiation, provide barrier properties, minimize die-face buildup, and to control the film's surface properties. Additives, such as antiblock, antislip, and antistatic agents, can be placed in specific layer positions. High-melt-strength layers can carry low-melt-strength materials during fabrication. The largest market for coextruded films and sheets is the

packaging industry; for example, two- or three-layer films are used as trash bags and five-to-nine-layer structures as flexible and semi-rigid packages. As many polymers as are necessary may be used to obtain the desired heat sealibility, barrier properties, chemical resistance, toughness, formability, and aesthetic appearance. Growing markets for applications of the coextrusion process are in the automotive, construction, appliance, and photoelectronics industries, and in food and medical packaging.

The choice of whether to use the blown or flat film process normally depends on the desired rate and final properties of the structure. Flat-film lines can typically run at a higher rate than can blown-film lines because the cooling efficiency of a chill roll is higher than that of the air used to cool the bubble. The flat film process, however, produces a product having uniaxial orientation, rather than the biaxial orientation produced by the blown film process. In many cases, the biaxial orientation is preferred because it produces a film that has more-balanced physical properties. The biaxial orientation can be also achieved by using a tentering process, but it comes with a higher cost and requires complicated steps. In our studies, we prepared laminar polymeric films by coextrusion blown-film processes.

1.2.2 Methods of Coextruding Films

There are two fundamentally different methods for coextruding films, namely, the coextrusion blown-film and coextrusion flat-film processes. The capital and operating costs for a coextrusion blown film process and a flat-die, chill-roll casting process depend on the product mix and utilization. Equipment suppliers provide comparative economic evaluations for specific products. The extruder used before the die and the take-off equipment used afterwards are standard equipment applied to the single-layer film manufacture of both blown and flat films.

The coextrusion blown-film process is based on the principle of two or more

polymers that have been plasticized and homogenized in separated extruders, fed into a coextrusion blown-film die to form a tubular structure, blown into a bubble, cooled and passed through the collapse frame, and collected by a winder. Figure 1-2 depicts the setup of a coextrusion blown-film process. The design of coextrusion blown-film die used most commonly today is that of a multimanifold spiral mandrel (Figure 1-3). This die consists of several concentric manifolds, one located within another. The manifolds are supported and secured through the base of the die. Each manifold consists of a flow channel that spirals around the mandrel, which allows the melt polymer to flow down the channel or leak across a land area to the next channel. This flow pattern smoothes out the flow of the polymer and minimizes any weld lines in the final film. Another type of coextrusion blown film die is the stackable plate die (Figure 1-4). In this type of die, each layer is spread uniformly and formed into a tube in a single plate. The plates are then stacked on top of one another and the layers are added sequentially. This type of die is becoming popular for specific applications because the number of layers can be adjusted by simply changing the number of plates in the die. The major disadvantage for this type of die is that a large separating force exists between the plates and, thus, many die bolts are required to hold the plates together. This situation means that the plates must have rather large diameters to maintain structural integrity and this requirement can produce longer flow paths and temperature differentials that can be detrimental to thermally sensitive polymers.

The coextrusion flat-film process is based on the principle of shaping two or more polymers, which have been plasticized and homogenized in separated extruders, into a planar structure in a coextrusion flat die, cooling and stabilizing this structure by means of roll contact, and then winding it up to a trimmed working width. Figure 1-5 displays the setup of a coextrusion flat-film process. Two basic types of die used in flat-die coextrusion system are the multimanifold and feedblock/single-manifold dies.

A hybrid-type die combines feedblocks with a multimanifold die.

In a multimanifold die (Figure 1-6), each layer incorporates individual manifolds that extend to the full width of the die. Each manifold is designed to distribute its polymer layer uniformly before combining it with the other layers. The major advantage of a multimanifold die is the ability to coextrude polymers that have very different viscosities because each layer is spread independently prior to being combined. A significant disadvantage of wide multimanifold dies is the difficulty in coextruding very thin layers, such as thin cap or thin tie layers. When using a wide die, it is difficult to obtain uniformity when the extrusion rate per width is very low; additionally, it is expensive and requires the attention of skilled operators. The feedblock/single-manifold dies of a flat-die coextrusion system use a feedblock before a conventional single manifold (Figure 1-7). A layered melt stream, which is prearranged ahead of the die inlet by the feedblock, is extended to the width of the die as it is reduced in thickness (Figure 1-8). Polymer melts from each extruder can be subdivided into as many layers as desired in the final product. One limitation of the use of feedblocks is that polymer viscosities must be matched fairly closely because the combined melt stream must spread uniformly within the die. A severe viscosity mismatch results in lay nonuniformity; the lower viscosity material tends to flow to the die edges. A crude rule of thumb is that polymer viscosities must be matched to within a factor of three or four, which is a reasonably broad range for many commercially important coextrusion processes. Often, to avoid flow instabilities, polymers are intentionally selected that have mismatched viscosities. The layer nonuniformity expected to arise from the mismatch is compensated by varying the melt temperature, to eliminate the viscosity mismatch, or by using a feedport that has a shaped geometry. Combinations of feedblocks and a multimanifold die are also used commercially. The multimanifold die can incorporate the same design principles as

the feedblock: i.e., vanes separating individual manifolds within the die. In a sense, the multimanifold die is a wide feedblock. A feedblock may be attached to one or more manifold inlets, as indicated in Figure 1-9. With this system, it is possible to coextrude polymers that have widely different viscosities and processing temperatures.

1.2.3 Layer Nonuniformity in Coextrusion Processes

Polymer rheology information is critical for designing coextrusion dies and feedblocks. The flow characteristics of the polymer must be considered when selecting materials for coextruded products. The viscosities of non-Newtonian polymers depend on the extrusion temperature and shear rate, both of which are factors that may vary within the coextrusion die. The shear rate dependence is further complicated because it is determined by the position and thickness of a polymer layer in the melt stream. The die or feedblock that has the best design does not necessarily ensure a commercially acceptable product. Layered melt streams flowing through a coextrusion die can spread nonuniformly or can become unstable, which can lead to layer nonuniformities — and even intermixing of layers — under certain conditions. The causes of layer deformation are related to non-Newtonian flow properties of polymers and viscoelastic interactions. Previous studies have shown that variations in layer thicknesses during coextrusion processes can arise from many causes, with several of the primary ones being interlayer instability, viscous encapsulation, and elastic layer rearrangement.

1.2.3.1 Interlayer Instability

Interfacial instability is an unsteady-state process in which the interface location between layers varies locally in a transient manner. Interface distortion due to flow

instability can cause thickness nonuniformities in the individual layers while still maintaining a product that has constant thickness. These instabilities result in irregular interfaces — and even layer intermixing in severe cases. At very low flow rates, the interface is smooth, as indicated in Figure 1-10(a). At moderate output rates, low-amplitude waviness of the interface is observed [see Figure 1-10(b)]; this waviness is barely noticeable to the eye and may not interfere with the function of the multilayer film. At higher output rates, layer distortion becomes more severe [Figure 1-10(c)]. If a large-amplitude waveform develops in the flowing multilayer stream within the die, the velocity gradient can carry the crest forward and convert it into a fold. Multiple folding results in an extremely jumbled, intermixed interface. This type of instability, which commonly is called "zigzag instability", has been observed in tubular blown-film, multimanifold, and feedblock/single manifold dies. This instability develops in the die land; its onset can be correlated with a critical interfacial shear stress for a particular polymer system [9]. The most important variables that influence this instability are the skin-layer viscosity, skin-to-core thickness ratio, total extrusion rate, and die gap. Although the interfacial shear stress does not cause instability, elasticity is related to shear stress; the interfacial stress is used to correlate variables for a particular system. Interfacial instability in a number of coextruded polymer systems has been correlated experimentally with their viscosity ratios and elasticity ratios [10], and a simplified rheology review is available [11]. Other studies have focused on viscosity differences [12–14], surface tension [15], critical stress levels [9,16,17], viscosity model parameters [18–20], and elasticity [21–29]. Other types of instabilities may exist: for example, a problem has been observed in the feedblock coextrusion of axisymmetric sheets [30]. A wavy interface is also characteristic of this instability, but the wave pattern is more regular when viewed from the surface. The instability, which commonly is called "wave instability",

originates in the die, well ahead of the die land; the internal die geometry influences both the severity and the pattern. For a given die geometry, the severity of instability increases with structure asymmetry; some polymers are more susceptible to unstable flow than are others. It has been suggested that this type of instability may be related to the extensional rheological properties of the polymers used in the coextruded structure [31]. Figure 1-11 provides examples of both zigzag and wave instabilities. No complete predictive theory exists that explains these complicated rheological interactions, but the accumulated experience of polymer producers, equipment suppliers, and experienced fabricators provides guidance in polymer selection.

1.2.3.2 Viscous Encapsulation

The importance of viscosity matching for layer uniformity was first studied in the capillary flow of two polymers for bicomponent fibril production [32–35]. Two polymers, which are introduced side by side into a round tube, experience interfacial distortion during flow if the viscosities are mismatched. The lower-viscosity polymer migrates to regions of highest shear (at the wall) and tends to encapsulate the higher-viscosity polymer (Figure 1-12); it is possible for the lower-viscosity polymer to totally encapsulate the higher-viscosity polymer. Nature seeks the path of least resistance. The degree of interfacial distortion that is due to the viscosity mismatch depends on the extent of the difference in viscosity, the shear rate, and the residence time. Tubular blown-film dies are more tolerant of viscosity mismatch because the layers are arranged concentrically, i.e., there are no ends. Since streamlines cannot cross each other, further migration cannot occur, but good die design is required to obtain concentric layers.

1.2.3.3 Elastic Layer Rearrangement

While matching the viscosities of adjacent layers has proven to be a very important requirement, the effect of polymer viscoelasticity on layer thickness uniformity is also an important consideration in the coextrusion process [36–40]. It has been shown that, in a die that can distort the interface between layers, polymers that are comparatively high in elasticity produce secondary flows normal to the primary flow direction (Figure 1-13). This effect becomes more pronounced as the width of a flat die increases. Appropriate shaping of the die channels can minimize the effect of layer interface distortion that is due to elastic effects. Coextruding a structure that contains layers of polymers with alternating low and high levels of elasticity can cause interface distortion that is due to the differences in elasticity between the layers in the flat dies. Typically, this effect is not observed in tubular dies.

1.2.3.4 Solution Method for Layer Deformation Problem

Zigzag-type interfacial instability can be reduced or eliminated by increasing the skin-layer thickness, increasing the die gap, reducing the total rate, or decreasing the skin polymer viscosity; these methods may be used singly or in combination. These remedies reduce interfacial shear stress, and stable flow results when it is below the critical stress for the polymer system being coextruded. Most often, it is the skin layer polymer viscosity that is decreased. In feedblock coextrusion, the resultant viscosity mismatch imposed by this remedy can cause variations in layer thickness. Shaped skin layer feedslots are then typically used to compensate and produce a uniform product. A review of techniques used to minimize this type of layer deformation has been published [41]. Care should also be taken when designing the joining geometry in a feedblock or die. To minimize instabilities, the layers should have similar velocities at the merging point. The joining of the layers should occur in a geometry that is as parallel as is realistically possible, rather than joining them in a

perpendicular manner. The layers should also merge into a channel that is of an appropriate height so that it does not force one layer to flow into the other. Wave instability is related to the extensional viscosities of the individual layers. This finding implies that all of the design criteria mentioned previously for layer joining are also important for this type of instability, as is the spreading of the layers in a film or sheet die. Since this type of instability is related to extensional viscosity, the rate at which the layers are stretched in the die will affect the forces in each layer. In structures containing materials that have high extensional viscosities, the die should be designed to spread the layers slowly and at a uniform rate; this process will help minimize wave pattern instabilities.

1.3 Blending Process

1.3.1 Introduction

The coextrusion process does have some disadvantages, such as the high cost of investing in equipment and the difficulty in process control resulting from requirements for multiple extruder and dies, adhesives between layers, and multi-step operations. In addition, multilayer composite films have limitations in their recyclability because the resins, which have different characteristics, adhere together. Recently, diverse techniques have been proposed to produce laminar structures for preparing food packaging films, such as sol-gel silica coating [42,43], plasma coating [44], and blending [45,46]. Among these techniques, the blending approach for improving barrier properties has been recognized as an attractive methodology because existing extrusion processing systems can be used without further investment of equipment. Blending is a process that combines two or more polymers into a polymer blend through mixing. Such a blend is sometimes called an "in situ"

composite because of the shaping that occurs in situ during processing. This blend system acts as a dispersion of one polymer within the other, with chemical linking occurring between dissimilar chains across the interface. In packaging applications, a combination of a barrier material (EVOH) and a lower-cost matrix material (PE or PP) is fabricated into the polymeric film. Figure 1-14 displays the laminar structure of a blend film comprising LDPE as the matrix and EVOH as the dispersed phase.

1.3.2 Factors that Affect Laminar Morphology

Many properties, such as permeability and mechanical properties, are determined by the morphology of the blend film. Generally, the morphology is determined by many factors, such as the rheological properties of the component polymers, the interfacial tension, the blend composition, and the processing type and its parameters. Significant melt-processing parameters include the flow patterns, the shear stresses, the mixing history, and the processing temperatures. It has been established that a high shear rate, a viscosity ratio (viscosity of dispersed phase/viscosity of matrix) smaller than, or close to, unity [45,47,48], and a low interfacial tension are all favorable for increasing the level of deformation and breakup of the dispersed-phase droplets [49–51]. It is well established that extensional flow is more efficient than shear flow in the deformation of the dispersed phase [52–55]. One of the most important factors for controlling the blend morphology is modifying the interface between the phases by adding a compatibilizer to obtain greater compatibility. Improved compatibility ensures an efficient stress transfer from the continuous phase to the dispersed phase during the extrusion and stretching process and, consequently, it results in greater deformation of the dispersed phase [56]. Thus, the addition of a compatibilizer improves the dispersion and, in some cases, enhances the ultimate mechanical properties of the blends [57–61]. Usually, there is an optimum content of

compatibilizer required to improve the properties [62–64].

1.3.3 Relation of Laminar Morphology and Properties

In polymer blend system, improving the barrier properties is achieved through the formation of a laminar morphology of the dispersed-phase, barrier material having a moderate aspect ratio. This situation arises because of the orientation effect, which occurs during the extrusion process, that results in an increase of tortuous paths [45,47,62,65–67]. Alternatively, the improvement in mechanical properties is achieved through the formation of a laminar morphology of the dispersed-phase, reinforced material having a high aspect ratio, such as a fibril-reinforced polymer blend [68–70]. The orientation of the dispersed phase in the form of fibrils, which is directly related to the stiffness of the phase, has been identified as the key parameter for determining the mechanical performance of the entire in situ composite [71].

The first successful attempt to produce a blow-molded high-barrier container with developed laminar morphology was reported by Subramanian [72]. The results showed that PA-6, the barrier resin, could be distributed in the form of large, thin sheets, which have laminar structure, in the HDPE matrix by extruding the blends under special extrusion conditions. In addition, a PP/EVOH blend film that has higher barrier properties was obtained by generating a laminar structure having a larger area by using a biaxial orientation film process [62]. Although EVOH exhibits excellent gas barrier properties and transparency, it has some drawbacks, such as its high cost, low toughness, and difficulty to process [73]. On the other hand, PA is inexpensive relative to EVOH and exhibits both high resistance to the permeation of hydrocarbons and good toughness. [74]. Thus, polypropylene and polyamide can be blended to improve the thermal and mechanical properties of polypropylenes. Furthermore, the addition of polyamide to polypropylene results in an improvement in the barrier

properties. Polypropylene exhibits excellent barrier properties to moisture, but it is a poor barrier toward O_2, CO_2, and N_2. In contrast, polyamide possesses high barrier properties toward these gasses and a high resistance toward hydrocarbons [75]. A compatibilizer must be used, however, to enhance the interphase adhesion and phase stability in immiscible blends of PP and PA [76]. The ultimate barrier property of the polymer blend depends on the morphological structure of the dispersed phase, the intrinsic barrier property of each component, and the nature of the interface between the two phases [66,77,78]. Recently, it was reported that injection-molded PP/PA blends having improved barrier properties can be produced by generating a laminar morphology of a polyamide-dispersed phase that was induced by shear and elongational flows [79]. Following the principles mentioned above, Kamal and co-workers [80,81] prepared PP/EVOH blends, which have laminar morphology, under controlled processing conditions using a special die designed to incorporate converging and diverging sections. In the process of producing this film, however, the authors did not obtain a blend film with highly improved barrier properties because drawing occurred only in the machine direction during the take-off stage from the die to the chilled roll, and it resulted in a laminar film of the dispersed phase having a small area. Faisant et al. have also reported that the oxygen permeability of PP/EVOH blends can be decreased significantly by inducing fibrillar and laminar morphologies of the EVOH phase by operating only under uniaxial drawing between the two roll mills. In the processing aspect, the final blend morphology is also determined by an orientation operation [46]. Yeo et al. has reported that an improved barrier property can be obtained by generating a laminar structure of the dispersed phase in the matrix phase of a PP/EVOH blend by applying a biaxially oriented film process [62]. This laminar morphology, which is induced by biaxial orientation, results in a significant increase in the oxygen barrier properties of PP/EVOH (85/15) blends: by ca. 10 times

relative to that of pure PP.   Lee and Kim proposed a indicator, $(L \times R) \times N$, of the oxygen barrier properties, where $L \times R$ is the average dimension of the dispersed phase and N is the average number of dispersed phase layers per µm. An optimum value of this indicator, which improves the barrier properties, was obtained upon adding the compatibilizer [45]. These authors also showed that large predeformed domains in the extruder outlet, which have short residence time under high screw rpm in the die, favored the formation of well-developed laminar structures that possess low oxygen permeabilities. Two different thermotropic liquid crystalline polymers (TCLPs), copolyesters, in propylene (PP) were analyzed with particular attention to the gas transport and mechanical properties of the extruded blend films [71]. Slight improvements of barrier permeability and toughness, with respect to PP, were obtained because the TCLPs were formed into the fine dispersions of fibril and laminar structures. A ternary blend, including a polyamide (Nylon 46), a thermotropic liquid crystalline polymer [TCLP, Poly(ester amide)], and a thermoplastic elastomer (EPDM), that has improved tensile properties was prepared by developing a fine dispersion of fibril, having a high aspect ratio, and laminar structures of TCLP in a shear flow field [82]. Both the tensile strength and modulus of the ternary blend increased upon increasing the draw ratio in the flow direction.

As we mentioned above, the development of the morphology of the blend is the key point that determines the properties of the blend films.

1.4 Objectives

Polymeric films are used widely in the flexible packaging market because of their clarity, toughness, light weight, flexibility, low cost, and recyclability [83]. To provide adequate shelf life, however, many packaging applications require films that have

even higher levels of oxygen and moisture impermeability. Polymeric films that have laminar structures, prepared from more than two resins, have both of these barrier properties and offer a choice, in addition to metals and glasses, for use in packaging applications. Sometimes, the requirements of certain mechanical properties are also considered for these applications. Thus, the question of how to achieve such requirements in a laminar polymeric film, with respect to the choice of materials and the processing methods used, becomes increasingly important.

We had several objectives at the onset of this research:

1. To study laminar polymeric films fabricated by different processing methods, including coextrusion and blending processes.

2. To study and predict the permeability and tensile behavior of laminar polymeric film fabricated by a coextrusion process. The polymeric film has an A/B/C structure, where that A and C represent support and functional layers, respectively, and B is the bonding layer.

3. To reduce the number of layers in a multilayer film fabricated by the coextrusion process, we chose to use a blend of support material and bonding material as the outer layer to promote the adhesion to the functional layer. The structure of the polymeric film is A/B/A, where A represents the blend layer and B the functional layer. The processibility and some properties of the film having the A/B/A structure were to be investigated.

4. To study the thermal, barrier, and mechanical properties related to the laminar morphology in polymeric films fabricated by the blend process and a subsequent blown-film process.

1.5 References

1. J. H. Briston and L. L. Katan, "Plastics Films", John Wiley and Sons, New York, 1989.

2. R. H. Foster, *Packaging*, **32**, 70 (1987).

3. T. Iwanami, Y. Hirai, *Tappi J.*, **66**, 1404 (1983).

4. J. M. Lagaron, A. K. Powell, and G. Bonner, *Polym. Test.*, **20**, 569 (2001).

5. H. U. Beckmann, and Ch. Herschbach, *Kunst. Plast. Euro.*, **86**, 5 (1996).

6. Z. Zhang, I. J Britt and M. A. Tung, *J. Appl. Polym. Sci.*, **82**, 1866 (2001).

7. R. Gopalakrishnan, J. M. Schultz and R. Gohil, *J. Appl. Polym. Sci.*, **56**, 1749 (1995).

8. H. Tamber and M. Planeta, U. S. Patent 6218024, 2001.

9. W. J. Schrenk and T. Alfrey, Coextruded Multilayer Polymer Films and Sheets, *Polymer Blends,* Academic Press, New York, 1978, Chapter 15.

10. C. D. Han, Y. J. Kim, and H. B. Chin, *Polym. Eng. Rev.*, **4**, 177 (1984).

11. M. A. Arvedson, Rheological Considerations in Coextrusion, *TAPPI/PLC Conference Proceedings,* 513, 1984.

12. C. E. Hickox, *Phys. Fluids*, **14**, 251 (1971).

13. C. S. Yih, *J. Fluid Mech.,* **27**, 337 (1967).

14. A. A. Khan and C. D. Han, *Trans. Soc. Rheol.*, **21**, 101 (1977).

15. A. P. Hooper and W. G. Boyd, *J. Fluid Mech.*, **128**, 507 (1983).

16. C. D. Han and D. A. Rao, *Polym. Eng. Sci.*, **20**, 128 (1980).

17. W. J. Schrenk, *Polym. Eng. Sci.*, **18**, 620 (1978).

18. B. Khomami, *J. Non-Newt. Fluid Mech.*, **36**, 289 (1990).

19. B. Khomami, *J. Non-Newt. Fluid Mech.*, **37**, 19 (1990).

20. N. D. Waters, *J. Non-Newt. Fluid Mech.*, **12**, 85 (1983).

21. G. M. Wilson and B. Khomami, *J. Non-Newt. Fluid Mech.*, **45**, 355 (1992).

22. G. M. Wilson, and B. Khomami, *J. Rheol.*, **37**, 315 (1993).

23. G. M. Wilson and B. Khomami, *J. Rheol.*, **37**, 341 (1993).

24. Y. Y. Su and B. Khomami, *J. Rheol.*, **36**, 357 (1992).

25. Y. Y. Su and B. Khomami, *Rheol. Acta*, **31**, 413 (1992).

26. B. Khomami and M. M. Ranjbaran, *Rheol. Acta*, **36**, 345 (1997).

27. H. K. Ganpule and B. Khomami, *J. Non-Newt. Fl. Mech.,* **81**, 27 (1999).

28. B. Khomami and K. C. Su, *J. Non-Newt. Fl. Mech.,* **91**, 59 (2000).

29. B. Khomami, Y. Renardy, K. C. Su, and M. A. Clarke, *J. Non-Newt. Fl. Mech.,* **91**, 85 (2000).

30. W. J. Schrenk and S. A. Marcus, *TAPPI/PLC Conference Proceedings,* 627, 1984.

31. R. Ramanathan, R. Shanker, T. Rehg, S. Jons, D.L. Headley, and W.J. Schrenk, *SPE-ANTEC Technical Papers*, **42**, 224 (1996).

32. J. H. Southern and R. L. Ballman, *Appl. Polym. Sci.,* **20**, 175 (1973).

33. J. L. White, R. C. Ufford, K. R. Dharod, and R. L. Price, *J. Appl. Polym. Sci.* **16**, 1313 (1972).

34. C. D. Han, *J. Appl. Polym. Sci.,* **17**, 1289 (1973).

35. A. E. Jr. Everage, *Trans. Soc. Rheol.* **17**, 629 (1973).

36. J. Dooley, K. S. Hyun, and K.R. Hughes, *Polym. Eng. and Sci.,* **38**, 1060 (1998).

37. J. Dooley and B.T. Hilton, *Plast. Eng.*, **50**, 25, (1994).

38. J. Dooley, and L. Dietsche, *Plast. Eng.*, **52**, 37 (1996).

39. B. Debbaut, , T. Avalosse, J. Dooley, and K. Hughes, *J. of Non-Newt. Fl. Mech.*, **69**, 255 (1997).

40. B. Debbaut and J. Dooley, *J. of Rheol.,* **43**, 1525 (1999).

41. T. I. Butler, *TAPPI J.,* 205 (1992).

42. K. Azuta, K. Tadanaga, and T. Minami, *J. Ceram. Soci. Japan*, **107**, 293 (1999).

43. S. Y. Lee, J. D. Lee, and S. M. Yang, *J. Mater. Sci.*, **34**, 1233 (1999).

44. L. Agres, Y. Segui, R. Delsol, and P. Raynaud, *J. Appl. Polym. Sci.*, **61**, 2015 (1996).

45. S. Y. Lee and S. C. Kim, Polym. Eng. Sci., 37, 463 (1997).

46. J. B. Faisant, A. A. Kadi, M. Bousmina, and L. Deschenes, *Polymer*, **39**, 533 (1998).

47. M. R. Kamal, H. Garmabi, and L. Arghyris, *Polym. Eng. Sci.*, **35**, 41 (1995).

48. R. M. Gohil, *J. Appl. Polym. Sci.*, **52**, 925 (1994).

49. K. Min, J. L. White, and J. F. Fellers, *Polym. Eng. Sci.*, **24**, 1327 (1994).

50. S. Wu, *Polym. Eng. Sci.*, **27**, 335 (1984).

51. R. Gonzalez-Nunez, B. D. Favis, P. J. Carreau, and C. Lavallee, *Polym. Eng. Sci.*, **33**, 851 (1993).

52. H. B. Chin and C. D. Han, *J. Rheol.*, **23**,557 (1979).

53. C. D. Han and K. Funatsu, *J. Rheol.*, **22**, 113 (1978).

54. H. B. Chin and C. D. Han, *J. Rheol.*, **24**, 1 (1980).

55. D. C. Huang and R. N. Shroff, *J. Rheol.*, **25**, 605 (1981).

56. R. Gopalakrishnan, J. M. Schultz, and R. M. Gohil, *J. Appl. Polym. Sci.*, 56, 1749 (1995).

57. A. Datta and D. G. Baird, *Polymer*, **36**, 505 (1995).

58. H. J. O'Donnell and D. G. Baird, *Polymer*, **36**, 3113 (1995).

59. Y. Seo, S. M. Hong, and K. U. Kim, *Macromolecules*, **30**, 2978 (1997).

60. Y. J. S, *J. Appl. Polym. Sci.*, **64**, 359 (1997).

61. S. Bualek-Limcharoen, J. Samran, T. Amornsakchai, and W. Meesiri, *Polym. Eng. Sci.*, **39**, 312 (1999).

62. J. H. Yeo, C. H. Lee, C. S. Park, K. J. Lee, J. D. Nam, and S. W. Kim, *Adv. Polym. Tec.*. **20**, 191 (2001).

63. O. Motta, L. Di Maio, L. Incarnato, and D. Acierno, *Polymer*, **37**, 2373 (1996).

64. S. B. Limcharoen, S. Saengsuwan, T. Amornsakchai, and B. Wanno, *Macromol. Symp.*, **170**, 189 (2001).

65. S. W. Kim and Y. H. Chun, *Korean J. Chem. Eng.*, **16**, 511 (1999).

66. P. M. Subramanian and V. Mehra, *Polym. Eng. Sci.*, **27**, 663 (1987).

67. R. Holsti-Meittinen, K. P. Perttila, J. V. Seppala, and M. T. Heino, *J. Appl. Polym. Sci.*, **58**, 1551 (1995).

68. L. E. Nielsen and R. F. Landel, "Mechanical Properties of Polymers and Composites", Marcel Dekker, New York, 1994.

69. F. Avalos, M. Arroyo, and J. P. Vigo, *J. Polym. Eng.*, **9**, 158 (1990).

70. M. Joshi, S. N. Maiti, and A. Misra, *Polym. Compos.*, **15**, 349 (1994).

71. L. Incarnato, P. Scarfato, O. Motta, and D. Acierno, *Polym. Eng. Sci.*, **21**, 354 (2000).

72. P. M. Subrmanian, *Polym. Eng. Sci.*, **25**, 483 (1985).

73. C. A. Finch, "Polyvinyl Alcohol", John Wiley and Sons, New York, 1993.

74. S. Y. Lee and S. C. Kim, *J. Appl. Polym. Sci.*, **67**, 2001 (1998).

75. R. Holsti-Meittinen, K. P. Perttila, J. V. Seppala, and M. T. Heino, *J. Appl. Polym. Sci.*, **58**, 1551 (1995).

76. R. Holsti-Meittinen, J. Seppala, and O. T. Ikkala, *Polym. Eng. Sci.*, **32**, 868 (1992).

77. G. W. Lohfink and M. R. Kamal, *Polym. Eng. Sci.*, **33**, 1404 (1993).

78. K. M. Kit, J. M. Schultz, and R. M. Gohil, *Polym. Eng. Sci.*, **35**, 680 (1995).

79. D. Jarus, A. Hiltner, and E. Baer, *Polymer*, **43**, 2401 (2002).

80. M. R. Kamal, G. Lohfink, L. Arghyris, and S. Hozhabr-Ghelichi, U. S. Patent No. 5,188,784 (1993).

81. M. R. Kamal, Hozhabr-Ghelichi, L. Arghyris, and M. Lambla, SPE ANTEC Tech.

Papers **38**, 2677 (1992).

82. Y. Seo, S. M. Hong, and K. U. Kim, *Macromolecules*, **30**, 2978 (1997).

L. B. Ryder, *Plast. Eng.*, **40**, 41 (1984).

Table 1-1 Materials combinations, special properties and important applications of coextruded blown films.

Material combinations	Special properties	Most important fields of application
Double-layer film		
1. LDPE/LDPE	pinhole-free (multicolored)	milk film, carrier bags, general packaging
2. LDPE/EVA	good weldability, sterilizable	heavy-duty bags, stretch packaging, medical articles
3. HDPE/EVA	sterilizable	blood plasma, bakery goods, food-stuffs
4. HDPE/LDPE	good strength	bakery goods, foodstuffs, tomato concentrate
5. LDPE/ionomer	good weldability, puncture-resistant	dairy products, foodstuffs, medical instruments. general packaging
6. LLDPE/LDPE LLDPE/EVA	high elasticity good surface adhesion	stretch film
7. Ionomers/EVA	grease-proof	coconut, biscuits
8. Ionomers/PA	gas- and aroma-tight	meat, sausage, ham. fish, foodstuffs, cheese
Three-layer film, symmetrical		
9. LDPE/HDPE/LDPE	weldable on both sides, reduced curling tendency	like 4, pet food, cornflakes
10. EVA/PP/EVA	like 9	like 9
11. EVA/HDPE/EVA	like 3	like 9, cornflakes
Two-layer film with tie-layer (TL)		
12. LDPE/TL/PA	gas, water- and aroma-tight	foamed PS granulate, meat, sausage, cheese, ham, fish, ready-made meals, hops
13. EVA/TL/PA	like 12 in hot-air channel good hot tack properties	like 12
14. Mod. EVA/TL/PA		like 12, vacuum packing for ham (shrinkable)
Three-layer film		
15. LDPE/HDPE/EVA	good weldability, good rigidity	bakery goods, foodstuffs
16. LDPE/EVA/PP	like 15	like 15
Fivelayer film		
17. LDPE/TL/PA/TL/ LDPE or LLDPE/TL/ PA/TL/LLDPE	no curling tendency, improved barrier properties, as PA projected against moisture absorption, improved layer adhesion, weldable on both sides	like 12
18. EVA/TL/PA/TL/EVA	like 17	like 17
19. LDPE/TL/EVAL/TL/LDPE	like 17	like 17, all sensitive food, requiring low gas permeability
20. LDPE/TL/EVAL/TL/LDPE	like 19	like 19, fish meal, wine packaging, milk powder (casein)
21. EVA/TI/EVAL/TL/EVA	like 19	like 19
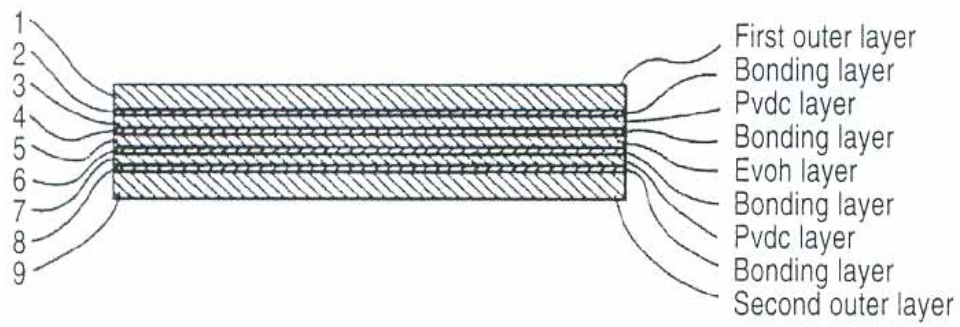
Figure 1-1 Multilayer laminar structure by coextrusion process
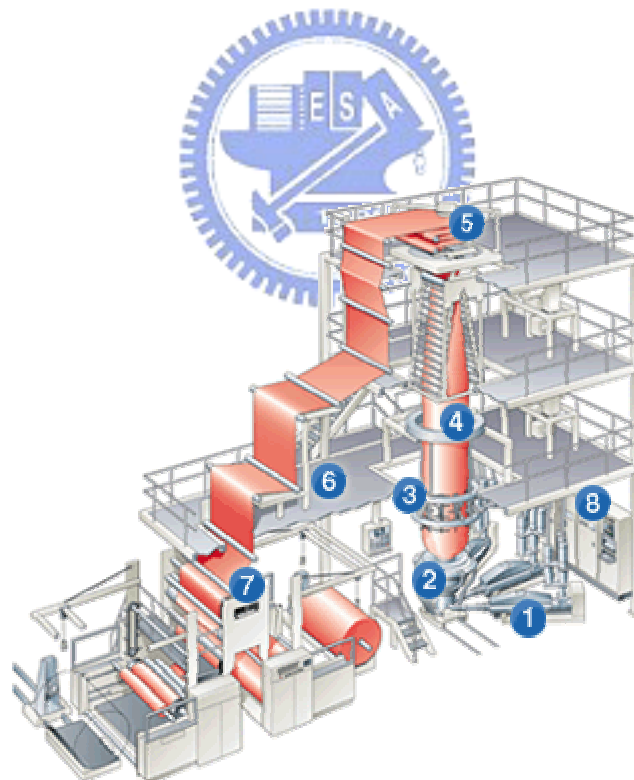
Figure 1-2 Coextrusion blown film line. (1) Extruders; (2) die and cooling equipment;

(3) sizing unit; (4) thickness gauge; (5) take-off unit; (6) film edge control; (7) winder.
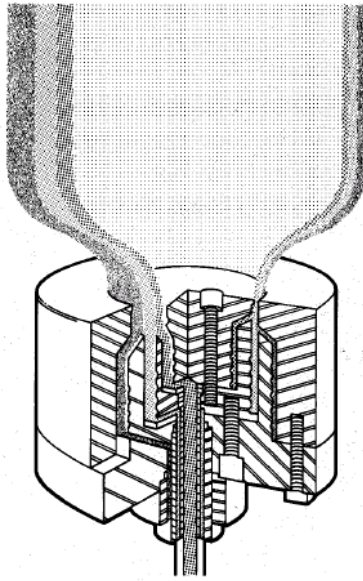
Figure 1-3 A three-layer multimanifold spiral mandrel blown film die.
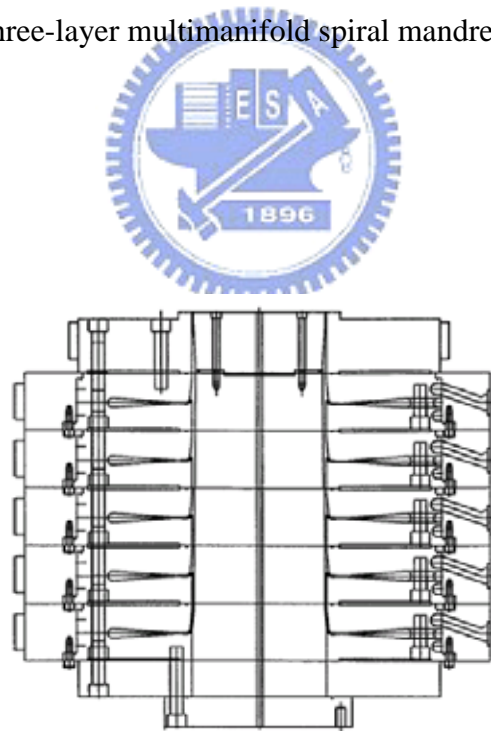
Figure 1-4 A Stackable blown film die.
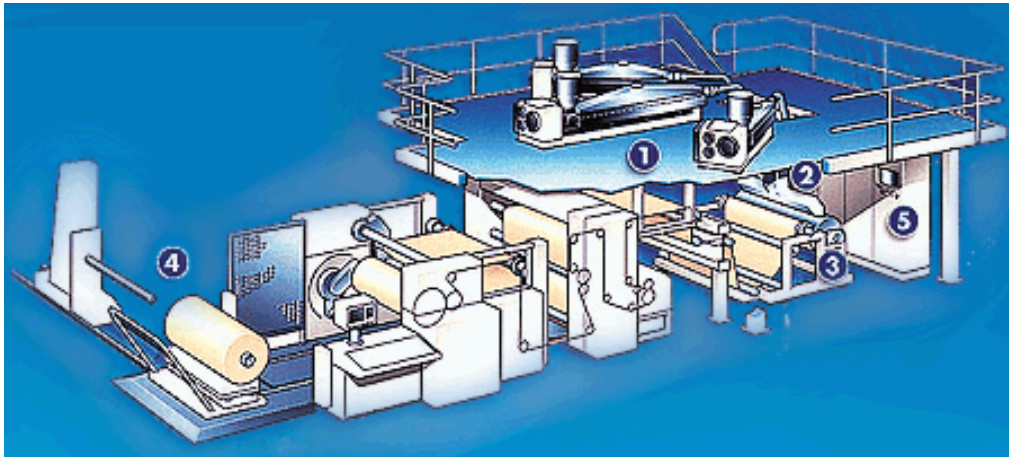
Figure 1-5 Coextrusion flat film line. (1) Extruders; (2) die; (3) casting section; (4) winder.
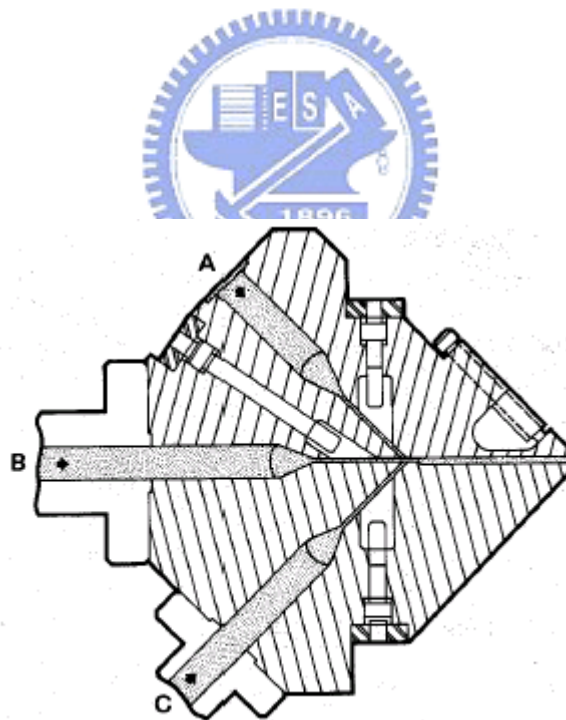
Figure 1-6 Cross-sectional view of three-layer multimanifold flat film die.
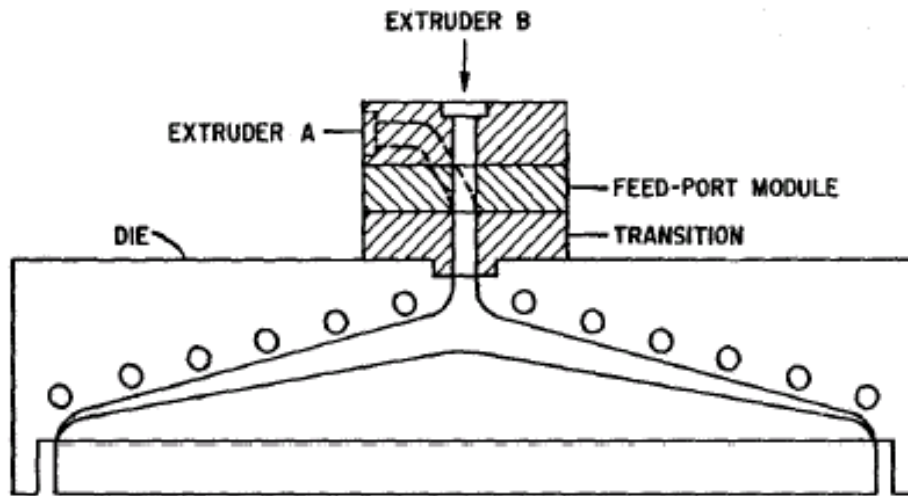
Figure 1-7 A feedblock/single manifold die
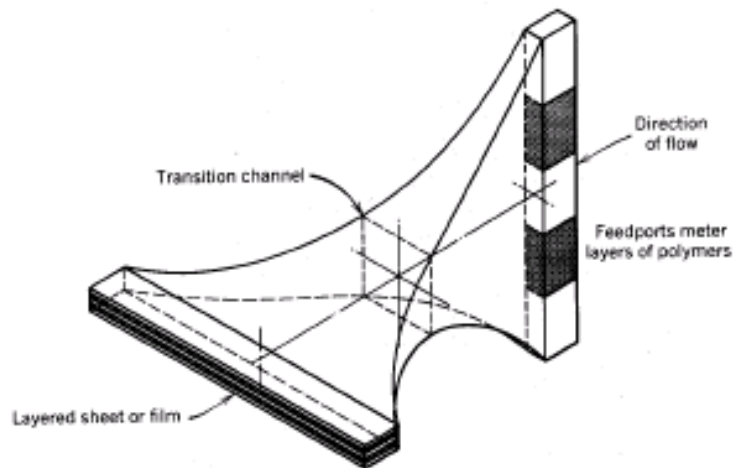
Figure 1-8 The principle of the feedblock for coextruding multilayer film. Numbaer of layers is equal to number of feedports.
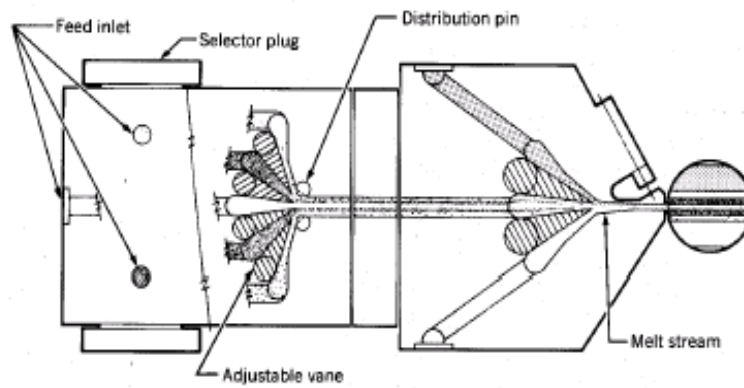
Figure 1-9 Combination feedblock and multimanifold die system. Feedblock feeds center-die manifold.
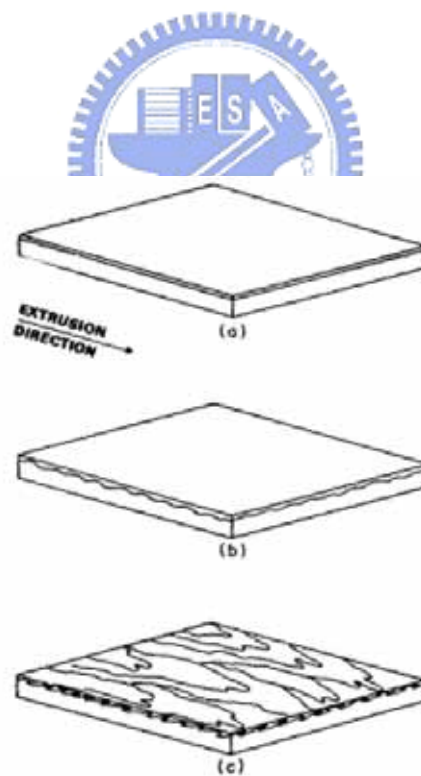
Figure 1-10 Interlayer instability
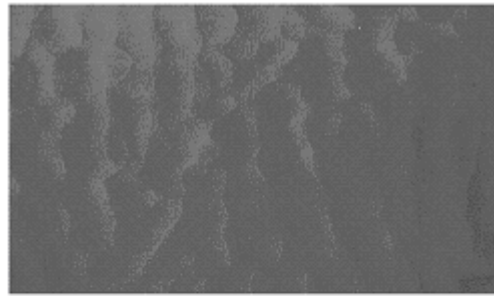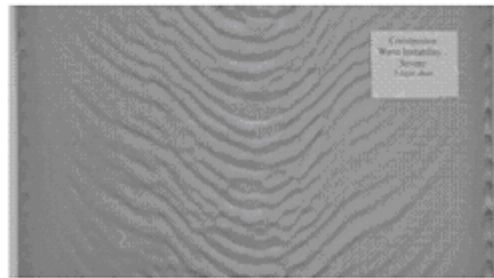
Figure 1-11 Interlayer instability pattern. (a) zig-zag; (b) wave.
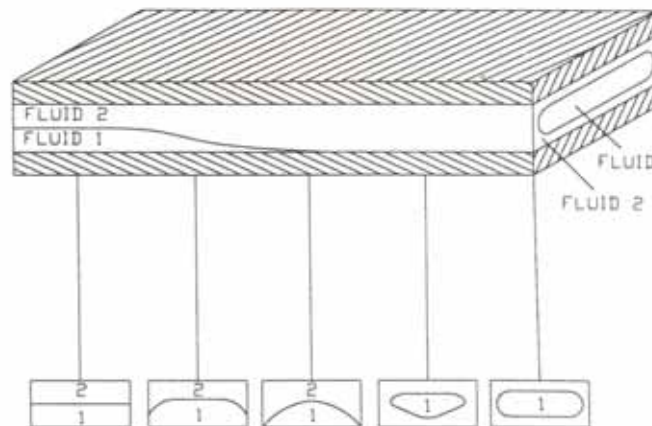
Figure 1-12 Viscous encapsulation in coextrusion flat-die.
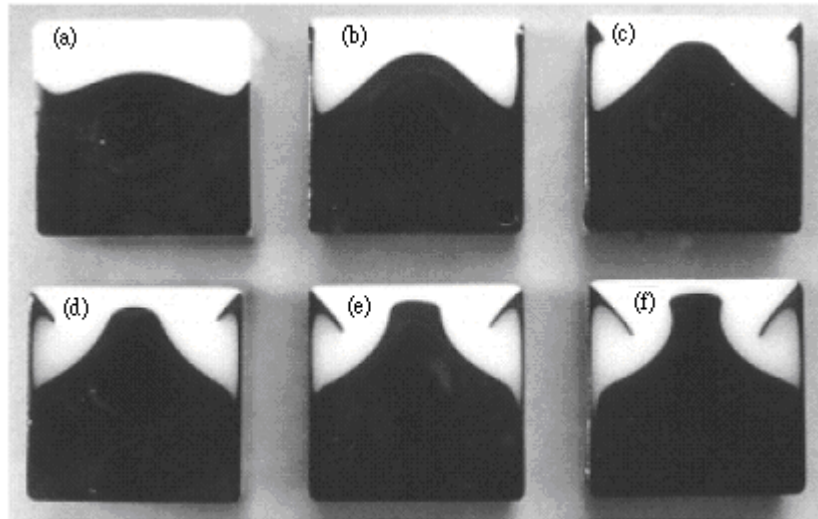
Figure 1-13 Progression of a two-layer polystyrene structure as it flows down a square channel. Cuts at axial distances from the entry (a) 5; (b) 20; (c) 30; (d) 40; (e) 50; (f) 58 cm.
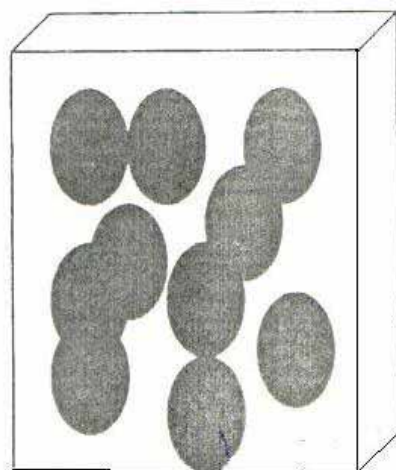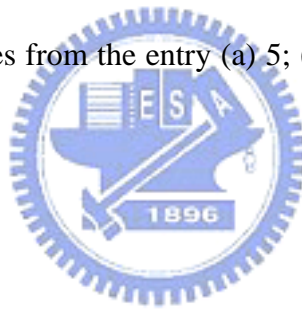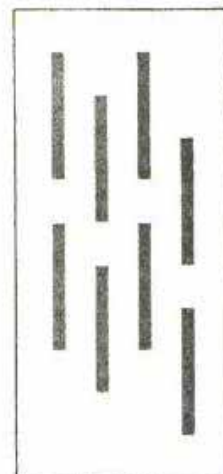
(a)   (b)

Figure 1-14 Multilayer laminar structure by blending process. (a) top view; (b) side view.

Chapter 2

Tensile Behavior of HDPE, PA-6, and Three-Layer

HDPE/tie/PA-6 Films

2.1 Introduction

It is becoming increasingly more common to prepare multilayer structures from different polymers to give materials that have multiple properties; i.e., by taking advantage of the best property of each individual component. Such multilayer extruded products are normally produced by coextrusion into multilayer sheets, blown films, cast films, tubes, and containers [1–6].

Polyethylene (PE) and polyamide 6 (PA-6), which are very popular in the packaging industry, are two important polymers often used in coextrusion processes. PE is employed widely because of its low price, easy processibility, chemical inertness, and high barrier property toward moisture, but its poor barrier properties toward oxygen, aromas, and organic solvents limit its applicability [7–10]. On the other hand, PA is a good barrier resin toward oxygen, aromas, and organic solvents and it has high tensile strength and toughness, but it has the drawbacks of being relatively expensive and a poor barrier for water vapor [11–15]. For packaging applications, clearly it is a good idea to combine these two resins into a single structure by using a coextrusion process to form multilayer films that have multiple properties. Because of incompatibility between these two polymers, however, an extrudable adhesive is often incorporated into the multilayer structure as a tie layer in

the coextrusion process. Kamykowski [16] studied the adhesive properties of five-layer coextruded cast films, polypropylene/adhesive/polyamide/adhesive/polypropylene, and found that adhesion generally can be improved upon increasing the overall film thickness or the relative amount of adhesive. Homopolymer diluents in the adhesive layer result in better adhesion relative to random copolymers. The molecular weight of the grafted adhesion polymer has only a small effect on adhesion. Tanaka et al. [17] successfully developed a new generation of tie layer adhesives, which maintain high adhesive strengths after thermoforming and orientation, by combining graft and polymer blending technologies. Adhesion between chemically dissimilar polymers was also introduced by blending the component materials and the adhesive [18–20]. This method not only provides good adhesion but it also eliminates the number of tie layer required in the multilayer process, e.g., the five-layer film coextrusion system can be replaced with a three-layer film comprising ethylene-vinyl alcohol copolymer (EVOH) as the central layer and low-density polyethylene (LDPE)/low-density polyethylene-grafted maleic anhydride (LDPE-g-MAH) blend as the external layers to form a three-layer structure, A/B/A (blend/EVOH/blend) [20].

One of the most important properties required for packaging applications is tensile strength. In this paper, we describe a constitutive equation that can be used to describe the plastic deformation of HDPE, PA-6, and three-layer films of the type HDPE/tie/PA-6. We have also examined the relationship between the mechanical properties of a three-layer film and those of its component layers; an additive rule can be used to predict the characteristics of the three-layer film.

2.2 Experimental

2.2.1 Materials

The materials used in the coextrusion blown-film process were (1) high-density polyethylene (HDPE), (2) polyamide-6 (PA-6), and (3) adhesive, high-density polyethylene-grafted maleic anhydride (HDPE-g-MAH). HDPE was supplied in pellet form (HDPE 9001) by Formosa Plastic Corp. (Taiwan); its melt index (M.I.) is 0.05 g/10 min (190 °C, 2.16 kg) and its density is 0.95 g/cm^3. PA-6 (Novamid 1030) was provided in pellet form by Mitsubishi Engineering Plastic Co. (Japan); its M.I. is 5 g/10 min (240 °C, 2.16 kg) and its density is 1.14 g/cm^3. The adhesive (Modic-AP H503) was obtained in pellet form from Mitsubishi Chemical Corp. (Japan); its M.I. and density are 1.5 g/10 min (190 °C, 2.16 kg) and 0.95 g/cm^3, respectively.

2.2.2 Preparation of Multilayer Films

Because of the hydrophilicity of PA-6, we dried this polymer in a vacuum oven for 12 h at 90 °C before processing. HDPE, PA-6, and HDPE-g-MAH were fed separately into their individual extruders and coextruded through a three-layer coextrusion blown-film die (inner diameter = 97.6 mm; gap thickness = 1.2 mm) at 250 °C. The three-layer film was inflated and cooled with air and stretched using a take-up device after leaving the exit of the die. Monolayers of PA-6 and HDPE films were also prepared using the same blown-film equipment. Four different compositions of the component layers were prepared and the overall thickness of each three-layer multilayer film was ca. 140 μm. Table 2-1 displays the thicknesses and volume fractions of the PA-6 layers; the compositions of all the three-layer films were controlled by using gear pumps precisely and steadily and the individual thicknesses of the component layers of the multilayer product were determined by using an

ultrasonic thickness measurement instrument (Quinsonic, ElektroPhysik). During the

coextrusion process, the tie layer generally was very thin (ca. 5 µm) and the main

molecular structure was HDPE; therefore, in this study we consider the tie layer to be

part of the HDPE layer and neglect its effects on the tensile behavior of the product.

2.2.3 Measuring Tensile Behavior

The uniaxial tensile measurements were conducted using a Hung-Ta Instrument

2102AP with test samples that were 40 mm long and 20 mm wide. Samples were

tested with crosshead speeds of 4, 40, and 400 mm/min at a temperature of 25 °C and

a relative humidity of 50%. Engineering stress–strain curves were determined from

load-extension data based on the original geometry of the test sample. Measurements

were taken on five replicate samples; average values are reported.

We calculated the engineering stress and strain by considering the original

geometry of the sample films; in fact, however, the cross-sectional area of a film

sample changed continuously during the deformation process. The engineering stress

and strain cannot represent the actual stress and strain at any one instance; it is

necessary to plot the true stress–strain curves to describe the tensile behavior. If the

deformation behavior was homogeneous, and a constant volume is assumed during

deformation, we calculated the true strain, ε_T, and the true stress, σ_T, by

$$\varepsilon_T = \ln(1 + \varepsilon_E) \tag{2.1}$$

$$\sigma_T = \sigma_E (1 + \varepsilon_E) \tag{2.2}$$

where ε_E and σ_E are the engineering strain and the engineering stress, respectively

[22,23]. On the other hand, when the deformation was heterogeneous, i.e., a neck

formed, we marked the surface of each sample film with a set of 199 points, which

were positioned 0.2 mm apart along the 40-mm gauge length of the specimen, before

testing [23]. The evolution of the specimen profile during a test was recorded continuously during the measurement using a CCD video camera, which was connected to a computer and coupled with a microscope mounted on a screw-driven device. The true stress and strain were determined by measuring the local deformation in the neck region from photographs obtained by a frame grabber during the experiment. Assuming that the sample maintained a constant volume during deformation, the true stress and true strain were calculated by

$$\varepsilon_T = \ln(1 + \varepsilon_L) \tag{2.3}$$

$$\sigma_T = \sigma_{eng}(1 + \varepsilon_L) \tag{2.4}$$

where ε_L is the longitudinal strain of the displacement between two markers in the neck region. These markers were monitored along the central axis; the cross section of the sample was rectangular, so that the effect of triaxiality during necking could be ignored [23, 24].
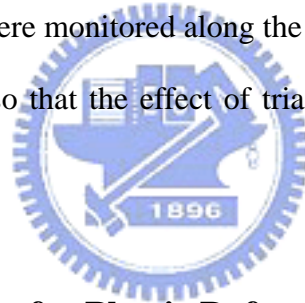
2.3 Constitutive Equation for Plastic Deformation

The constitutive equation that describes the plastic deformation for thermoplastics was first proposed by G'Sell and Jonas [25] in the following form:

$$\sigma_T = K \cdot \exp\left(\frac{\gamma}{2} \cdot \varepsilon_T\right) \cdot \dot{\varepsilon}_T^{\ m} \tag{2.5}$$

$$\gamma = \gamma_\varepsilon \cdot \varepsilon_T \tag{2.6}$$

where σ_T and ε_T are the true stress and strain, respectively, K and γ_ε are constants, $\dot{\varepsilon}_T$ is true strain rate, and γ and m are the strain hardening coefficient and the strain rate sensitivity, respectively. The parameters γ and m are defined [26] as:

$$m \equiv \left(\frac{\partial \ln \sigma_T}{\partial \ln \dot{\varepsilon}_T} \right)_{\varepsilon_T} \tag{2.7}$$

$$\gamma \equiv \left(\frac{\partial \ln \sigma_T}{\partial \varepsilon_T} \right)_{\dot{\varepsilon}_T} \tag{2.8}$$

Equation (2.5), which incorporates the influence of the strain rate into the strain hardening equation [27], has been used to describe the plastic deformation of ductile metals. To calculate the parameters of the constitutive equation, G'Sell et al. employed an hourglass-shaped test specimen and developed a sophisticated procedure in which the strain was measured at the narrowest part of the specimen by passing a taut wire around its circumference [25] and monitoring it using a video interface [28]. A constant true strain rate, denoted $\dot{\varepsilon}_T$, is then maintained by regulating the crosshead speed using a computer through these two interfaces. By applying these two techniques, the parameter m could be obtained as the slope of the linear relationship of the natural logarithm of true strain rate ($\ln \dot{\varepsilon}_T$) versus the natural logarithm of true stress ($\ln \sigma_T$) curve at constant strain; the parameters γ_ε and K could also be obtained as the slope and intercept, respectively, of the plot of the linear relationship between the natural logarithm of $(\sigma_T / \dot{\varepsilon}_T{}^m)$ versus the square of ε_T at constant strain rate. In this study, we made an effort to obtain the parameters of the equation from the engineering data by using only a conventional tensile machine and a CCD video camera without any aiding interface. The detailed procedure is described in a later section below.

First, we transformed Equation (2.5) into the form of a natural logarithm:

$$\ln \sigma_T = \ln K + \frac{\gamma_\varepsilon}{2} \cdot \varepsilon_T^2 + m \cdot \ln \dot{\varepsilon}_T \tag{2.9}$$

where $\dot{\varepsilon}_T = \dfrac{d\varepsilon_T}{dt} = \dfrac{d\varepsilon_T}{d\varepsilon_E} \cdot \dfrac{d\varepsilon_E}{dt}$ for homogeneously deformation   (2.10)

and $\dot{\varepsilon}_T = \dfrac{d\varepsilon_T}{dt} = \dfrac{d\varepsilon_T}{d\varepsilon_E} \cdot \dfrac{d\varepsilon_L}{dt}$ for inhomogeneously deformation (2.11)

Substituting Equations (2.1) and (2.10) into Equation (2.9):

$$\ln \sigma_T = \ln K + \frac{\gamma_\varepsilon}{2} \cdot \varepsilon_T{}^2 + m \cdot \ln(\frac{1}{1+\varepsilon_E} \cdot \frac{d\varepsilon_E}{dt})$$

$$= \ln K + \frac{\gamma_\varepsilon}{2} \cdot \varepsilon_T{}^2 + m \cdot \ln(\frac{1}{1+\varepsilon_E}) + m \cdot \ln \frac{d\varepsilon_E}{dt}$$

$$= \frac{\gamma_\varepsilon}{2} \cdot \varepsilon_T{}^2 - m \cdot \ln(1+\varepsilon_E) + m \cdot \ln \frac{d\varepsilon_E}{dt} + \ln K$$

Hence, $\ln \sigma_T = \dfrac{\gamma_\varepsilon}{2} \cdot \varepsilon_T{}^2 - m \cdot \varepsilon_T + \ln K + m \cdot \ln \dot{\varepsilon}_E$ (2.12)

We also treated Equation (2.11) with the same procedure we applied to Equation (2.10) to obtain the following result:

$$\ln \sigma_T = \frac{\gamma_\varepsilon}{2} \cdot \varepsilon_T{}^2 - m \cdot \varepsilon_T + \ln K + m \cdot \ln \dot{\varepsilon}_L \qquad (2.13)$$

where $\dot{\varepsilon}_E = \dfrac{d\varepsilon_E}{dt}$ is the engineering strain rate for homogeneous deformation, which

can be calculated from the crosshead speed and the original gauge length and

$\dot{\varepsilon}_L = \dfrac{d\varepsilon_L}{dt}$ is the longitudinal strain rate in the neck region for inhomogeneous

deformation calculated from the measured data and time. Thus, using this mathematical approach, we transformed Equation (2.5) into the second-order polynomial equations, Equations (2.12) and (2.13), each of which has the form of a quadratic equation [Equation (2.14)].

$$y = ax^2 + bx + c \qquad (2.14)$$

Fitting Equations (2.12) and (2.13) to the data of the plot of $\ln\sigma_T$ versus ε_T by a least-squares approximation allows all of the parameters, including K, m and γ_ε, to be

obtained:

$$a = \frac{\gamma_\varepsilon}{2}, \ b = -m, \ c = \ln K + m \cdot \ln \dot\varepsilon_E \quad \text{for homogeneous deformation (2.15)}$$

$$a = \frac{\gamma_\varepsilon}{2}, \ b = -m, \ c = \ln K + m \cdot \ln \dot\varepsilon_L \quad \text{for inhomogeneous deformation (2.16)}$$

2.4 Results and Discussion

Figure 2-1 presents the engineering stress–strain curves for the monolayer films of HDPE recorded at three crosshead speeds (4, 40, and 400 mm/min). We observe that the HDPE film deforms inhomogeneously at these crosshead speeds; a significant load drop occurs; it is associated with the formation of a stable neck at the central cross-section. The load drop is followed by the cold drawing process, which is associated with neck propagation along the specimen. At a high level of strain, the engineering stress increases rapidly with increasing engineering strain arising from the molecular alignment [29]. The true stress–strain curves for HDPE films at various crosshead speeds were determined by measuring the local strain at the neck region and applying Equations (2.3) and (2.4). Figure 2-2 displays the true stress–strain curves of the HDPE films at the three crosshead speeds. Figure 2-3 displays both the experimental data and the fitted curves of $\ln\sigma_T$ versus ε_T recorded at various crosshead speeds. A reasonable second-order polynomial relationship exists for the HDPE film over the range of true strains from 0.45 to 2.4 (correlation coefficients are all > 0.98) after the least-squares approximation. We calculated the corresponding parameters of Equation (2.5) for the HDPE film at the various crosshead speeds using Equation (2.16); Table 2-2 summarizes the results. We observe that, upon increasing the crosshead speed, γ_ε decreases, m does not change significantly, and K increases. Figure 2-4 displays the results of applying the parameters to Equation (2.5); we

obtained the modeling curves for the true stress–strain, where we estimated the true strain rate by constructing a plot of true strain versus time. When the deformation was homogeneous, the time was obtained from the extension rate and the true strain rate was taken as the slope in the strain range of plastic deformation, 0.45–2.4, as presented in Figure 2-5. When a neck was formed, the time was obtained directly from the video recording, and the true strain rate was taken as the highest slope of the plot of the true strain versus time [30]. The HDPE film deformed inhomogeneously at all crosshead speeds; Table 2-3 lists the true strain rates at the various crosshead speeds. To allow comparisons to be made between the experimental data and the fitted results, Figure 2-4 also displays the experimental true stress–strain data. We observe that a good correlation exists between the modeling curves and the experimental data in the range of plastic deformation of the HDPE films.

Figure 2-6 indicates that the PA-6 film displays obviously different tensile behavior when compared to the HDPE film. The PA-6 film exhibits a higher level of engineering stress and deforms homogeneously at the lower crosshead speeds, i.e., 4 and 40 mm/min. At higher levels of strain, in common with the results for the HDPE film, the engineering stress increases rapidly upon increasing the engineering strain as a result of molecular alignment; the true stress–strain curve was determined using Equations (2.1) and (2.2). At the highest crosshead speed (i.e., 400 mm/min), however, the deformation mode changes from homogeneous to inhomogeneous and the true stress–strain curve was calculated, as it was for the HDPE film, by using Equations (2.3) and (2.4). As indicated in Figure 2-7, a reasonable second-order polynomial relationship appears to exist in the plot of $\ln\sigma_T$ versus ε_T for the PA-6 film over the range of true strains from 0.45 to 1.8 (correlation coefficients are all > 0.98) after the least-squares approximation. Table 2-2 summarizes the corresponding parameters of Equation (2.5) for the PA-6 film at the various crosshead speeds, which we calculated

using Equation (2.15) for crosshead speeds of 4 and 40 mm/min and Equation (2.16) for the crosshead speed of 400 mm/min. As shown in Table 2-2, the value of γ_ε decreases upon increasing the crosshead speed, but the values of m and K increase. Figure 2-8 presents a comparison between the experimental true stress–strain curves and those obtained by modeling; Table 2-3 lists the true strain rate used to calculate the modeling curves. A good agreement also exists between the experimental and modeled data over the range of plastic deformation of the PA-6 films.

Figure 2-9 presents a plot of the engineering and true stress–strain curves of the three-layer films containing various volume fractions of PA-6 at a crosshead speed of 40 mm/min. It is clear that all of these curves lie between those obtained for the monolayer HDPE and PA-6 films. The stress level increases upon increasing the volume fraction of the PA-6 layer. In the range of volume fractions of PA-6 that we investigated, all of the three-layer films deform inhomogeneously at the crosshead speed. As shown in Figure 2-10(a), a reasonable second-order polynomial relationship appears to exist in the plot of $\ln\sigma_T$ versus ε_T for the three-layer film over the range of true strains from 0.45 to 2.1 (correlation coefficients are all > 0.98) after the least-squares approximation, as it did for both the HDPE and PA-6 films at a crosshead speed 40 mm/min. None of the three-layer films fractured when the experiments were terminated at a true strain of 2.1. Table 2-2 also presents the corresponding parameters of the constitutive equation for the three-layer films recorded at various crosshead speeds. As we observe in Table 2-2, the value of γ_ε decreases upon increasing the crosshead speed, but the values of m and K both increase, and the values of all of these parameters lie between those obtained when using the HDPE and PA-6 films. Figure 2-10(b) presents a comparison of the modeling curves and experimental true stress–strain data obtained at a crosshead speed of 40 mm/min; Table 2-3 lists the true strain rates of the three-layer films at

various volume fractions of PA-6 that we used to model the curves. Good agreements also exist, as they did for the HDPE and PA-6 films, between the experimental data and the modeling curves over the range of plastic deformation for the three-layer films having various volume fractions of PA-6.

To determine whether there is a relationship between the properties of the three-layer films and its component layers (HDPE and PA-6), we employed an additive rule [21] to examine them:

$$\sigma_M = \alpha_{HDPE}\,\sigma_{HDPE} + \alpha_{PA-6}\sigma_{PA-6} \qquad (2.17)$$

where σ_M is the true stress of a three-layer film, σ_{HDPE} and σ_{HPA-6} are the true stresses of the HDPE and PA-6 layers, respectively, and α_{HDPE} and α_{PA-6} are the volume fractions of the HDPE (including the tie layer) and PA-6 layers, respectively.

From Equations (2.5) and (2.17), we determine that the relationship between the true stress–strain of the three-layer and individual component layer films is:

$$K_M \exp(\frac{\gamma_{\varepsilon M}}{2} \cdot \varepsilon_T^2) \cdot \overset{\bullet}{\varepsilon_T}{}^{m_M} =$$

$$\alpha_{HDPE} K_{HDPE} \exp(\frac{\gamma_{\varepsilon HDPE}}{2} \cdot \varepsilon_T^2) \cdot \overset{\bullet}{\varepsilon_T}{}^{m_{HDPE}} + \alpha_{PA-6} K_{PA-6} \exp(\frac{\gamma_{\varepsilon PA-6}}{2} \cdot \varepsilon_T^2) \cdot \overset{\bullet}{\varepsilon_T}{}^{m_{PA-6}}$$

$$(2.18)$$

where K_M and $\gamma_{\varepsilon M}$ are constants for the three-layer film; m_M is the strain rate sensitivity of the three-layer film; K_{HDPE} and $\gamma_{\varepsilon HDPE}$ are constants for the HDPE film; m_{HDPE} is the strain rate sensitivity of the HDPE film; K_{PA-6} and $\gamma_{\varepsilon PA-6}$ are constants for the PA-6 film; and m_{PA-6} is the strain rate sensitivity of the PA-6 film.

The strain hardening coefficient, γ_M, and strain rate sensitivity, m, of the three-layer film are defined [26] as:

$$\gamma_M(\varepsilon) = \frac{1}{\sigma_M}\frac{\partial \sigma_M}{\partial \varepsilon} \qquad (2.19)$$

$$m_M = \frac{\dot{\varepsilon}_M}{\sigma_M} \frac{\partial \sigma_M}{\partial \dot{\varepsilon}} \qquad (2.20)$$

From Equations (2.6), (2.18) and (2.19), the relationship between the constants, γ_ε, of the three-layer and individual component layer films is

$$\gamma_{\varepsilon M} = \frac{\gamma_{\varepsilon HDPE}\, \alpha_{HDPE}\, \sigma_{HDPE} + \gamma_{\varepsilon PA-6} \alpha_{PA-6} \sigma_{PA-6}}{\alpha_{HDPE}\, \sigma_{HDPE} + \alpha_{PA-6} \sigma_{PA-6}} \qquad (2.21)$$

From Equations (2.18) and (2.20), the relationship of between the strain rate sensitivities, m, of the three-layer and individual component layer films is

$$m_M = \frac{m_{HDPE}\, \alpha_{HDPE}\, \sigma_{HDPE} + m_{PA-6} \alpha_{PA-6} \sigma_{PA-6}}{\alpha_{HDPE}\, \sigma_{HDPE} + \alpha_{PA-6} \sigma_{PA-6}} \qquad (2.22)$$

From Equations (2.21) and (2.22), we observe that both the constants of the HDPE and PA-6 films are weighting factors that can be used to calculate the corresponding two constants of the three-layer films. We also wished to examine the relationship between the constant K of the three-layer film and those of its component layers by using the additive rule. In this study, we employed two forms of the additive rule to calculate the value of K for the three-layer film based on those values of its component parts:

$$\ln K_M = \alpha_{HDPE}\, \ln K_{HDPE} + \alpha_{PA-6}\, \ln K_{PA-6} \qquad (2.23)$$

$$K_M = \alpha_{HDPE}\, K_{HDPE} + \alpha_{PA-6} K_{PA-6} \qquad (2.24)$$

Figure 2-11 indicates that a better agreement exists between the experimental data and the values calculated using the additive rule based on Equation (2.23) than that based on Equation (2.24).

We calculated the parameters, γ_M, m, and K, of the three-layer films having various volume fractions of PA-6 by the additive rule using the parameters of the individual component layers listed in Table 2-2. Figures 2-12~2-14 present the relationship

between these parameters obtained by the additive rule and those obtained experimentally (from Table 2-2) with respect to the compositions of films. Good agreements exist between the experimental data and the results using the additive-rule model for both the strain hardening parameter and the true yield stress at low crosshead speeds, which suggests that this rule can be used to accurately predict the plastic deformation of the three-layer films. A larger discrepancy exists, however, between the modeled and experimental data for both these parameters of the three-layer films at the highest crosshead speed. This discrepancy is due to the generation of heat during the deformation process [31]; heat would cause a decrease in the stress required to produce a given strain and would result in a discrepancy between the experimental data and that obtained using the additive rule.

2.5 Conclusions

In this study, we successfully fabricated HDPE/tie/PA-6 three-layer films, having a typical A/B/C multilayer structure, by a coextrusion blown-film process. We investigated the plastic deformation behavior of the component layer films and the three-layer films. The PA-6 films deformed homogeneously at low crosshead speeds, but deformed inhomogeneously at the highest crosshead speed. On the other hand, the HDPE and three-layer films all deformed inhomogeneously at each crosshead speed we studied. We employed a constitutive equation to describe the tensile behavior of the films over the range of plastic deformation. The tensile behavior of the component layers and multilayer films at various crosshead speeds can be expressed precisely by using a constitutive equation that has three parameters in the true stress–strain relationship: γ_M, m, and K. We examined the relationships between the parameters of the monolayers of the component layers and those of the three-layer films by using an

additive rule. By using the rule, we can also predict—with good agreements in the true stress–strain relationship—the tensile behavior of the three-layer film from that of each individual component, but a larger discrepancy exists between the modeled and experimental data at high crosshead speed because heat is generated during the deformation process.

2.6 References

1. J. Culter, J. Krohn, and W. Todd, *Pack. Tech. Eng.*, **8**, 30 (1999).

2. J. Dooley, K. S. Hyun, and K. Hughes, *Polym. Eng. Sci.*, **38**, 1060 (1998).

3. W. J. Schrenk and S. A. Marcus, *J. Plast. Film Sheet.*, **1**, 30 (1985).

4. S. Hosoda, Y. Seki, and H. Kihara, *Polymer*, **34**, 4602 (1993).

5. S. J. Liu and C. H. Yang, *Adv. Polym. Tech.*, **20**, 108 (2001).

6. J. M. De Gooijer, M. Scheltus, and C. E. Koning, *Polym. Eng. Sci.*, **41**, 86 (2001).

7. F. Hensen, Plastics Extrusion Technology, Hanser, New York, 1997 (Chapter 5).

8. Rubin II, Handbook of Plastic Materials and Technology, Wiley, New York, 1990 (Chapter 30).

9. M. B. Sabne, S. M. Thombre, A. S. Patil, S. D. Patil, S. B. Idage, and S. P. Vernekar, *J. Appl. Polym. Sci.*, **58**, 1275 (1995).

10. C. Gagnard, Y. Germain, P. Keraudren, and B. Barriere, *J. Appl. Polym. Sci.*, **90**, 2727 (2003).

11. D. C. Climenhage, *Packaging*, **32**, 39 (1987).

12. S. Eichler and J. Miltz, *J. Appl. Polym. Sci.*, **50**, 2095 (1993).

13. Rubin II, Handbook of Plastic Materials and Technology, Wiley, New York, 1990 (Chapter 16).

14. Y. P. Khanna, E. D. Day, M. L. Tsai, and G. Vaidyanathan, *J. Plast. Film Sheet.*, **13**,

197 (1997).

15. S. Bianchi, S. Cantagallo, G. Consolati, M. Laporta, M. Pegoraro, G. Tieghi, and L. Zanderighi, *J. Appl. Polym. Sci.*, **86**, 559 (2002).

16. G. W. Kamykowski, *J. Plast. Film Sheet.*, **16**, 237 (2000).

17. H. Tanaka, H. Shigemoto, and H. Kawchi, *J. Plast. Film Sheet.*, **12**, 279 (1996).

18. S. S. Valdes, F. O. Villarreal, M. L. Quintanilla, I. Y. Flores, and L. F. Ramos de Valle, Polym. Eng. Sci., **38**, 127 (1998).

19. J. V. Olmos, S. S. Valdes, I. G. Y. Flores, *Polym. Eng. Sci.*, **39**, 1597 (1999).

20. C. H. Huang, J. S. Wu, C. C. Huang, and L. S. Lin, *Polym. J.*, **35**, 978 (2003).

21. W. J. Schrenk and T. Alfrey, *Polym. Eng. Sci.*, **9**,393 (1969).

22. M. Al-Hussein and G. Strobl, *Macromolecules*, **35**, 8515 (2002).

23. C. G'Sell, N. A. Aly-Helal, and J. J. Jonas, *J. Mater. Sci.*, **18**, 1731 (1983).

24. G. Buisson and K. Ravi-Chandar, *Polymer*, **31**, 2071 (1990).

25. C. G'Sell and J. J. Jonas, *J. Mater. Sci.*, **14**, 583 (1979).

26. E. W. Hart, *Acta Metall.*, **15**, 351 (1967).

27. S. Bahadur, *Polym. Eng. Sci.*, **13**, 266 (1973).

28. C. G'Sell, J. M. Hiver, A. Dahoun, and A. Souahi, J. Mater. Sci., **27**, 5031 (1992).

29. A. Peterlin, *J. Mater. Sci.*, **6**, 490 (1971).

30. V. Gaucher-Miri, G. K. Jones, R. Kaas, A. Hiltner, and E. Baer, *J. Mater. Sci.*, **37**,2635 (2002).

31. I. H. Hall, *J. Appl. Polym. Sci.*, **12**, 739 (1968).

Table 2-1 Thickness and volume fraction of the PA-6 layer in each three-layer film.

Thickness of PA-6 layer (μm)	Volume fraction of PA-6 layer (%)
14	10
28	20
42	30
63	45

Table 2-2 The parameters K, γ_ε, and m of the constitutive equation for the HDPE,

PA-6, and three-layer films recorded at various crosshead speeds.

Volume fraction of	Crosshead Speed (mm/min)								
	4			40			400		
PA-6 layer (%)	K	γ_ε	m	K	γ_ε	m	K	γ_ε	m
0 (HDPE)	36.67	0.70	0.028	40.12	0.64	0.024	43.54	0.62	0.029
10	38.34	0.88	0.028	42.60	0.82	0.028	45.74	0.77	0.038
20	43.02	1.03	0.029	46.53	0.94	0.035	47.31	0.85	0.045
30	44.26	1.16	0.032	50.15	1.03	0.039	52.14	0.96	0.048
45	50.31	1.27	0.030	56.26	1.15	0.043	57.42	1.02	0.054
100 (PA-6)	70.24	1.46	0.031	87.77	1.36	0.049	97.52	1.26	0.072

Table 2-3 True strain rates $\dot{\varepsilon}_T$ (1/s) of the HDPE, PA-6, and three-layer films recorded at various crosshead speeds.

Volume fraction of PA-6 layer (%)	Crosshead speed (mm/min)		
	4	40	400
	$\dot{\varepsilon}_T$	$\dot{\varepsilon}_T$	$\dot{\varepsilon}_T$
0 (HDPE)	0.0040	0.030	0.40
10	0.0030	0.025	0.40
20	0.0030	0.023	0.40
30	0.0025	0.020	0.37
45	0.0020	0.020	0.35
100 (PA-6)	0.0007	0.0049	0.30
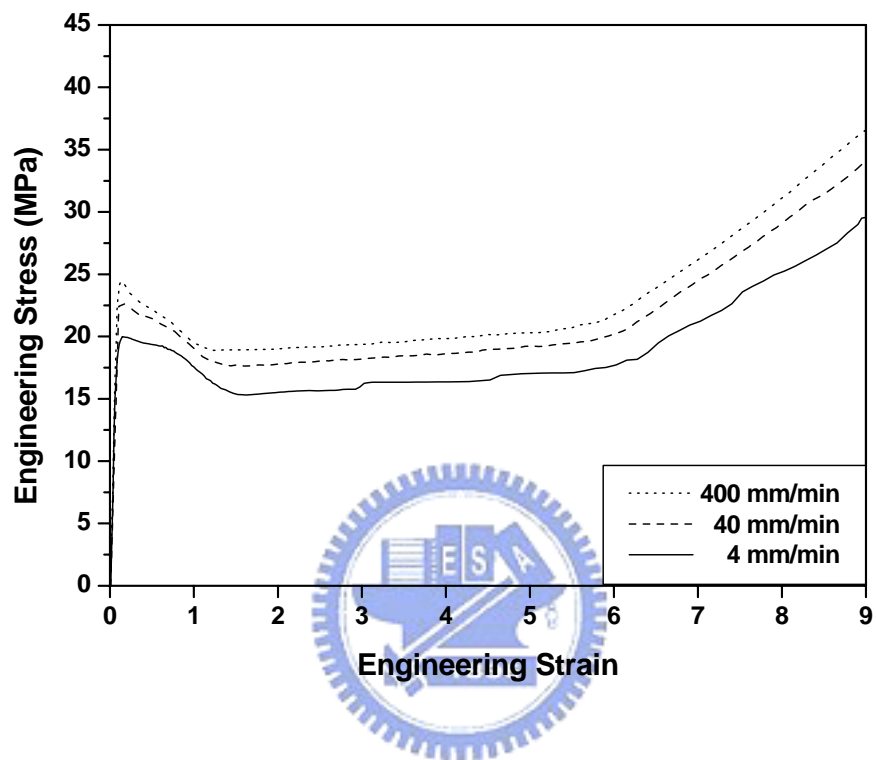
Figure 2-1 Engineering stress–strain curves of the HDPE film recorded at various
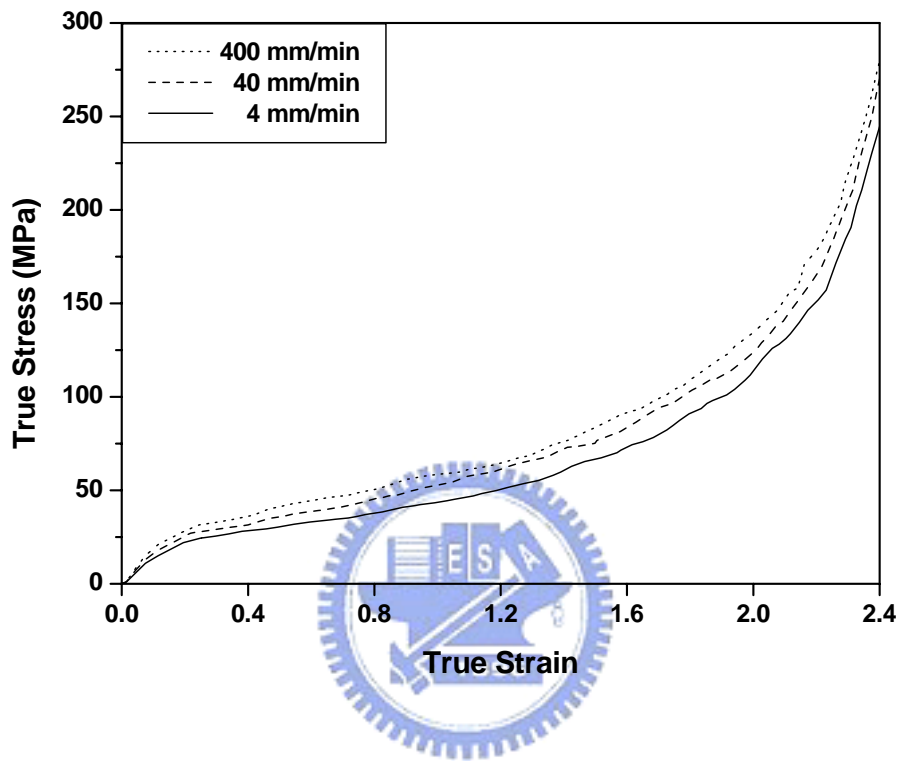
crosshead speeds.

Figure 2-2 True stress–strain curves of the HDPE film recorded at various crosshead speeds.
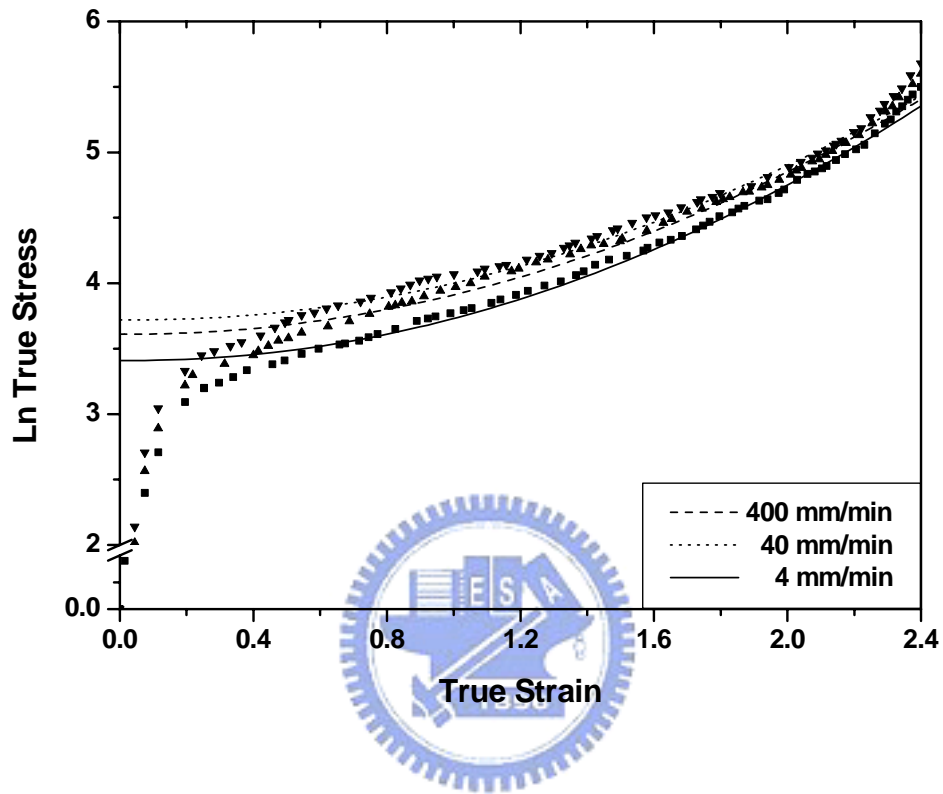
Figure 2-3 Modeling the value of ln(true stress)-strain of the HDPE film at various crosshead speeds.
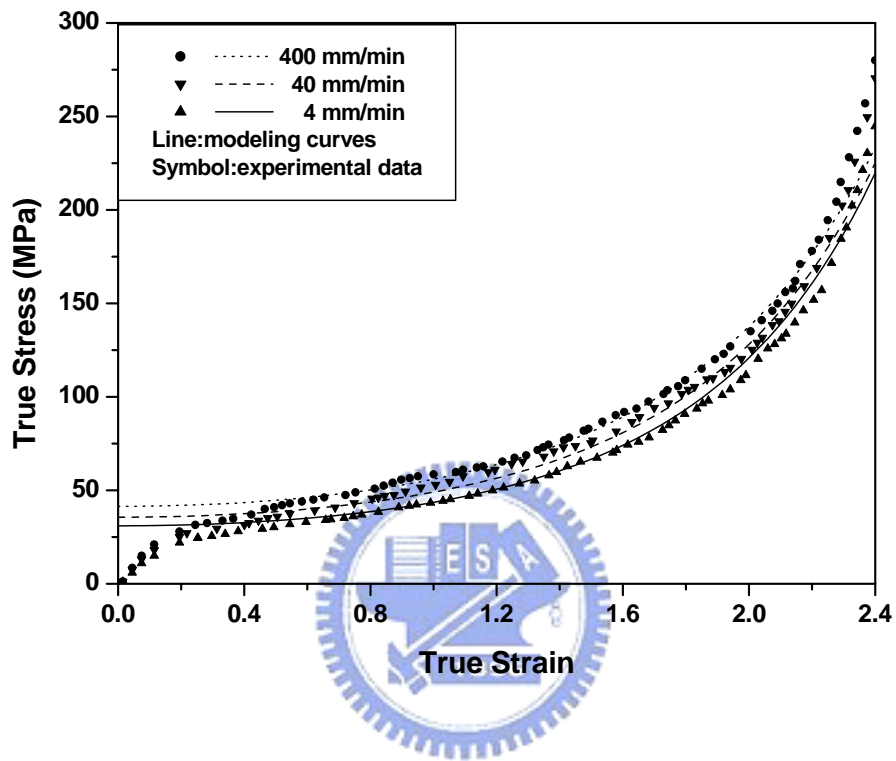
Figure 2-4 Comparison between the modeling curves and the experimental true

stress–strain data for the HDPE film recorded at various crosshead speeds.
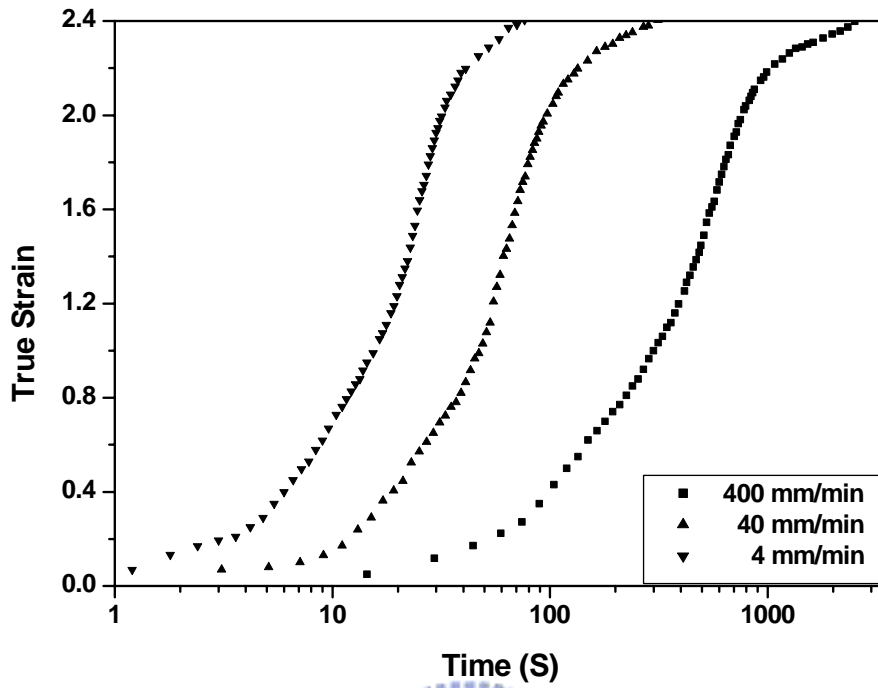
Figure 2-5 True strain as a function of time for the HDPE film recorded at various
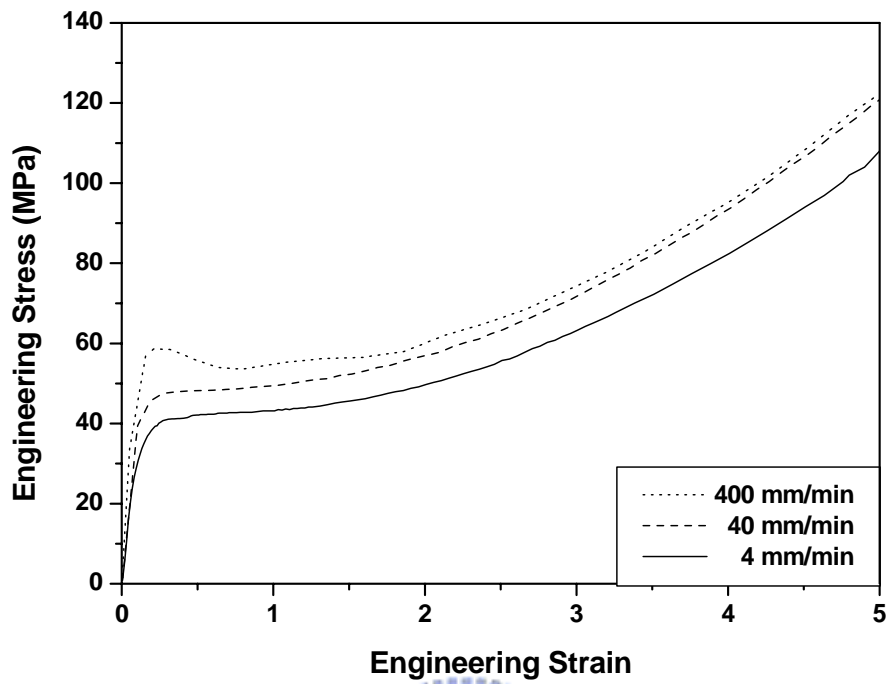
crosshead speeds.

Figure 2-6 Engineering stress–strain curves of the PA-6 film recorded at various
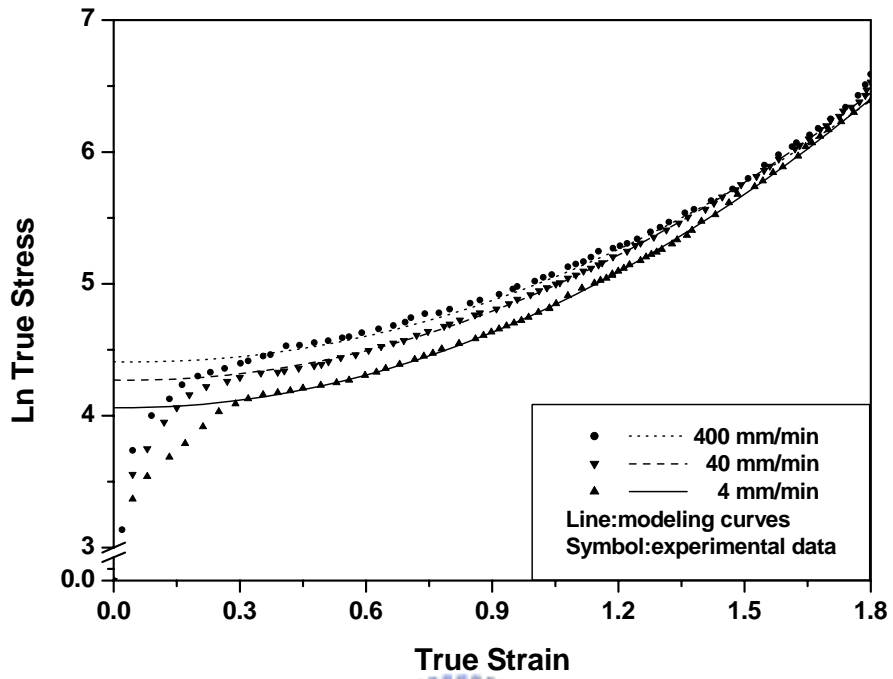
crosshead speeds.

Figure 2-7 Modeling the value of ln(true stress)-strain of the PA-6 film at various

crosshead speeds.
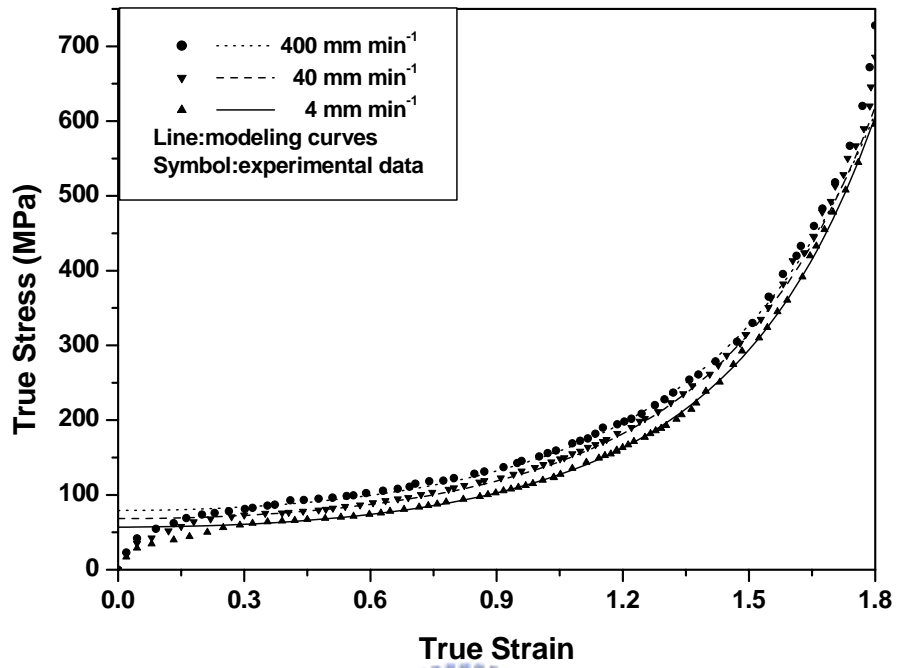
Figure 2-8 Comparison between the modeling curves and the experimental true

stress–strain data for the PA-6 film.
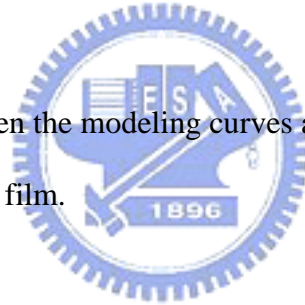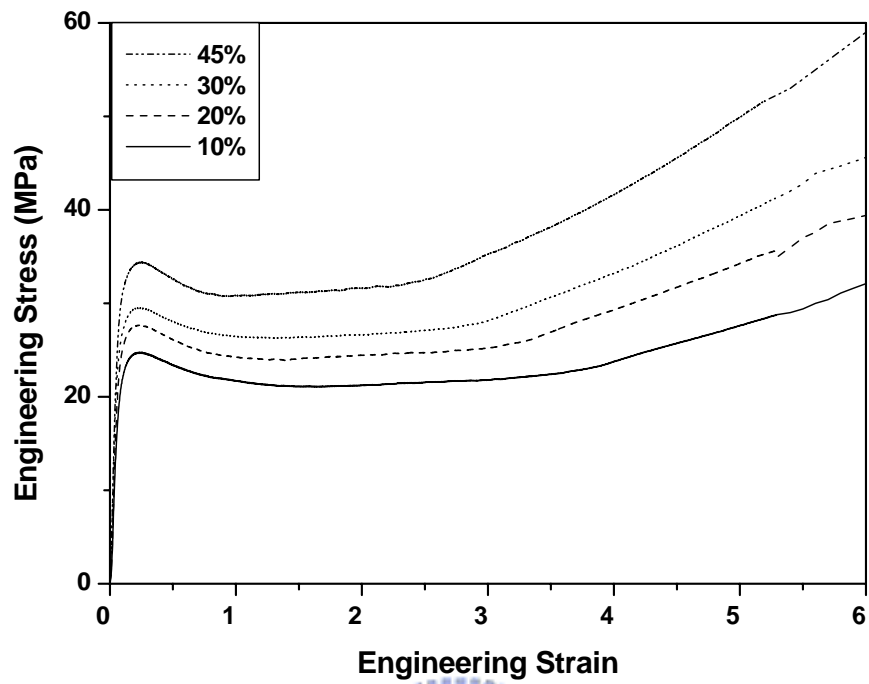
Figure 2-9 Engineering stress–strain curves of the three-layer films, having various

volume fractions of PA-6, recorded at a crosshead speed of 40 mm/min.
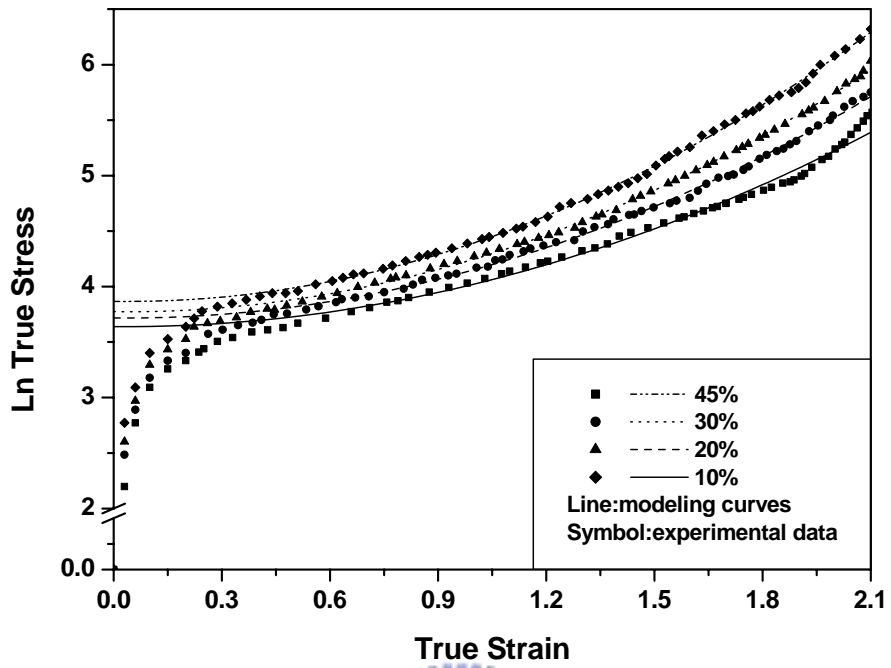
Figure 2-10(a) Modeling curves of ln(true stress)-true strain and experimental data

recorded at a crosshead speed of 40 mm/min.

Figure 2-10(b) Modeling curves of true stress-true strain and experimental data

recorded at a crosshead speed of 40 mm/min.
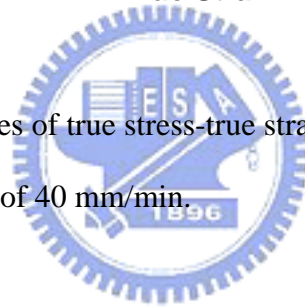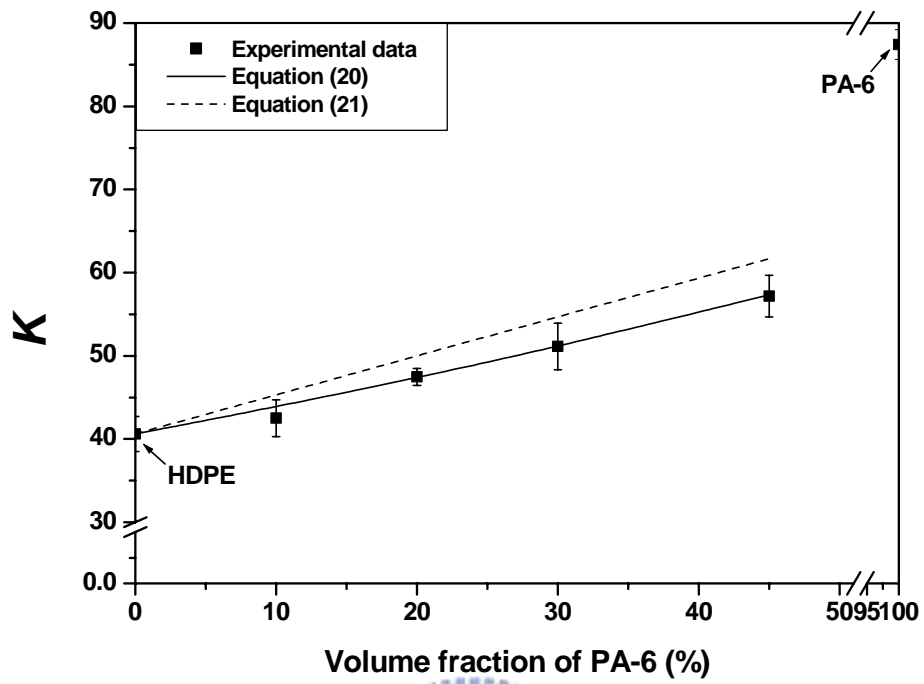
Figure 2-11 Comparisons of the relationships between Equations (20) and (21) and the experimental data.
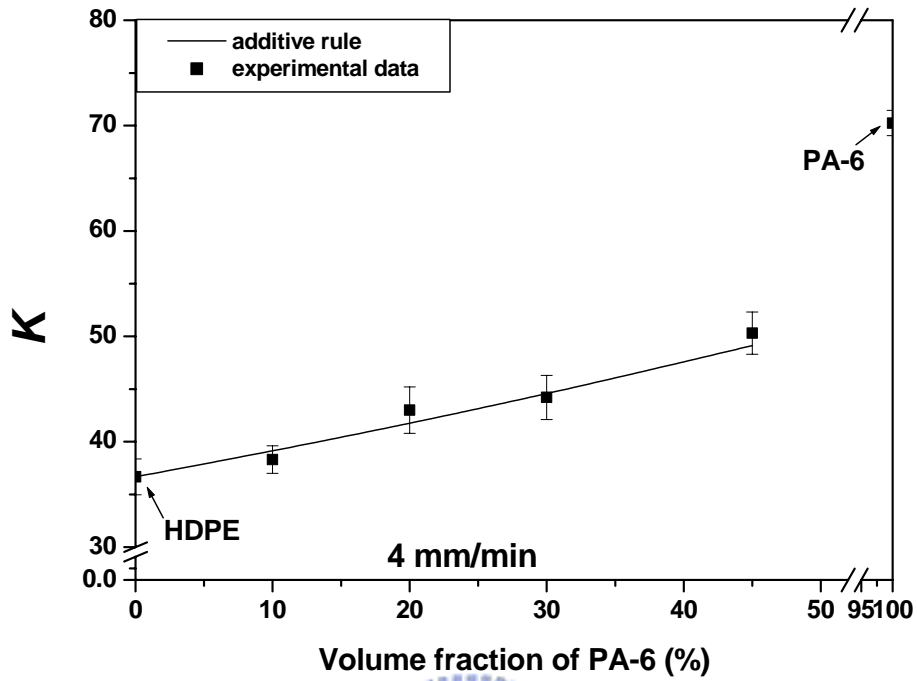
Figure 2-12(a) Comparison between the values of *K* of the three-layer films, having various volume fractions of PA-6, determined using the additive rule and that from the experimental data at crosshead speeds of 4 mm/min.
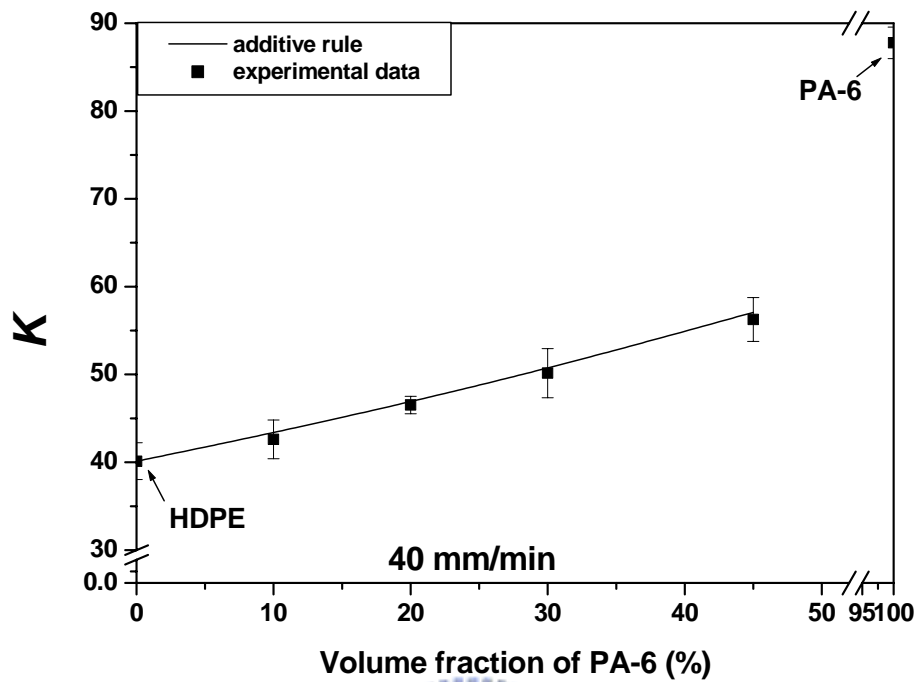
Figure 2-12(b) Comparison between the values of *K* of the three-layer films, having various volume fractions of PA-6, determined using the additive rule and that from the experimental data at crosshead speeds of 40 mm/min.
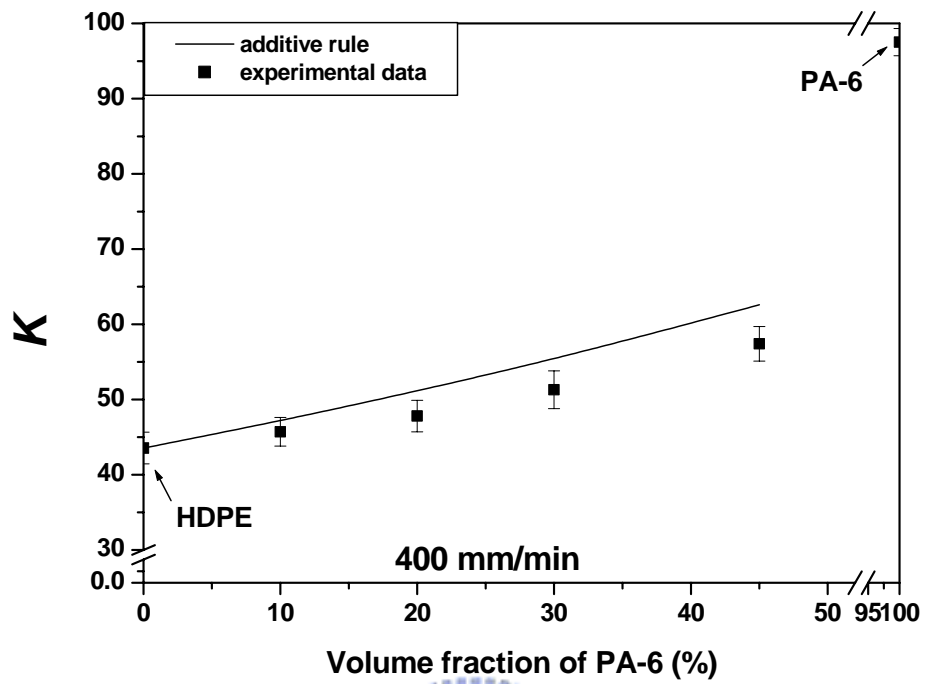
Figure 2-12(c) Comparison between the values of K of the three-layer films, having various volume fractions of PA-6, determined using the additive rule and that from the experimental data at crosshead speeds of 400 mm/min.
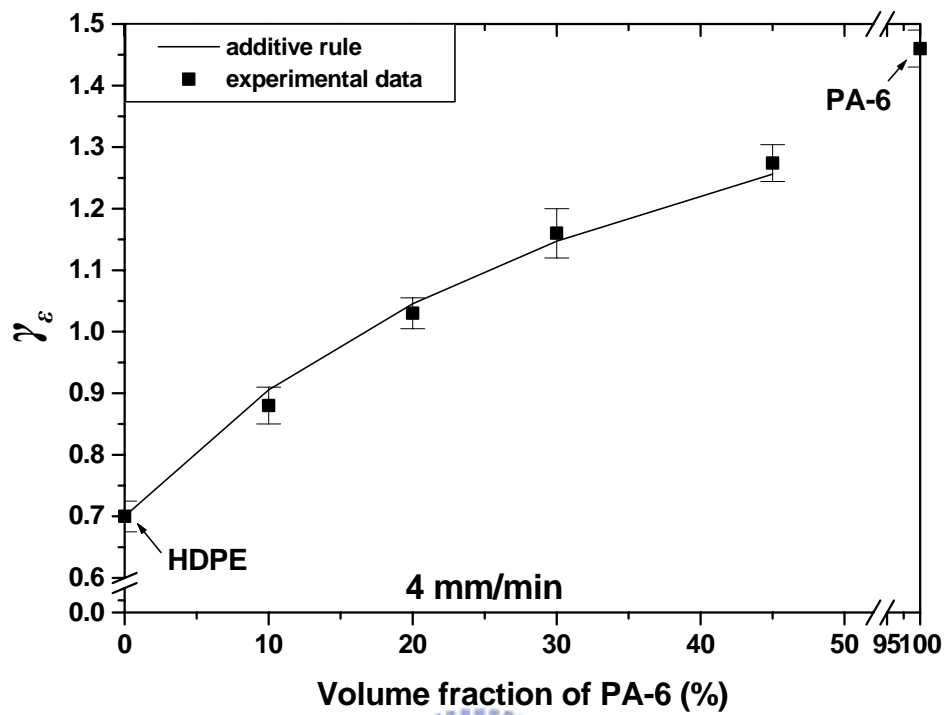
Figure 2-13(a) Comparison between the values of γ_ε of the three-layer films, having various volume fractions of PA-6, determined using the additive rule and that from the experimental data at crosshead speeds of 4 mm/min.
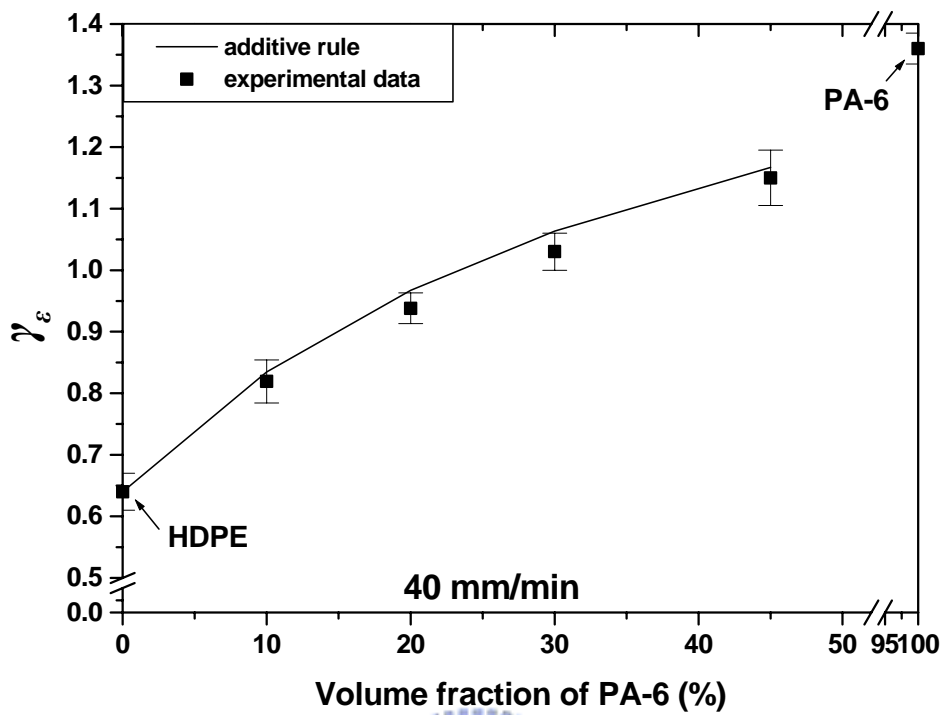
Figure 2-13(b) Comparison between the values of γ_ε of the three-layer films, having

various volume fractions of PA-6, determined using the additive rule and that from the

experimental data at crosshead speeds of 40 mm/min.
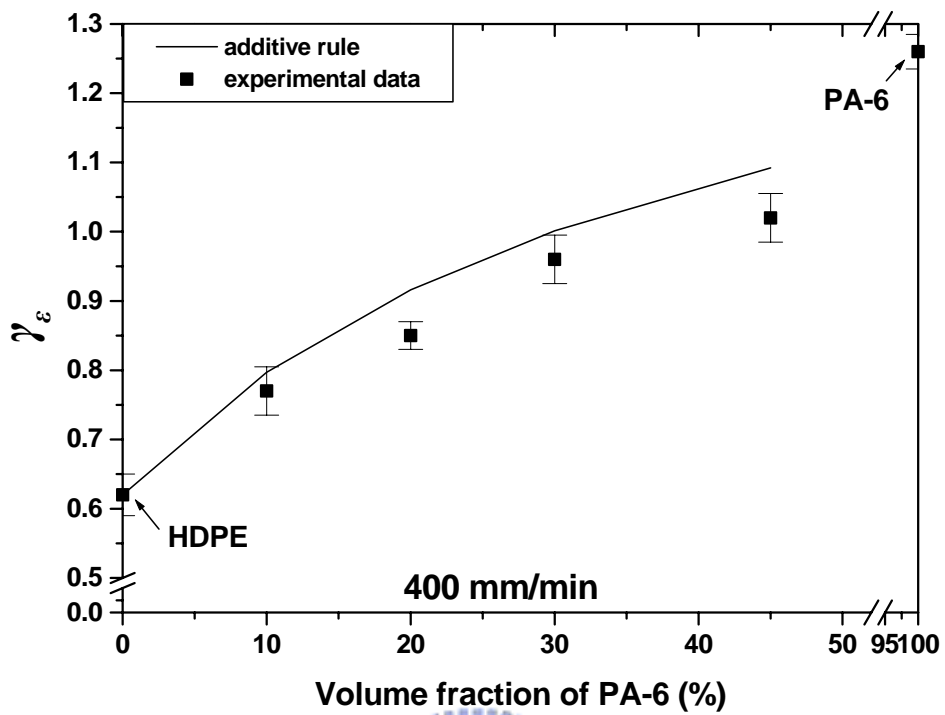
Figure 2-13(c) Comparison between the values of *m* of the three-layer films, having

various volume fractions of PA-6, determined using the additive rule and that from the

experimental data at crosshead speeds 400 mm/min.
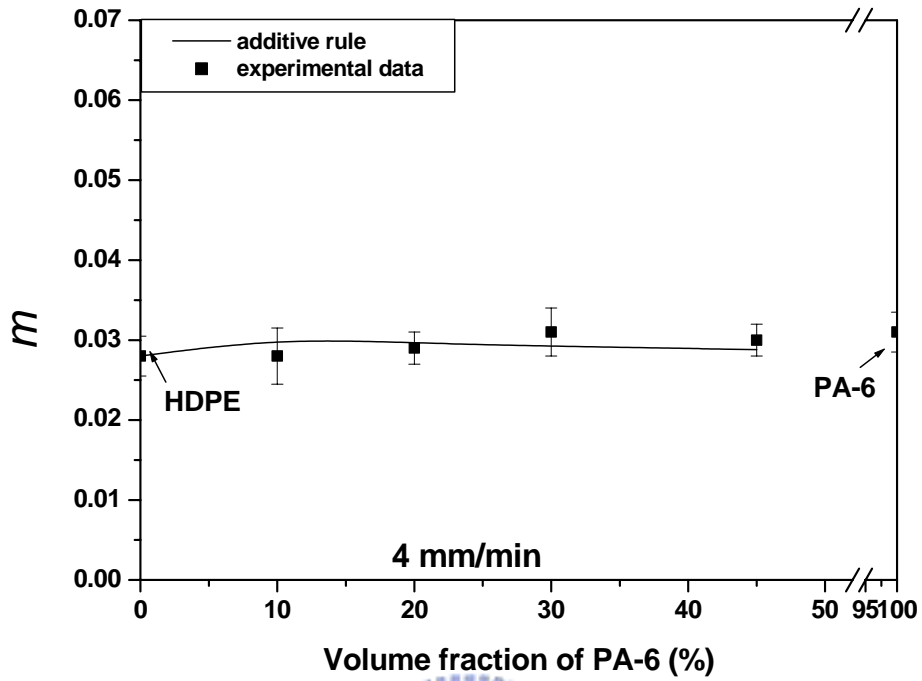
Figure 2-14(a) Comparison between the values of *m* of the three-layer films, having various volume fractions of PA-6, determined using the additive rule and that from the experimental data at crosshead speeds of 4 mm/min.
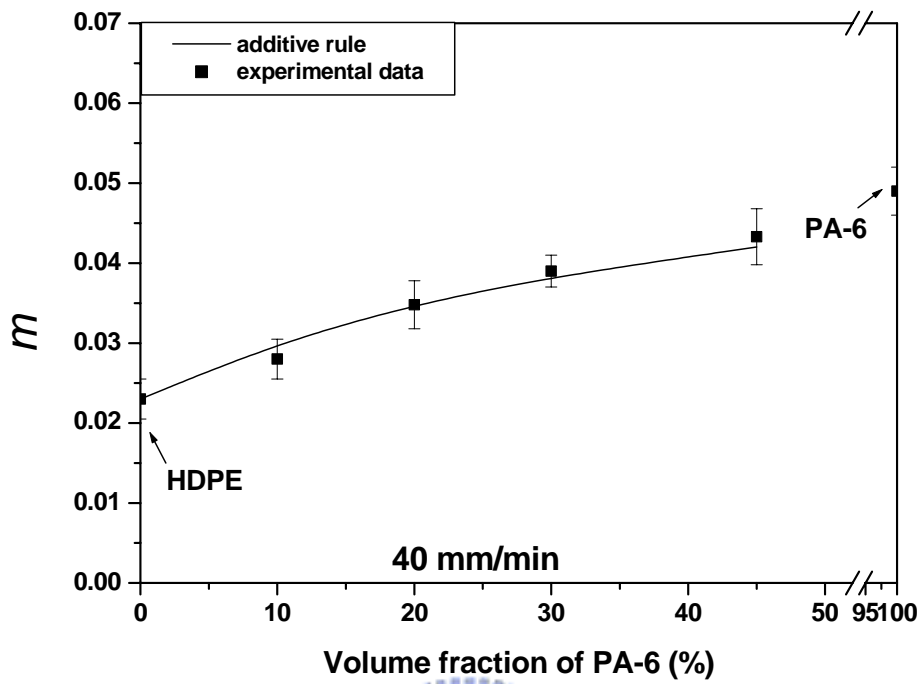
Figure 2-14(b) Comparison between the values of *m* of the three-layer films, having

various volume fractions of PA-6, determined using the additive rule and that from the

experimental data at crosshead speeds of 40 mm/min.
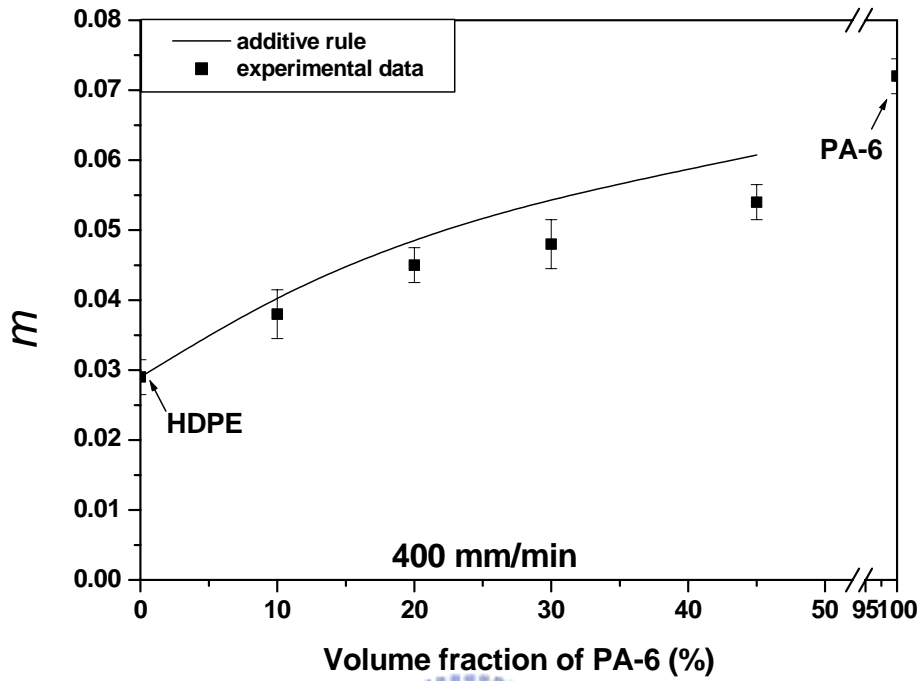
Figure 2-14(c) Comparison between the values of *m* of the three-layer films, having various volume fractions of PA-6, determined using the additive rule and that from the experimental data at crosshead speeds of 400 mm/min.

Chapter 3

Predicting the Permeability and Tensile Behavior of HDPE/tie/PA-6 Three-layer Films

3.1 Introduction

It is more common to introduce multilayer structure comprising different polymers to form a product with multiple properties. Each property takes the advantages of the best property of each individual component. Normally, a multilayer extruded product can be produced by a coextrusion into the types of multilayer sheets, blown films, cast films, tubing, and containers [1–5].

Polyethylene (PE) and polyamide 6 (PA-6) are two important classes of polymers used in coextrusion that are very popular in the packaging industry. PE is employed widely because of its low price, easy processibility, chemical inertness and high barrier properties toward moisture, but its poor barrier property toward oxygen, aromas and organic solvents limits its applicability [6-9]. On the other hand, PA is a good barrier resin toward oxygen, aromas, and organic solvents and it has high tensile strength and toughness, but is relatively expensive and a poor barrier for water vapor [10-13]. In packaging application, it is reasonable to combine these two resins into a single structure by using a coextrusion process to form multilayer films with multiple properties. However, an extrudable adhesive is often incorporated into the multilayer structure as tie layer in the coextrusion process due to the incompatibility between these two polymers. Kamykowski [14] studied the adhesive properties of five-layer,

polypropylene/ adhesive/ polyamide/ adhesive/ polypropylene, coextruded cast films and found that adhesion can be generally improved upon increasing the overall film thickness or the relative amount of the adhesive. Homopolymer diluents in the adhesive layer have better adhesion property than random copolymers. The molecular weight of the grafted polymer of adhesive has a small effect on adhesion. By combining graft and polymer blending, Tanaka et al. [15] have successfully developed a new generation of tie layer adhesives that maintain high adhesive strengths after thermoforming and orientation. Blend of component material and adhesive as both the adhesion promoting layer and support layer was used to eliminate the tie layer and provide adhesion between the chemical dissimilar layers [16-18], e.g. the five-layer film coextrusion system was replaced with a three-layer film comprising EVOH as the central layer and LDPE/LDPE-g-MAH blends as the external layers to form a three-layer structure, A/B/A (blend/EVOH/blend) [18].

In packaging application, the permeability and tensile strength are the two most important properties. These two properties of the monolayer with single material regarding to HDPE and PA-6 were reported in previous literatures [13,19-23]. With the goal of constructing a method for effectively predicting the specific properties of a multilayer structure from the properties of its individual component materials. In this paper we use a three-layer film, HDPE/tie/PA-6, to examine the permeabilities of nitrogen (N_2), oxygen (O_2), carbon dioxide (CO_2), and water vapor and tensile properties of three-layer films fabricated via a coextruded blown-film process using a series model [24] and an additive rule [25] as predicting methods, respectively. The aim of the study is to provide an economical and efficient tool for designing the compositions of the multilayer sheets, films and containers to achieve the desired properties by coextrusion process.

3.2 Experimental

3.2.1 Materials

The materials used in the coextrusion blown-film process were: (1) high-density polyethylene (HDPE); (2) polyamide-6 (PA-6); (3) adhesive, high-density polyethylene-grafted maleic anhydride (HDPE-g-MAH). HDPE was supplied in pellet form by Formosa Plastic Corp. (Taiwan), HDPE 9001. The melt index (M.I.) is 0.05 g/10min (190 °C, 2.16 kg); the density is 0.95 g/cm. The PA-6 was provided in pellet form by Mitsubishi Engineering Plastic Co. (Japan), Novamid 1030. The M.I. is 5 g/10min (240 °C, 2.16 kg); the density is 1.14 g/cm^3. The adhesive was obtained in pellet form from Mitsubishi Chemical Corp. (Japan), Modic-AP H503. The M.I. is 1.5 g/10min (190 °C, 2.16 kg); the density is 0.93 g/cm.

3.2.2 Preparation of Multilayer Films

Because of the hydrophilic property of PA-6, the polymer was dried in a vacuum oven for 12 hours at 90 °C before processing. HDPE, PA-6, and HDPE-g-MAH were fed separately into their individual extruders and coextruded through a three-layer coextrusion blown-film die (inner diameter = 97.6 mm; gap thickness = 1.2 mm) at 250 °C. The three-layer film was inflated and cooled with air and stretched by a take-up device after leaving the exit of the die. Monolayers of PA-6 and HDPE films were also prepared using the same blown-film equipment. All samples were placed in cabinet for 14 days maintained at 25 °C. Four different compositions of the component layers were prepared and the overall thickness of three-layer multilayered films was ca. 140 μm. Table 3-1 presents the thicknesses and volume fractions of the PA-6 layers; the compositions of all the three-layer films were controlled by using gear pumps precisely and steadily and the individual thicknesses of the component

layers were measured by using ultrasonic thickness measurement (Quinsonic, ElektroPhysik). Because the tie layer generally was very thin (ca. 5 μm in this study) in the coextrusion process, and the main molecular structure was HDPE, we consider the tie layer to be part of the HDPE layer and neglect its effect on permeability and tensile behavior in this study.

3.2.3 Permeability Measurement

The gas permeability, including that toward nitrogen (N_2), oxygen (O_2), and carbon dioxide (CO_2), was measured using a Lyssy L-100-5000 Gas Permeability Tester [26], following the ASTM Standard Method D1434. The gas permeability of the samples was measured at 23 °C and a relative humidity of 0%. Water vapor permeability was measured using a Lyssy L-80-5000 Water Vapor Permeability Tester [27], following the ASTM Standard Method E96. The permeability of the samples was measured at 38 °C and a relative humidity of 90%. The temperatures of both measurements were controlled by a water bath. Measurements were taken on 5 replicate samples; average values are reported.

3.2.4 Tensile Behavior Measurement

The uniaxial tensile behaviors of test samples with dimension of 40 mm long and 20 mm wide were measured by using a Hung-Ta Instrument, Model 2102AP. Three crosshead speeds, 4, 40 and 400 mm/min, were employed to test samples at a temperature of 25 °C and a relative humidity of 50%. Engineering stress–strain curves were determined from load-displacement data based on the original geometry of test sample. Measurements were taken on 5 replicate samples.

We calculated the engineering stress and strain by employing the original geometry of the sample film, but the cross-sectional area of a film sample changed continuously

during actual deformation. So, the engineering stress and strain cannot represent the actual stress and strain at any instance during deformation. It is necessary and more instructive to plot the true stress–strain curves to describe the tensile behavior. If the test sample deformed homogeneously, the constancy of volume was assumed during deformation and the true strain, ε_T, and the true stress, σ_T, were calculated by

$$\varepsilon_T = \ln(1 + \varepsilon_E) \tag{3.1}$$

$$\sigma_T = \sigma_E(1 + \varepsilon_E) \tag{3.2}$$

where ε_E and σ_E are the engineering strain and the engineering stress, respectively [19,28]. On the other hand, if the deformation was inhomogeneous, i.e., a neck formed, the surface of each sample film was marked with a set of 199 points, which were positioned 0.2mm apart along the 40mm gauge length of the specimen before testing [31]. The evolution of the specimen profile during a test was recorded continuously during the measurement with the aid of a CCD video camera, which was connected to a computer and coupled with a microscope mounted on a screw-driven device. The true stress and strain were determined by measuring the local deformation in the neck region from photographs obtained by a frame grabber during the experiment. Assuming that the sample kept constant volume during deformation, the true stress and true strain were calculated by

$$\varepsilon_T = \ln(1 + \varepsilon_L) \tag{3.3}$$

$$\sigma_T = \sigma_E(1 + \varepsilon_L) \tag{3.4}$$

where ε_L is the longitudinal strain of the displacement between two markers in the neck region. These markers were monitored along the central axis and the cross-section of sample was rectangular so that the effect of triaxiality during necking

could be ignored [31, 32].

3.3 Results and Discussion

3.3.1 Permeability

Table 3-2 lists the gas permeabilities, including N_2, O_2, and CO_2, of PA-6 and HDPE films. We obviously see that the PA-6 film performs much better barrier properties than HDPE toward all these gases, with permeabilities for both films increasing in the order $CO_2 > N_2 > O_2$. Table 3-2 also displays the gas permeabilities of three-layer films with various volume fraction of the PA-6 layer. The values of gas permeabilities of these three-layer films all lie between those of the individual component layers for all the gases. As expected, the permeability toward all gases decreased upon increasing the volume fraction of the PA-6 layer. In order to predict the gas permeability of a three-layer film from that of its individual component layers, we empolyed a series model [24] due to the lamellar structure of these films.

$$\frac{1}{P_M} = \frac{\alpha_{HDPE}}{P_{HDPE}} + \frac{\alpha_{PA-6}}{P_{PA-6}} \tag{3.5}$$

where P_M is the permeability of the three-layer film, P_{HDPE} and P_{PA-6} are the permeabilities of the monolayer films of HDPE and PA-6, respectively, and α_{HDPE} and α_{HPA-6} are the volume fractions of HDPE (including the tie layer) and PA-6 in the three-layer film, respectively. The gas permeabilities of three-layer films toward N_2, O_2, and CO_2 are presented in Figures 3-1~3-3, respectively, for both the series model and the experimental data. There exists a good agreement between the model's predictions and the experimental data for all these gases.

Table 3-3 lists the water vapor permeabilities of HDPE and PA-6films. In contrast to their gas permeabilities, we see that the HDPE film has a much better water vapor

barrier property than that of PA-6. Table 3-3 also presents the water vapor permeabilities of the three-layer films as a function of the volume fraction of the PA-6 layer. Similarly to the gas permeabilities, the values of water vapor permeabilities all lie between those of the individual component layers. Figure 3-4 displays the water vapor permeabilities of the three-layer films as a function of the volume fraction of the PA-6 layer. For the sake of comparison, this figure also presents the predictions obtained by the model using Equation (3.5). The water vapor permeabilities increase upon increasing the PA-6 content and agree reasonably well with the series model..

3.3.2 Tensile Behavior

The engineering stress–strain curves for the monolayer films of HDPE and PA-6 were showed in Figure 3-5. We see that the HDPE film deforms inhomogeneously at these three crosshead speeds, 4, 40 and 400 mm/min. A significant load drop can be seen to occur which is associated with stable neck formation at the central cross-section. The load drop is followed by the cold drawing, which is associated with neck propagation along the specimen. The true stress-strain curve was determined by measuring the local strain during neck region and applying Equations (3.3) and (3.4). On the other hand, the PA-6 film shows the obviously different tensile behavior compared to HDPE films. The PA-6 film exhibits a higher level of engineering stress and deforms homogeneously at low level of crosshead speeds, i.e. 4 and 40 mm/min. At higher level of strain, the engineering stress increases rapidly with the increase of engineering strain due to the molecular alignment [33]; this effect is known as strain hardening. The true stress-strain curve was calculated using Equation (3.1) and (3.2). However, at high level of crosshead speed, i.e. 400 mm/min, the deformation mode changes from homogeneous to inhomogeneous and the true stress-strain curve was determined as HDPE. Figure 3-6 displays the true stress–strain curves of the PA-6 and

HDPE films.

To model the deformation behavior of film, we employed the following empirical constitutive equation [19,29]:

$$\sigma_T = \sigma_0 \exp(\gamma \cdot \varepsilon_T) \tag{3.6}$$

where σ_0 and γ are the true yield stress and the strain hardening parameter, respectively. The constitutive equation can also be presented in the following form:

$$\ln \sigma_T = \ln \sigma_0 + \gamma \cdot \varepsilon_T \tag{3.7}$$

From Equation (3.7), the relationship of the natural logarithm of true stress ($\ln\sigma$) and true strain (ε_T) should be linear in the region of plastic deformation. By treating the least-squares approximation to the plot of the $\ln\sigma$ versus ε_T, the slope and intercept correspond to the strain hardening parameter (γ) and the natural logarithm of the true yield stress ($\ln\sigma_0$), respectively. Figure 3-7 displays the fitted curves and experimental data of the $\ln\sigma$ versus ε_T for the HDPE and PA-6 films. A linear relationship for both films appears to exist over the range of true strains from 0.25 to 1.40 with the correlation coefficients all > 0.99 with respect to the approximation. The corresponding parameters of the constitutive equation for the HDPE and PA-6 films at various crosshead speeds are summarized in Table 3-4. For comparison, Figure 3-8 displays both the experimental true stress–strain data and the modeling curves. We could see that a good agreement exists between the modeling curves and experimental data for the range of plastic deformation of the HDPE and PA-6 films.

Figure 3-9 presents a plot of the engineering and true stress–strain curves of three-layer films with various volume fractions of PA-6 at crosshead speed of 40 mm/min. It is clear that these curves all lie between those obtained for monolayers of HDPE and PA-6 films. The stress level increases upon increasing the volume fraction

of the PA-6 layer and, in addition, the strain hardening behavior due to the molecular alignment becomes more obvious. In the range of volume fractions of PA-6 that we investigated, all the three-layer films deform inhomogeneously at the crosshead speed. As shown in Figure 3-10, a linear relationship also appears to exist for the three-layer films over the same range of true strains (0.25–1.40) as it did for the HDPE and PA-6 films at crosshead speed 40 mm/min. The correlation coefficients are also all > 0.99 with respect to the approximation. The corresponding parameters of the constitutive equation for the three-layer films at various crosshead speeds are also presented in Table 3-4. A comparison of the modeling curves and experimental true stress–strain data at crosshead speed of 40 mm/min was shown in Figure 3-11. There also exists a good agreement between the experimental data and the modeling curves over the range of plastic deformation for the three-layer films with various volume fractions of PA-6.

Similar to what we reported above for predicting permeability, we introduced a simple theoretical additive rule model [25] to predict the tensile behavior of a three-layer film from those of its individual component layers:

$$\sigma_M = \alpha_{HDPE}\, \sigma_{HDPE} + \alpha_{PA-6}\sigma_{PA-6} \tag{3.8}$$

where σ_M is the true stress of a three-layer film, σ_{HDPE} and σ_{HPA-6} are the true stresses of the HDPE and PA-6 layers, respectively, and α_{HDPE} and α_{HPA-6} are the volume fractions of HDPE (including the tie layer) and PA-6 layers, respectively.

From Equations (3.6) and (3.8), the relationship between the true stress–strain of the three-layer and the individual component layer films is:

$$\sigma_{oM}\, \exp(\gamma_M \cdot \varepsilon_T) = \alpha_{PA-6}\sigma_{0PA-6}\, \exp(\gamma_{PA-6} \cdot \varepsilon_T)$$
$$+ \alpha_{HDPE}\, \sigma_{0HDPE}\, \exp(\gamma_{HDPE} \cdot \varepsilon_T) \tag{3.9}$$

where σ_{0M} is the true yield stress of the three-layer film, σ_{0HDPE} and σ_{0PA-6} are the true

yield stresses of the HDPE and PA-6 layers, respectively, and γ_M, γ_{HDPE} and γ_{PA-6}, are the strain hardening parameters of the three-layer film, HDPE, and PA-6 layers, respectively. It is reasonable to assume that the true yield stress of the three-layer film alone follows the additive rule:

$$\sigma_{0M} = \alpha_{PA-6}\sigma_{0PA-6} + \alpha_{HDPE}\,\sigma_{0HDPE} \qquad (3.10)$$

and the strain hardening parameter of the three-layer film is defined as [30]:

$$\begin{aligned}\gamma_M(\varepsilon) &= \frac{\partial \ln\sigma_M}{\partial\varepsilon} \\ &= \frac{\partial\left[\alpha_{PA-6}\sigma_{0PA-6}\exp(\gamma_{PA-6}\cdot\varepsilon) + \alpha_{HDPE}\sigma_{0HDPE}\exp(\gamma_{HDPE}\cdot\varepsilon)\right]}{\partial\varepsilon}\end{aligned} \qquad (2.11)$$

We calculated the parameters σ_{0M} and γ_M for the additive rule by using the parameters of the individual component layers in Table 3-4. Figure 3-12 presents the dependence of these parameters obtained by additive rule and the experimental data (from Table 3-4) with respect to the compositions of films. We can see that a good agreement exists between the experimental data and the additive-rule model for both strain hardening parameter and true yield stress at low level of crosshead speeds, which suggests that this rule can be used to accurately predict the plastic deformation of the three-layer films. But a larger discrepancy existed between the model and experimental data at high crosshead speed for both these parameters of the three-layer films at high level of crosshead speed. This is due to the generation of heat during deformation [34]. The heat would cause a decrease in the stress to produce a given strain, which resulted in the discrepancy between experimental data and additive rule.

3.4 Conclusions

In this study, we have successfully fabricated HDPE/tie/PA-6 three-layer films,

typical multilayer structure A/B/C, by a coextrusion blown-film process. We have investigated the three gases, including N_2, O_2, and CO_2, and water vapor permeabilities. We found that predicting both the gas and water vapor permeability of the three-layer films with respect to the volume fraction of PA-6 based upon those of the individual component layer films occurs in good agreement with the experimental data when using the series model. On the other hand, a constitutive equation was employed to describe the tensile behavior of the films over the range of plastic deformation. The tensile behavior of the component layer and multilayer films at various crosshead speeds can be precisely expressed by a constitutive equation having two parameters in the true stress–strain relationship, i.e., the true yield stress and the strain hardening parameter. We examined the relationships between the parameters of the monolayers of the component layers and those of the three-layer films by using an additive rule. By using the rule, we can also predict the tensile properties, including the true yield stress and strain hardening, of the three-layer film from those of the individual component layers with good agreements in the true stress–strain relationship. But there was a larger discrepancy between the model and experimental data at high crosshead speed due to the generation of heat during deformation.

In summary, we could design efficiently the compositions of the multilayer structure to achieve specific permeability and/or tensile property by employing these model predictions before processing.

3.5 References

1. J. Culter, J. Krohn and W. Todd, *Pack. Tech. Eng.*, **8**, 30 (1999).

2. J. Dooley, K. S. Hyun, and K. Hughes, *Polym. Eng. Sci.*, **38**, 1060 (1998).

3. W. J. Schrenk and S. A. Marcus, *J. Plast. Film Sheet.*, **1**, 30 (1985).

4. S. Hosoda, Y. Seki and H. Kihara, *Polymer*, **34**, 4602 (1993).

5. S. J. Liu and C. H. Yang, *Adv. Polym. Tech.*, **20**, 108 (2001).

6. F. Hensen, Plastics Extrusion Technology, Hanser, New York,1997, Chap. 5.

7. I. I. Rubin, Handbook of Plastic Materials and Technology, Wiley, New York, 1990, Chap. 30.

8. M. B. Sabne, S. M. Thombre, A. S. Patil, S. D. Patil, S. B. Idage, and S. P. Vernekar, *J. Appl. Polym. Sci.*, **58**, 1275 (1995).

9. T. S. Gill and M. Xanthos, *Polym. Eng. Sci.*, **2**, 248 (1996).

10. D. C. Climenhage, *Packaging*, **32**, 39 (1987).

11. S. Eichler and J. Miltz, *J. Appl. Polym. Sci.*, **50**, 2095 (1993).

12. I. I. Rubin, Handbook of Plastic Materials and Technology, Wiley, New York, 1990, Chap. 16.

13. Y. P. Khanna, E. D. Day, M. L. Tsai and G. Vaidyanathan, *J. Plast. Film Sheet.*, **13**, 197 (1997).

14. G. W. Kamykowski, *J. Plast. Film Sheet.*, **16**, 237 (2000).

15. H. Tanaka, H. Shigemoto and H. Kawchi, *J. Plast. Film Sheet.*, **12**, 279 (1996).

16. S. S. Valdes, F. O. Villarreal, M. L. Quintanilla, I. Y. Flores, and L. F. Ramos de Valle, *Polym. Eng. Sci.*, **38**, 127 (1998).

17. J. V. Olmos, S. S. Valdes, and I. G. Yánez Flores, *Polym. Eng. Sci.*, **39**, 1597 (1999).

18. C. H. Huang, J. S. Wu, C. C. Huang, and L.S. Lin, *Polym. J.,* **35**, 978 (2003).

19. S.Bahadur, *Polym. Eng. Sci.*, **13**, 266 (1973).

20. Y. Wang, A. J. Easteal and X. D. Chen, *Pack. Tech. Sci.*, **11,** 169 (1998).

21. L. Lin and A. S. Argon, *J. Mater. Sci.*, **29**, 294 (1994).

22. S. Bianchi, S. Cantagallo, G. Consolati, M. Laporta, M. Pegoraro, G. Tieghi and L.

Zanderighi, *J. Appl. Polym. Sci.*, **86**, 559 (2002).

23. L. Lin and A. S. Argon, *J. Mater. Sci.*, **29**, 294 (1994).

24. J. B. Faisant, A. Aït-Kadi, M. Bousmina and L. Deschênes, *Polymer*, **39**, 533 (1998).

25. W. J. Schrenk and T. Alfrey, *Polym. Eng. Sci.*, **9**, 393 (1969).

26. Automatic Manometric Gas Permeability Tester Operator Manual, Model L100-5000, Lyssy AG, 2001.

27. Automatic Manometric Water Vapor Permeability Tester Operator Manual, Model L80-5000, Lyssy AG, 2001.

28. M. Al-Hussein and G. Strobl, *Macromolecules*, **35**, 8515 (2002).

29. V. Gaucher-Miri, G. K. Jones, R. Kaas, A. Hiltner and E. Baer, *J. Mater. Sci.*, **37**, 2635 (2002).

30. E. W. Hart, *Acta Metall.*, **15**, 351 (1967).

31. C. G'Sell, N. A. Aly-Helal and J. J. Jonas, *J. Mater. Sci.*, **18**, 1731 (1983).

32. Gĕrard Buisson and K. Ravi-Chandar, *Polymer*, **31**, 2071 (1990).

33. A. Peterlin, *J. Mater. Sci.*, **6**, 490 (1971).

34. I. H. Hall, *J. Appl. Polym. Sci.*, **12**, 739 (1968).

Table 3-1 Thickness and volume fraction of PA-6 layer in three-layer films

Thickness of PA-6 layer (μm)	Volume fraction of PA-6 layer (%)
14	10
28	20
42	30
63	45

Table 3-2 Gas Permeabilities of monolayer PA-6, monolayer HDPE and three-layer films.

Volume fraction of PA-6 (%)	Permeability (ml-mm/m^2-day-atm)		
	N_2	O_2	CO_2
0 (HDPE)	1.26	9.28	17.41
10	1.21	6.73	16.20
20	1.07	4.61	13.22
30	0.87	4.10	12.66
45	0.82	2.94	10.37
100 (PA-6)	0.55	1.73	7.50

Table 3-3 Water Vapor Permeabilities of monolayer PA-6, monolayer HDPE and three-layer films.

Volume fraction of PA-6 layer (%)	Permeability $\times\ 10^2$ (g-mm/m^2-day)
0 (HDPE)	2.71
10	2.82
20	3.53
30	4.00
45	5.01
100 (PA-6)	987.52

Table 3-4 True yield stress (σ_0) and strain hardening parameter (γ)of HDPE, PA-6 and three-layer films at various crosshead speeds.

| Volume fraction of | Crosshead Speed (mm/min) | | | | | |
| | 4 | | 40 | | 400 | |
PA-6 layer (%)	σ_0 (MPa)	γ	σ_0 (MPa)	γ	σ_0 (MPa)	γ
0 (HDPE)	21.54	0.80	23.57	0.78	26.20	0.75
10	22.20	0.87	25.79	0.86	27.66	0.78
20	24.78	0.91	27.66	0.89	30.88	0.81
30	25.66	0.97	30.88	0.92	34.47	0.84
45	29.67	1.02	33.78	0.97	38.09	0.86
100 (PA-6)	38.09	1.15	48.43	1.10	55.70	0.99
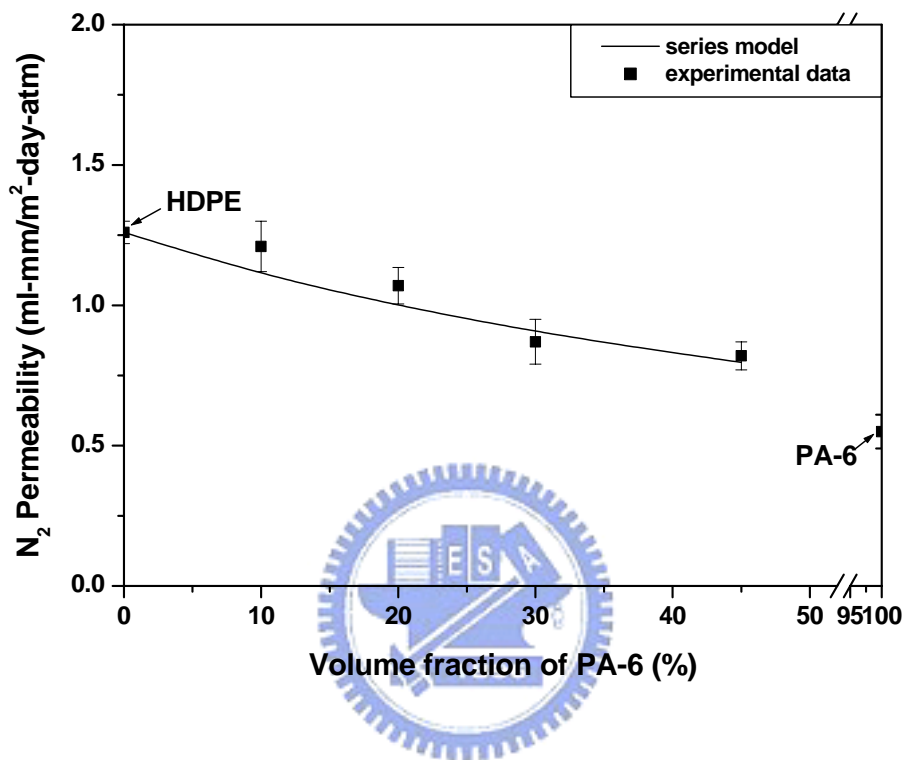
Figure 3-1 Nitrogen (N$_2$) permeabilities of three-layer films with various content of
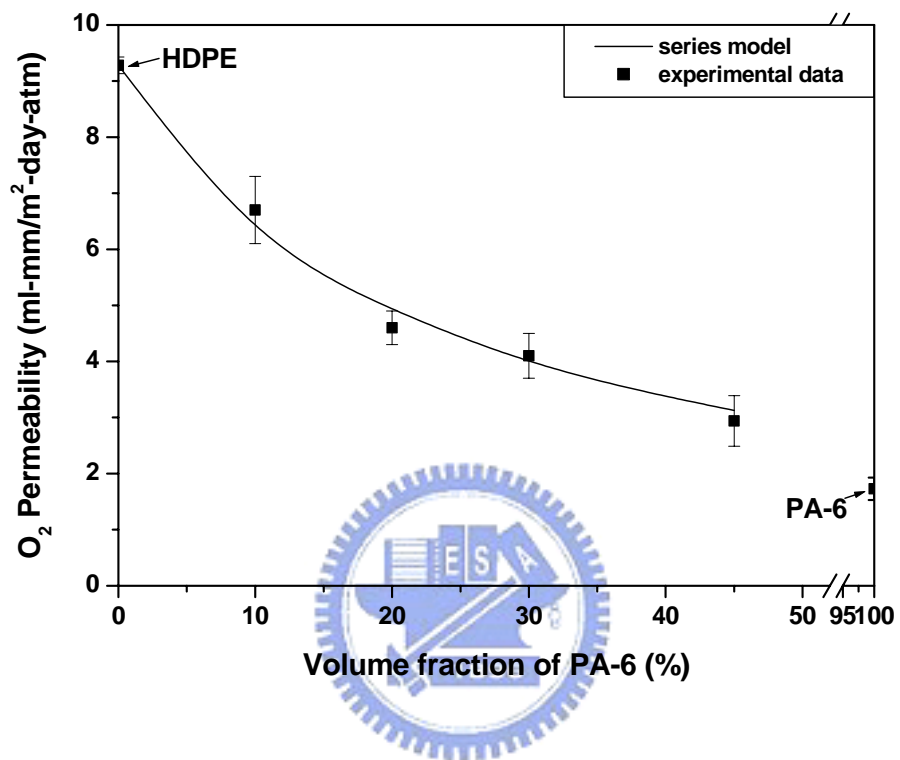
PA-6 layer.

Figure 3-2 Oxygen (O$_2$) permeabilities of three-layer films with various content of
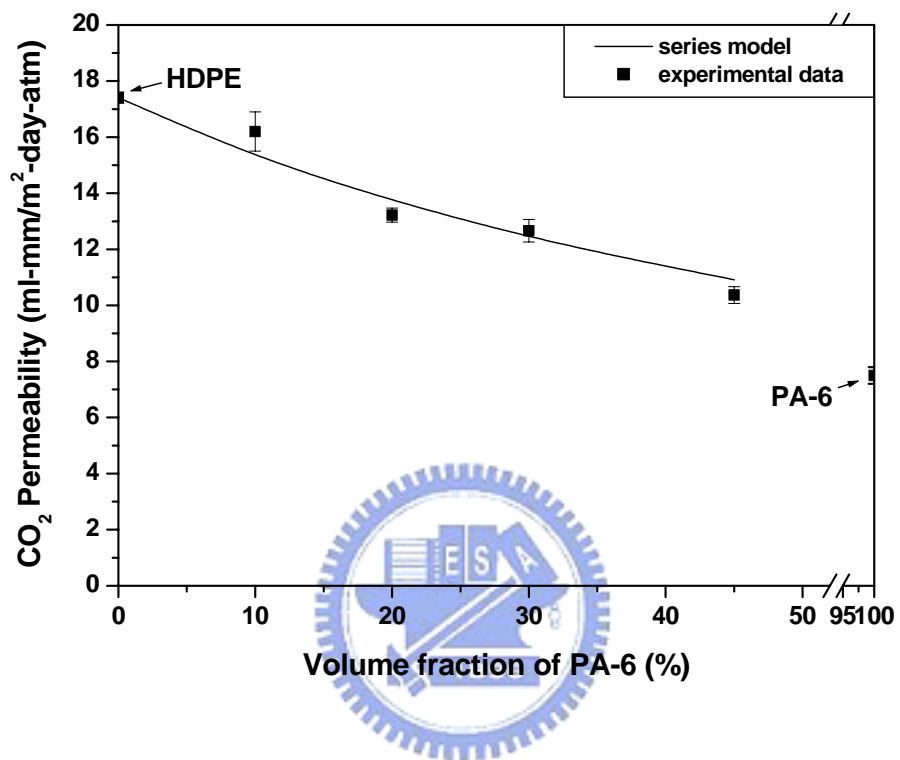
PA-6 layer.

Figure 3-3 Carbon dioxide (CO_2) permeabilities of three-layer films with various content of PA-6 layer.
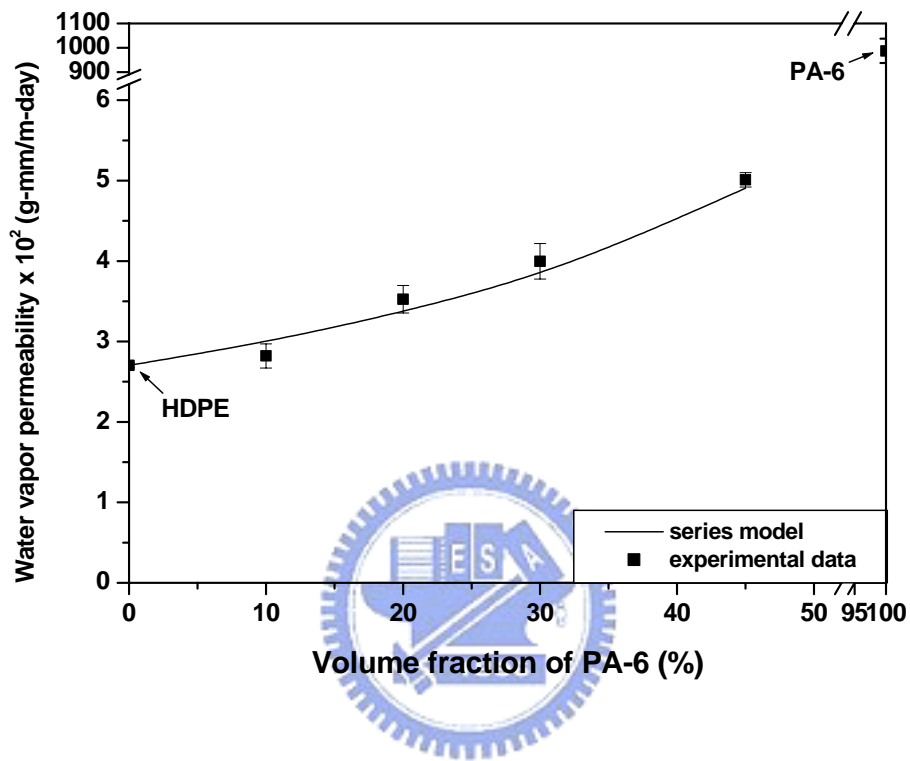
Figure 3-4 Water vapor permeabilities of three-layer films with various content of

PA-6 layer.
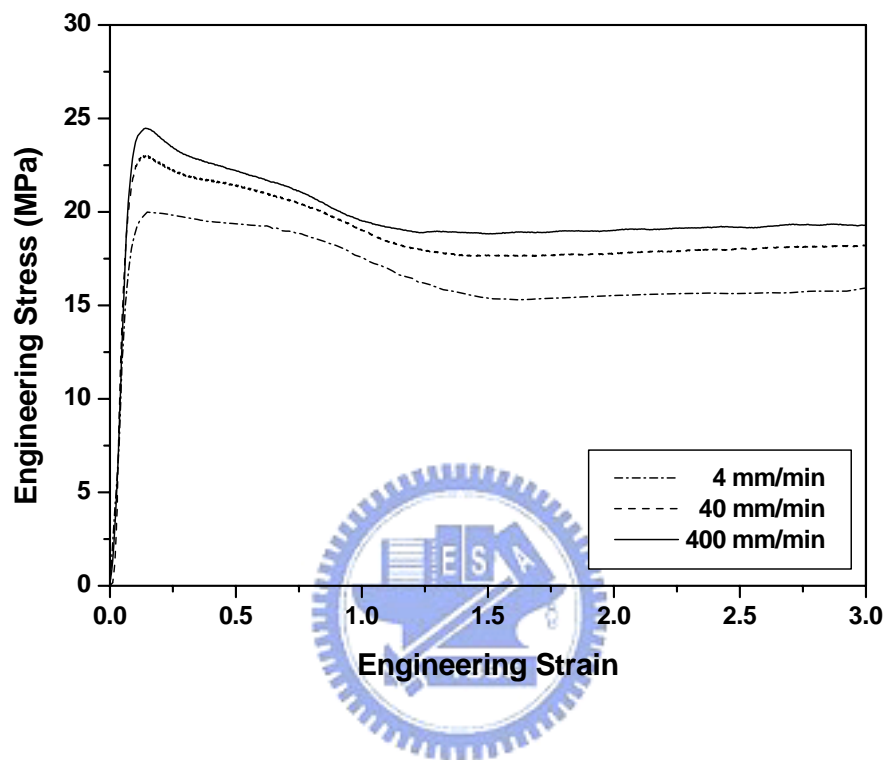
Figure 3-5(a) Engineering stress-strain curves of HDPE film at various crosshead
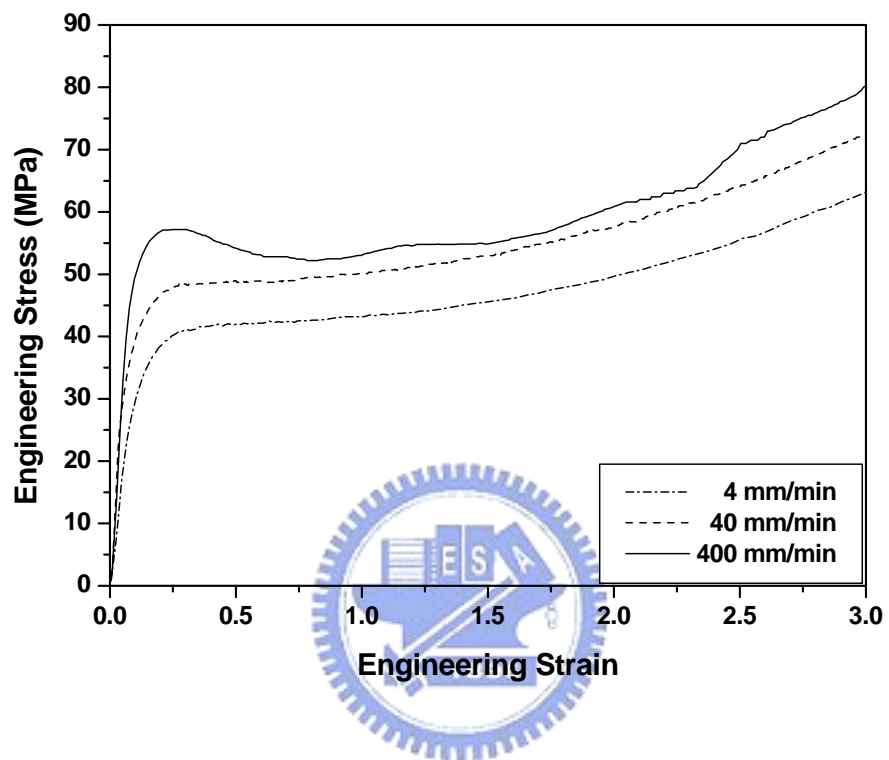
speeds.

Figure 3-5(b) Engineering stress-strain curves of PA-6 films at various crosshead speeds.
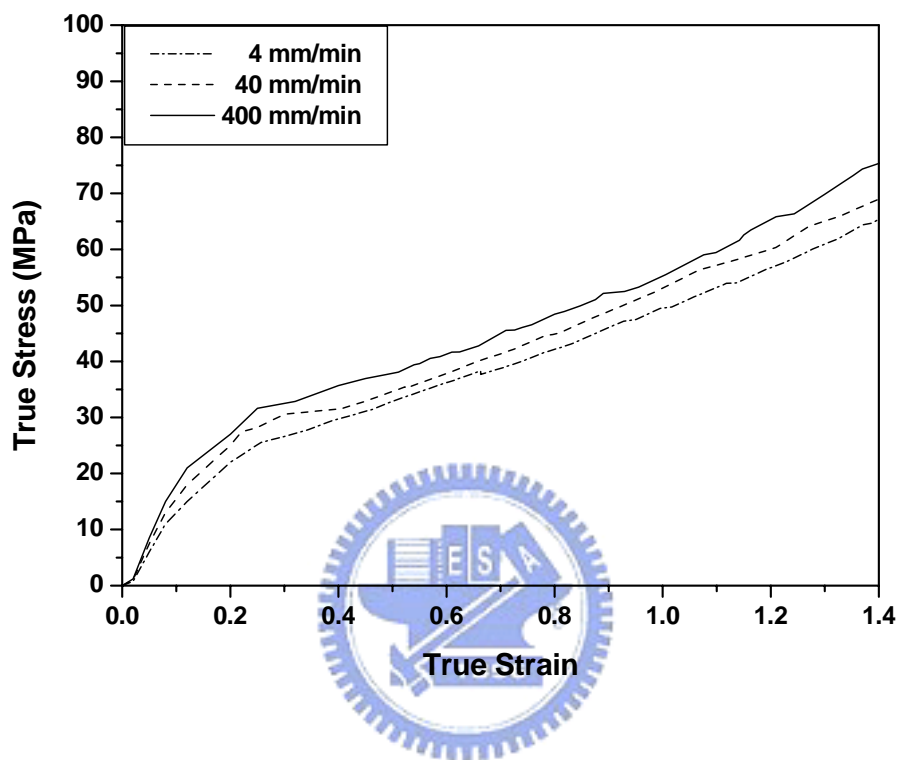
Figure 3-6(a) True stress-strain curves of HDPE films at various crosshead speeds.
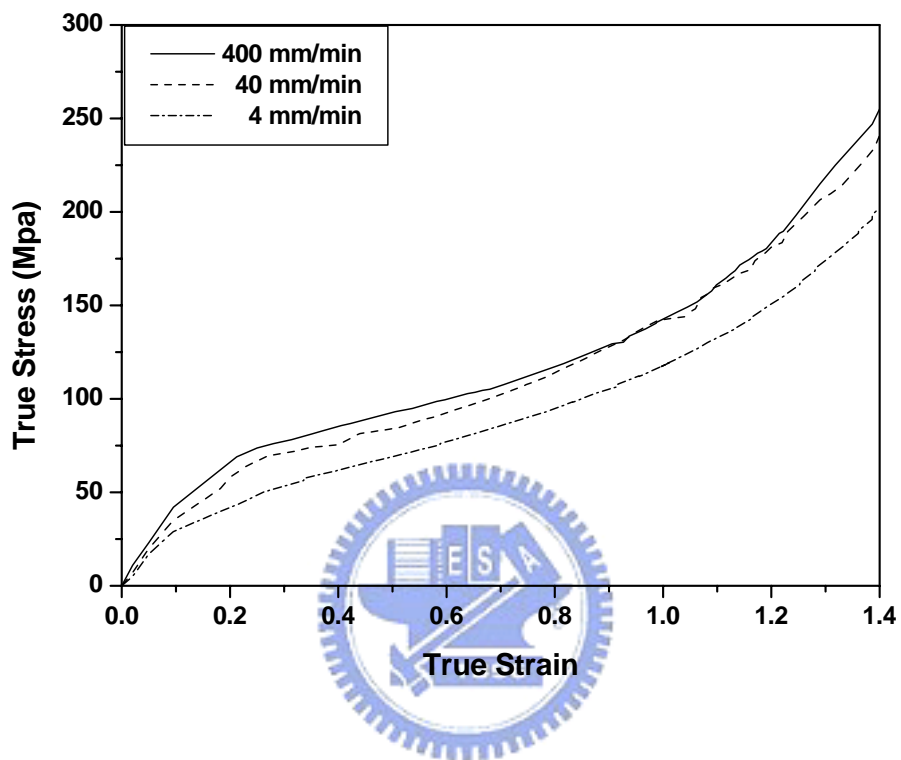
Figure 3-6(b) True stress-strain curves of PA-6 films at various crosshead speeds.
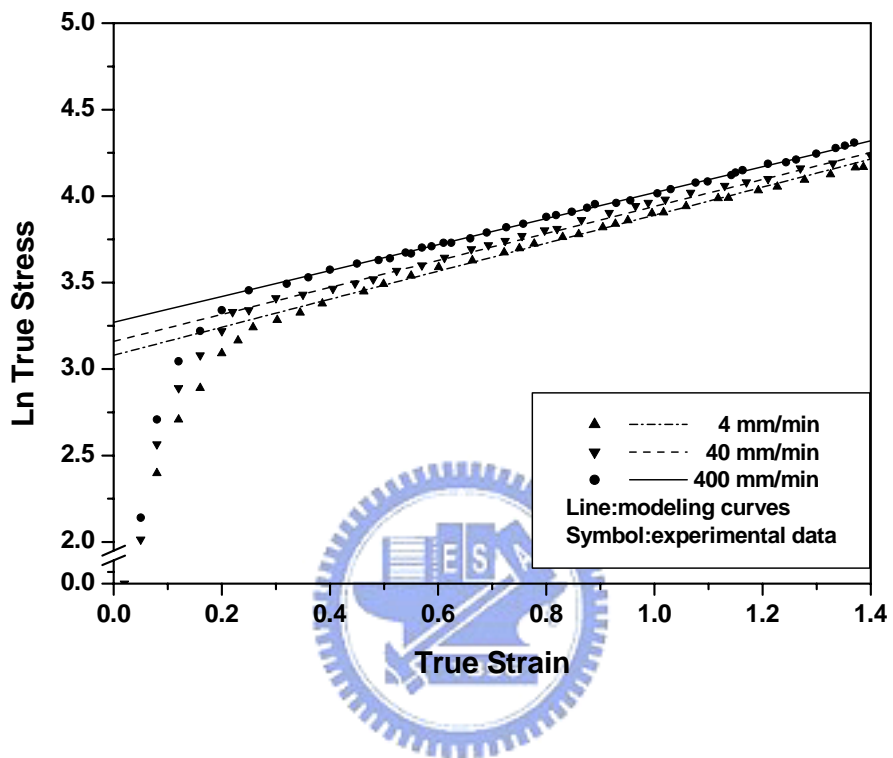
Figure 3-7(a) Modeling and experimental data of Ln true stress-strain of HDPE films

at various crosshead speeds.
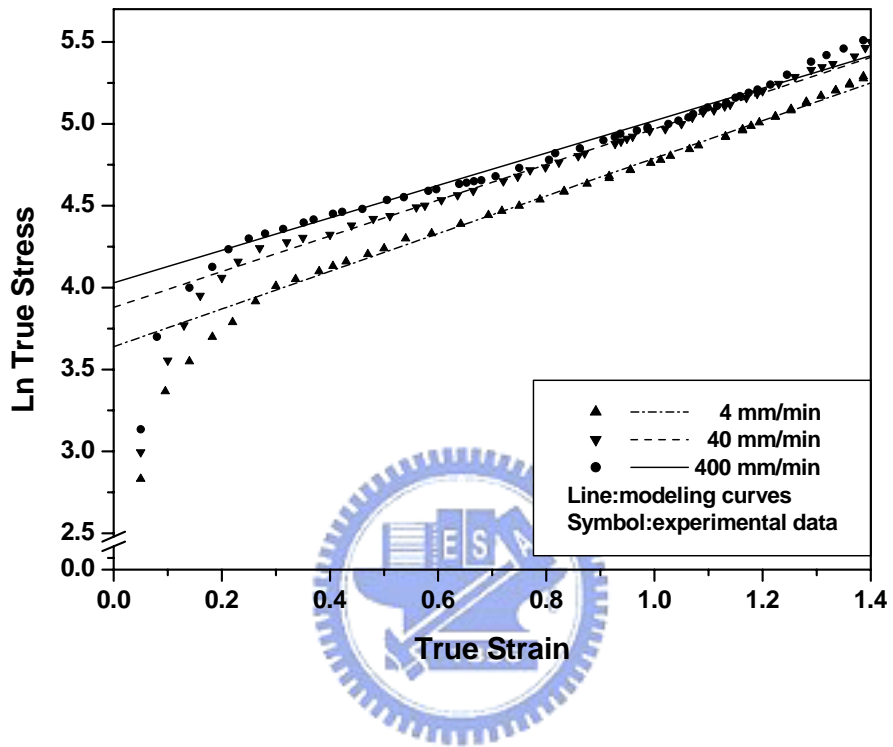
Figure 3-7(b) Modeling and experimental data of Ln true stress-strain of PA-6 films at various crosshead speeds.
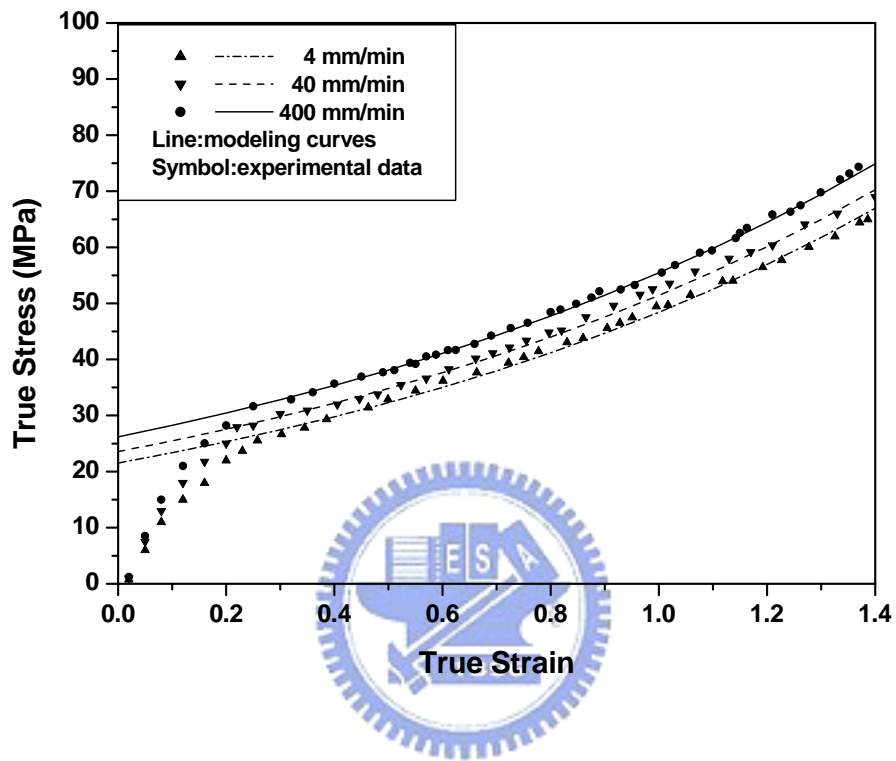
Figure 3-8(a) Comparison of true stress-strain curves between modeling curves and

experimental data of HDPE films at various crosshead speeds.
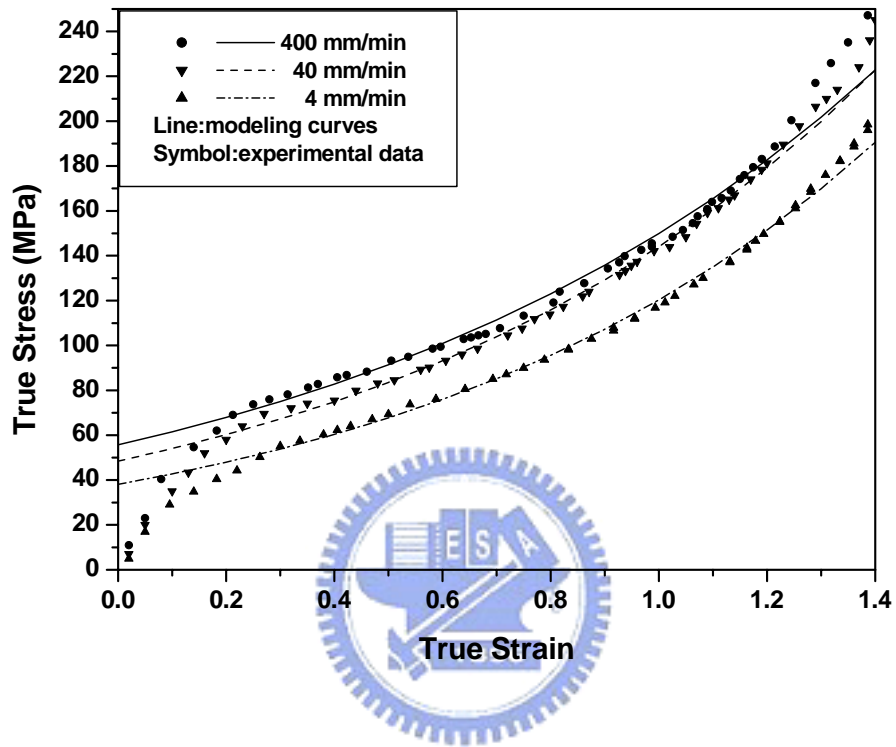
Figure 3-8(b) Comparison of true stress-strain curves between modeling curves and experimental data of PA-6 films at various crosshead speeds.
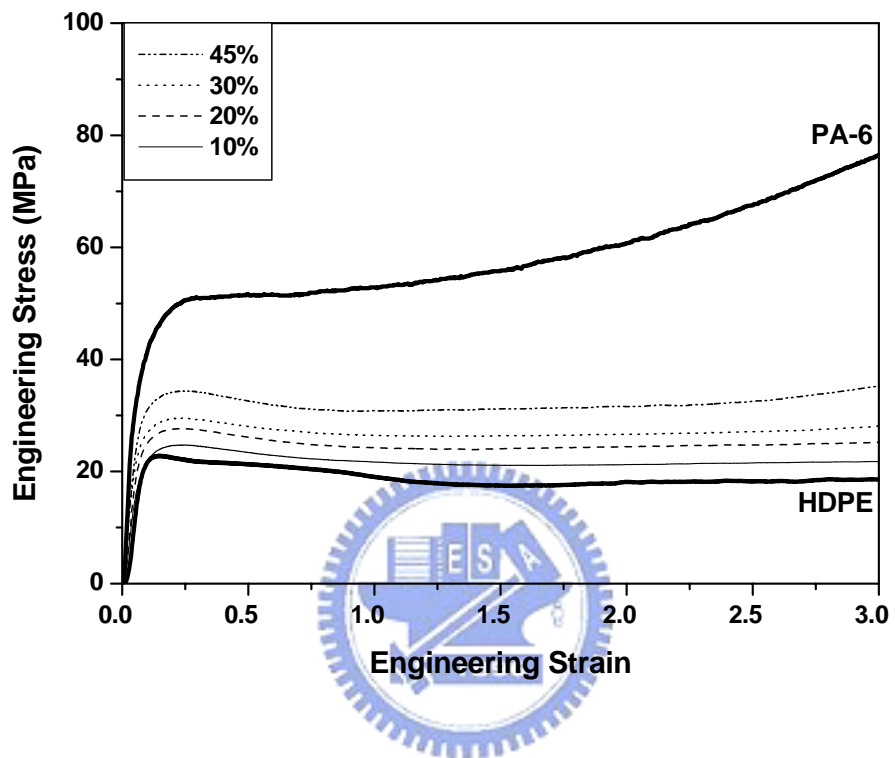
Figure 3-9(a) Engineering stress-strain curves of three-layer films as a function of

volume fraction of PA-6 layer at crosshead speed 40 mm/min. Thick solid lines

represent the component layer of PA-6 and HDPE, respectively.
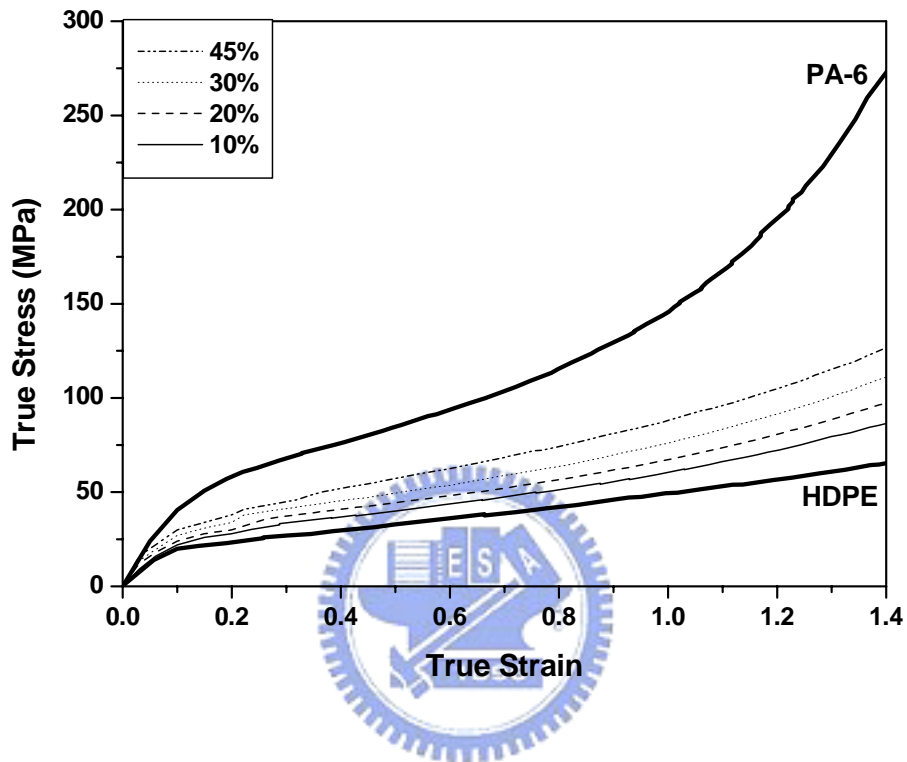
Figure 3-9(b) True stress-strain curves of three-layer films as a function of volume fraction of PA-6 layer at crosshead speed 40 mm/min. Thick solid lines represent the component layer of PA-6 and HDPE, respectively.
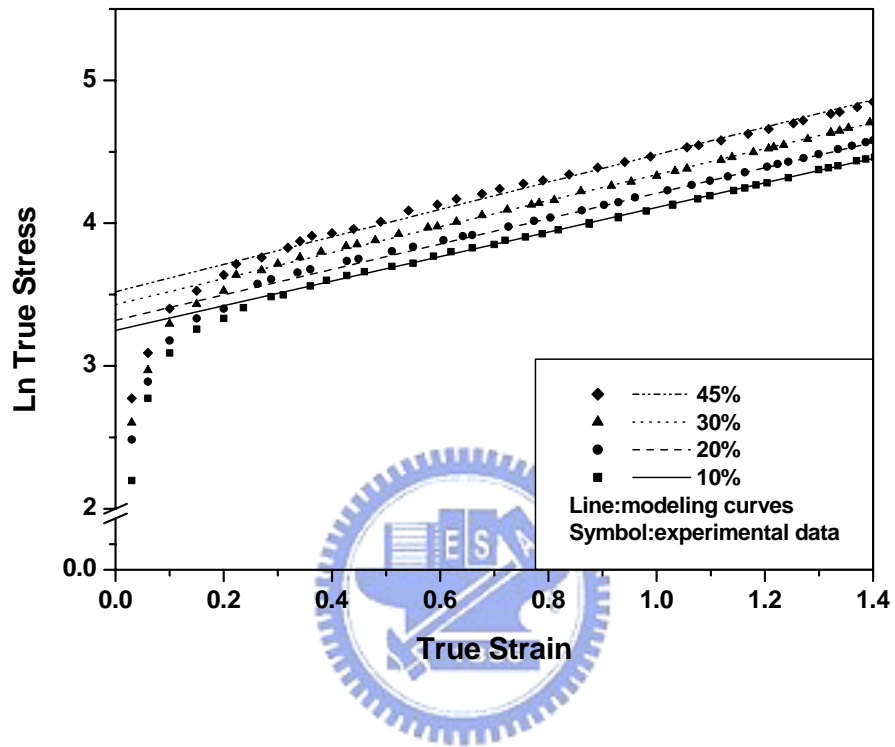
Figure 3-10 Modeling and experimental data of Ln true stress-strain of three-layer

films as a function of volume fraction of PA-6 layer at crosshead speed 40 mm/min.
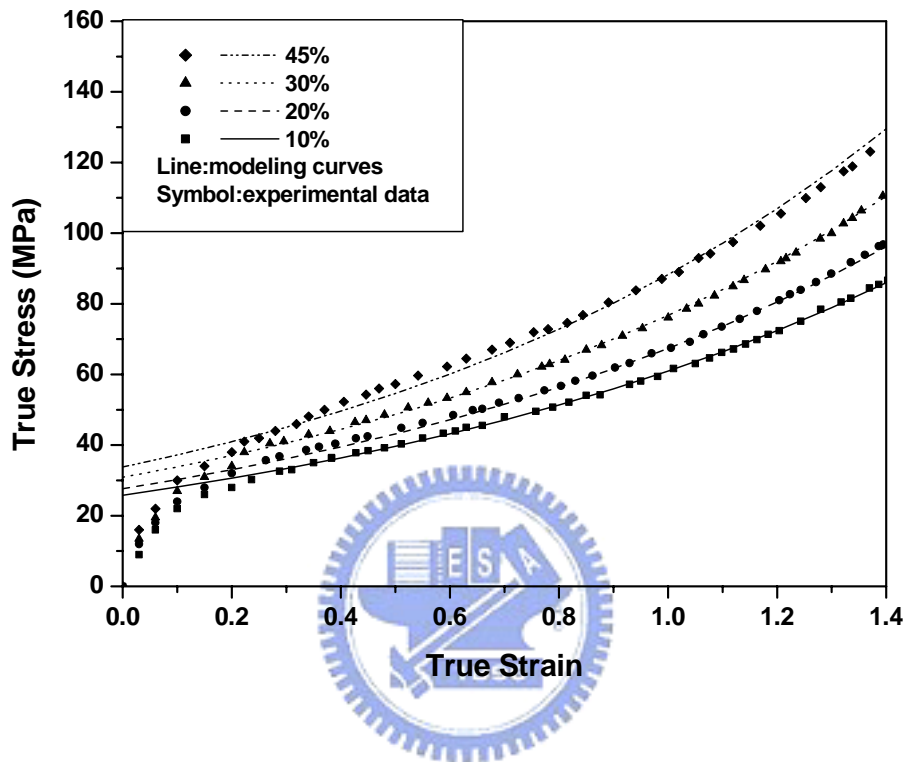
Figure 3-11 Comparison of true stress-strain curves between modeling curves and experimental data of three-layer films as a function of volume fraction of PA-6 layer at crosshead speed 40 mm/min.
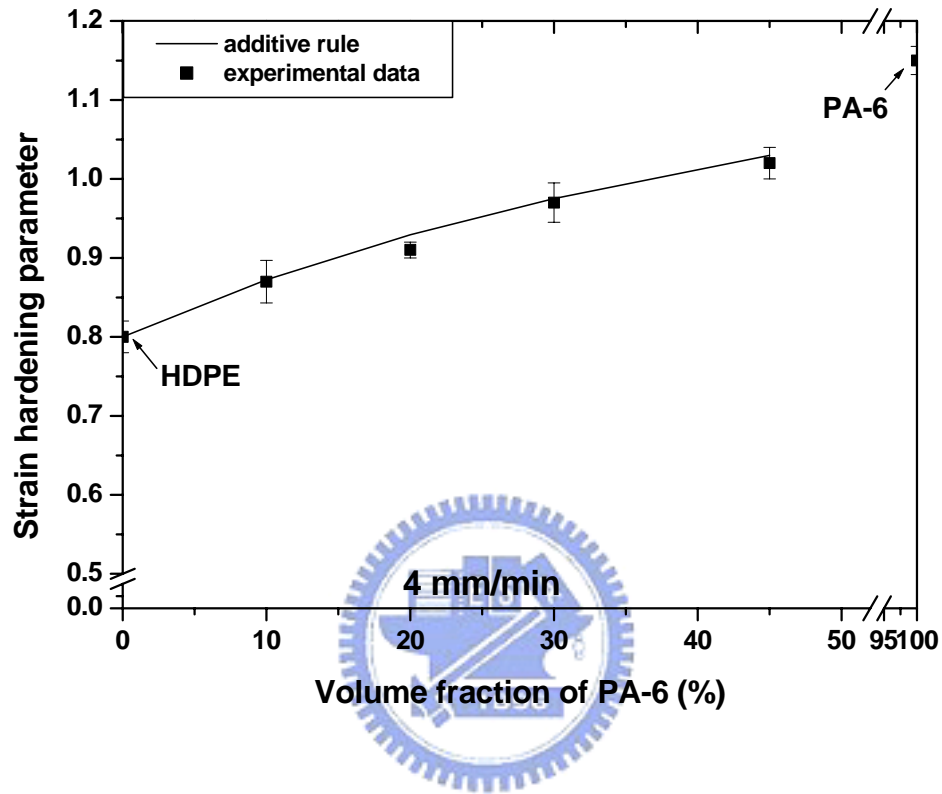
Figure 3-12(a) Comparison of strain hardening parameter between additive rule and experimental data as a function of PA-6 content at crosshead speed of 4 m/min.
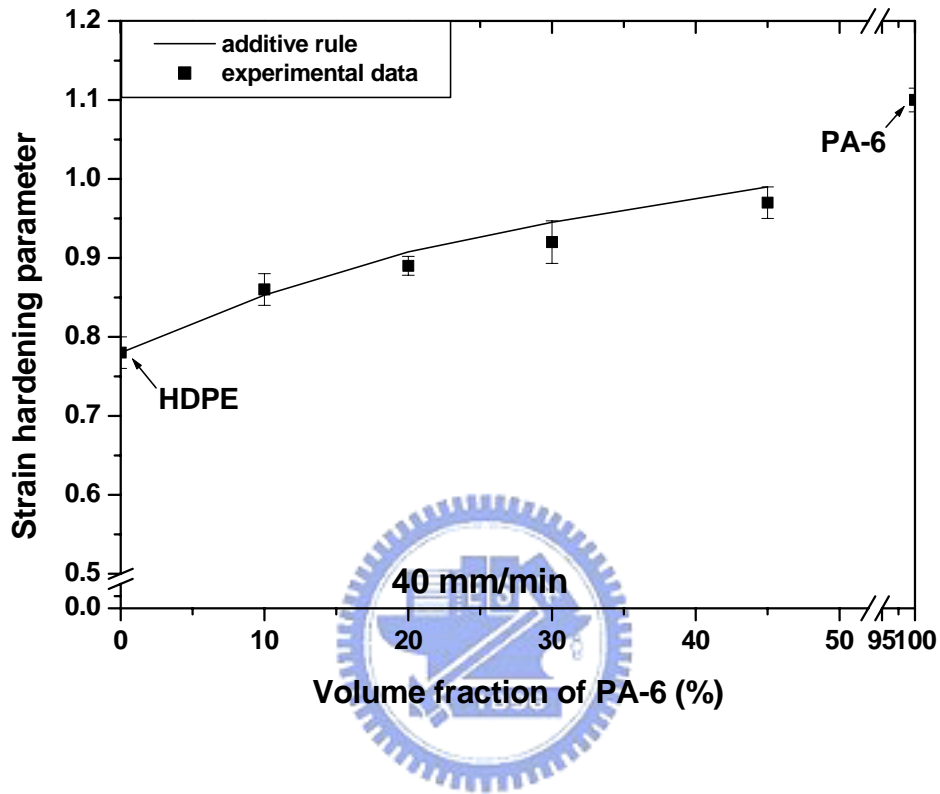
Figure 3-12(b) Comparison of strain hardening parameter between additive rule and experimental data as a function of PA-6 content at crosshead speed of 40 mm/min.
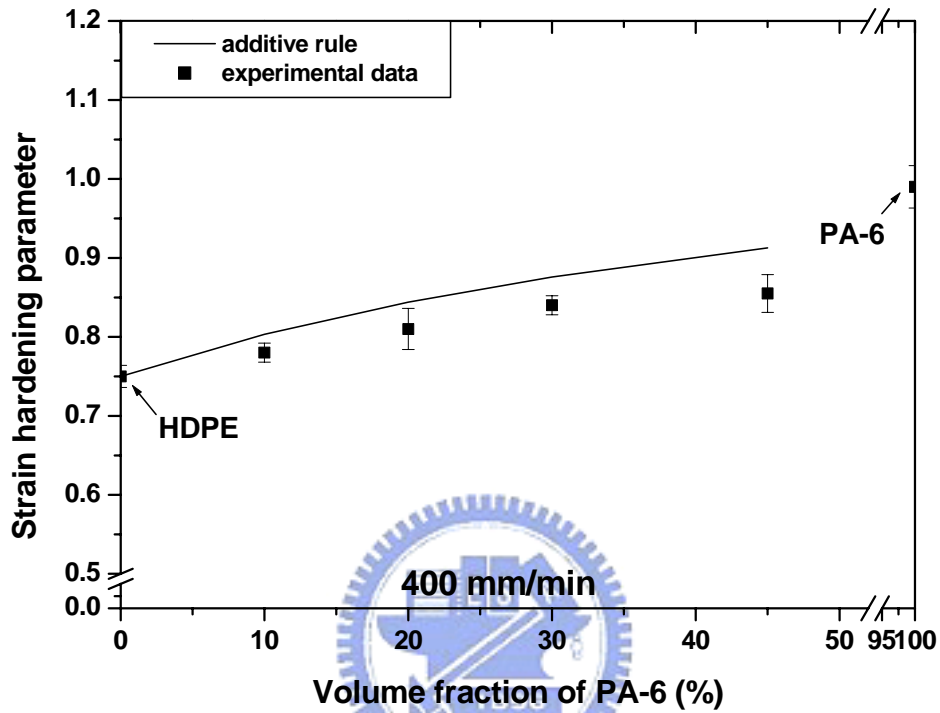
(c)

Figure 3-12(c) Comparison of strain hardening parameter between additive rule and experimental data as a function of PA-6 content at crosshead speed of 400 mm/min.
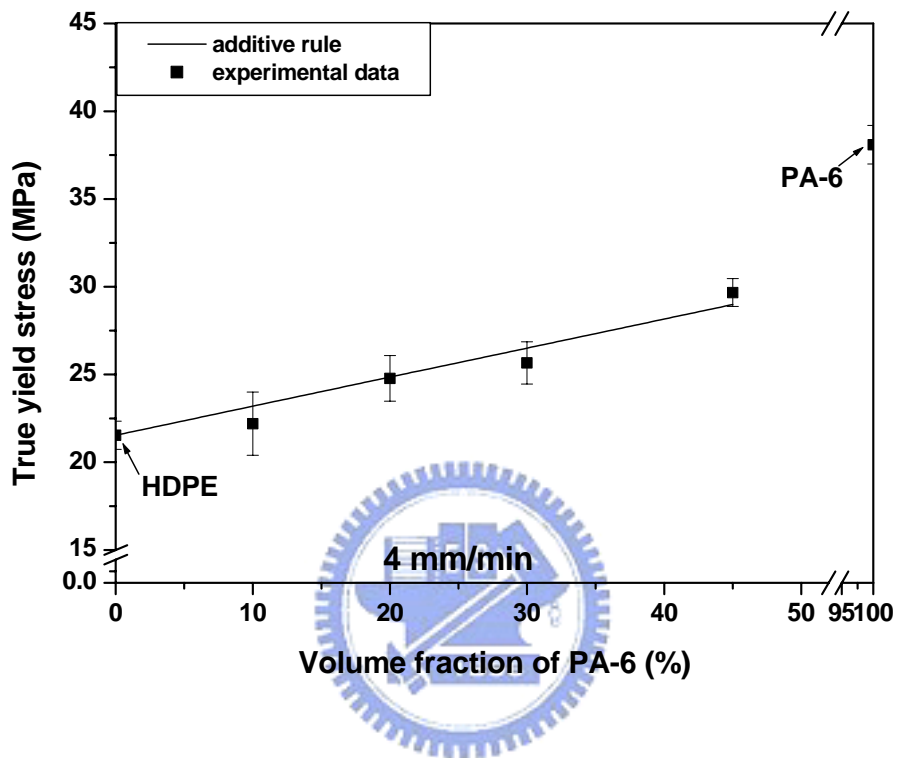
Figure 3-13(a) Comparison of true yield stress between additive rule and experimental

data as a function of PA-6 content at crosshead speed of 4 mm/min.
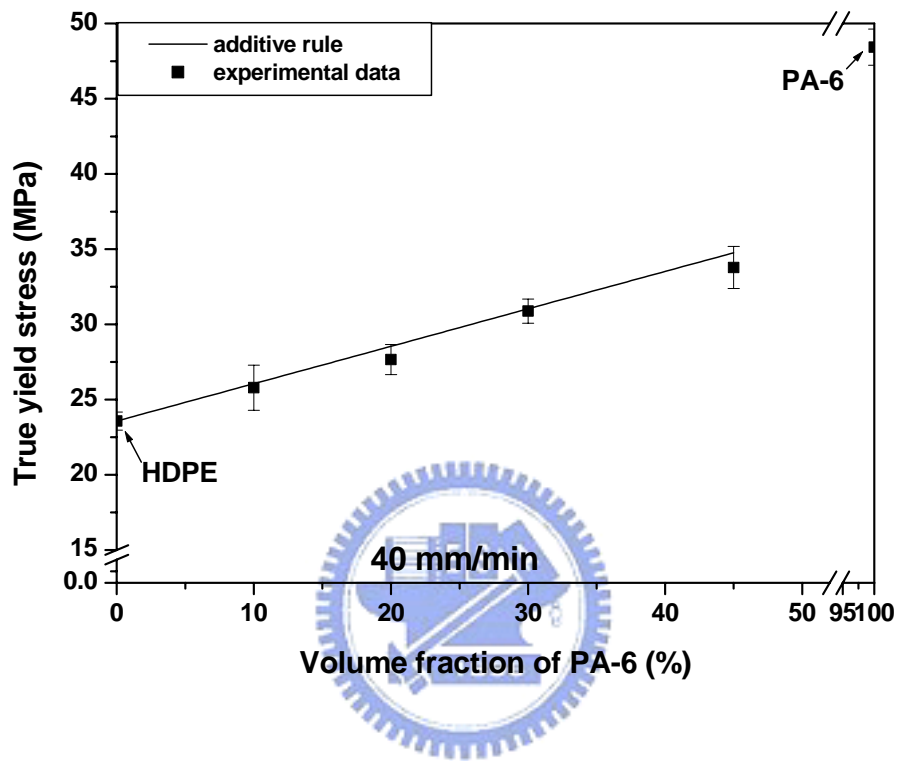
Figure 3-13(b) Comparison of true yield stress between additive rule and

experimental data as a function of PA-6 content at crosshead speed of 40 mm/min.
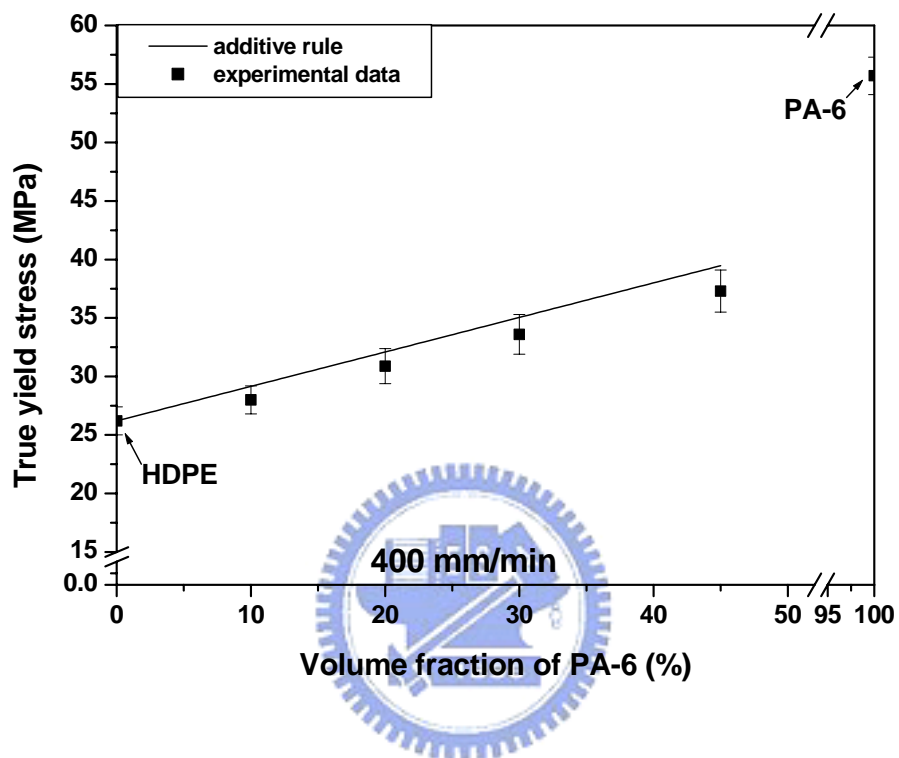
Figure 3-13(c) Comparison of true yield stress between additive rule and experimental

data as a function of PA-6 content at crosshead speed of 400 mm/min.

Chapter 4

Adhesion, Permeability and Mechanical Properties of Multilayered Blown Films using Maleated Low-Density Polyethylene Blends as Adhesion-Promoting Layers

4.1 Introduction

Coextrusion is a process in which two or more polymers are extruded simultaneously and joined together to form a single structure having different properties in each layer and to achieve a broad range of properties that are not available in any of the individual materials alone. In recent years, the packaging and container industries have paid increasing attention to the development of new or improved products formed by coextrusion, such as multilayer sheets, multilayer films, and multilayer containers [1–3]. The number of layers comprising these materials depends on the required end-use properties and the availability of polymer combinations suitable for specific applications.

Recently, it has become common [4,5] in food packaging technology to coextrude multilayer films consisting of distinct layers that are barriers for oxygen and moisture. Polyethylene is an excellent moisture barrier for packaging, and its low cost, strength and ease of processing make it suitable for many applications. Its inability, however, to act as a barrier for oxygen, aromatics, and oils limits its potential applications. On the other hand, ethylene–vinyl alcohol copolymer (EVOH) possesses excellent barrier

properties to oxygen, aromatics, and oils [6–9]. Unfortunately, EVOH is highly sensitive to moisture, which alters its ability to acts as an oxygen barrier [10,11]. Therefore, using coextrusion to combine polyethylene and EVOH in a multilayer structure is very attractive for many demanding packaging applications, such as for food, drugs, and cosmetics. Typical commercial multilayer barrier films for food packaging contain EVOH as an oxygen barrier layer and polyethylene resins as the moisture barrier layer. This film possesses a multilayer structure in which outer PE layers protect an inner EVOH layer from continuous exposure to moisture. Because of the chemical dissimilarities between PE and EVOH, however, an extrudable adhesive polymer must be incorporated into the film as a tie layer that promotes adhesion. Graft copolymers are widely recognized as novel potential adhesive polymers for imparting improved adhesion. These copolymers are synthesized mainly by modifying polyolefin resins through the addition of functionality. This process is achieved by adding acid or anhydride units to polyolefins through grafting or by direct synthesis of copolymers. Tanaka et al. [12] have successfully developed a new generation of tie layer adhesives, by combining graft and polymer blending, that maintain high adhesive strengths after thermoforming and orientation. Botros studied three-layer films, tie/EVOH/tie, using a coextrusion cast-film process [13] and found that the tie layers bind to EVOH through covalent and hydrogen bonding. The failure mechanisms of the three-layer films were of a mixed cohesive/adhesive type. Kim et al. [14] have investigated the mechanical and transport properties of various combinations of two-layer films, including LDPE/tie, Nylon 6/tie and LDPE/Nylon 6. The tensile strength and modulus of a coextruded film follows the additivity rule and its permeability follows the inverse additivity rule [15]. Kamykowski studied the adhesive properties of five-layer coextruded cast films [16] and found that the adhesion properties generally improved upon increasing the overall

film thickness or the relative amount of the adhesive (maleic anhydride-grafted polypropylene). The molecular weight of the grafted resin had a small effect on adhesion. Homopolymer diluents outperform random copolymer diluents in their adhesion properties.

Having additional tie layers in a coextruded film makes the fabrication process more complex and expensive, because of the need in the coextrusion system for a specially designed die and additional extruders for the adhesive polymers. An alternative approach has been reported that overcomes this disadvantage by replacing the five-layer film coextrusion system with a three-layer film comprising EVOH as the central layer and LLDPE/LLDPE-g-MAH blends as the external layers [17,18].

In this paper, we report a method to eliminate the need for tie layers by using blends of low-density polyethylene (LDPE) and linear low-density polyethylene grafted with maleic anhydride (LDPE-g-MAH) that promote adhesion between LDPE and EVOH in coextruded three-layer blown films. We investigated the mechanical properties of the films, including their peel strengths, tensile properties, and tear strengths, and compared their oxygen and water vapor permeability to theoretical predictions [19]. These blown films could be a viable option for reducing the number of film layers in coextrusion processing.

4.2 Experimental

4.2.1 Materials

Commercial-grade, low-density polyethylene [LDPE, 6030F, M. I. (g/10 min, 190 °C, 2.16 kg) = 0.27, density = 0.922 g/cm^3] was supplied in pellet form by Formosa Plastic Corp. (Taiwan). The ethylene–vinyl alcohol copolymer [EVOH, F101A, ethylene

content (mol %) = 32, M. I. (g/10 min, 190 °C, 2.16 kg) = 1.6, density = 1.19 g/cm^3]

was provided in pellet form by Kuraray Co. (Japan). The adhesive, Modic-AP L502,

was obtained in pellet form from Mitsubishi Chemical Corp. (Japan). It is a low-density

polyethylene-grafted maleic anhydride [LDPE-g-MAH, M. I. (g/10 min, 190 °C, 2.16

kg) = 1.0, density = 0.93g/cm^3].

4.2.2 Preparing Blends

LDPE-g-MAH was dried in a vacuum oven for 24 h period at 50 °C before blending.

Blends of LDPE with different amounts of LDPE-g-MAH (0, 5, 7.5, 10, 12.5, 15, 20,

and 25 wt%) were prepared in pellet form by melt mixing in a twin-screw extruder

operating at 210 °C and 40 rpm.

4.2.3 Preparing Multilayer Films

Prior to processing, EVOH was dried in a vacuum oven for 24 h at 60 °C. The

extruded blends (the external layers) were coextruded with EVOH (the internal layer)

through a three-layer coextrusion blown-film die (inner diameter = 97.6 mm; gap

thickness = 1.2 mm) at 230 °C. A 42-mm-diameter extruder (L/D = 28) was used for the

extruded blends and a 25-mm-diameter extruder (L/D = 28) was used for EVOH. All

extruders were attached with gear pumps to control the thickness of individual

component layers precisely. The ratios of take-off and blow-up were 3.5 and 2.5,

respectively. Three-layer films were fabricated with EVOH as the internal layer (overall

16.6 wt%) and blends of LDPE and LDPE-g-MAH (0, 5, 7.5, 10, 12.5, 15, 20 or 25

wt% of LDPE) as the external layers (overall 83.4 wt%). The thickness of all the

three-layer films produced, irrespective of the relative amount of LDPE-g-MAH, was

150 µm (blend, 130 µm; EVOH, 20 µm). We also prepared three-layer films having

overall EVOH content of 7.9, 13, 17.1, 21.2 or 24.4 wt% (internal layer) and a blend of

LDPE with 15-wt% of LDPE-g-MAH (external layers). Table 4-1 shows the thicknesses

of these three-layer films with respect to the EVOH content. To allow theoretical

predictions to be made, we also prepared monolayer film samples of LDPE, EVOH and

LDPE-g-MAH under the same processing conditions.

4.2.4 Preparing Specimens for Measuring Peel Strengths

Film samples were cut into strips (25 mm × 300 mm) and delamination was initiated

at one end by soaking the tips of each strip in formic acid (HCOOH) for ca. 4 h.   The

corner of a strip was pulled repeatedly with tweezers until we observed a slight

indication of delamination. The delamination was then propagated throughout the width

of the strip. The peel strengths of the three-layer films were measured at 23 °C by

T-type using a tensile tester with a crosshead speed of 25.4 cm/min, following the

procedure described in ASTM D1876. At least ten samples were tested to obtain

average values.

4.2.5 Analysis by FTIR Spectroscopy

The interactions at the interface between the layers of the blend and EVOH were

analyzed by Fourier transform infrared (FTIR) spectroscopy as a function of the content

of LDPE-g-MAH and EVOH using a Bio-Rad FTS-165. At least 32 scans at a

resolution of 4 cm^{-1} were signal-averaged. The hydrogen bonding was also analyzed by

FTIR spectroscopy.

4.2.6 Measuring Tensile Properties

The tensile properties of the three-layer films, including tensile strength, tensile

modulus and ultimate elongation, were measured by a tensile tester at 23 °C and a relative humidity of 50% in both the machine direction (MD) and the transverse direction (TD), following the procedure described in ASTM D882. At least ten samples were tested to obtain average values.

4.2.7 Measuring Tear Strength

The tear strengths of the three-layer films were measured by a tensile tester at 23 °C and a relative humidity of 50% in both the machine direction (MD) and the transverse direction (TD), following the procedure described in ASTM D1938. At least ten samples were tested to obtain average values.

4.2.8 Measuring Oxygen Permeability

The oxygen permeability properties of the three-layer films were measured using a Lyssy L-100-5000 Gas Permeability Tester [20], following the ASTM D1434. The oxygen permeability of the films was measured at 23 °C and a relative humidity of 0%. The temperature was controlled by a water bath.

4.2.9 Measuring Water Vapor Permeability

Water vapor permeability properties of the three-layer films were measured using Lyssy L-80-5000 Water Vapor Permeability Tester [21], following the ASTM E96. The water vapor permeability of the films was measured at 38 °C and a relative humidity of 90%. The temperature was controlled by a water bath.

4.3 Results and Discussion

Table 4-2 lists the tensile, tear and barrier properties of individual component materials. It is seen that the LDPE-g-MAH exhibit almost the same values in all mechanical and barrier properties as LDPE. The EVOH has much better tensile strength, modulus, tear strength and oxygen barrier property than both LDPE and LDPE-g-MAHH. On the other hand, LDPE and LDPE-g-MAH exhibit higher tensile elongation and water vapor barrier property. We assume that these properties of the blends are not affected significantly by the relative amount of LDPE-g-MAH in LDPE due to the same level of properties as shown in Table 4-2.

4.3.1 Peel Properties

Figure 4-1 shows the peel strength as a function of the relative amount of LDPE-g-MAH. The peel strength increased slightly upon increasing the amount of LDPE-g-MAH and then increased sharply when the amount of LDPE-g-MAH was greater than 12.5 wt%. When the LDPE-g-MAH content was above 15 wt%, we observed in the three-layer films a concomitant elongation and break in the blend layer of the film in addition to peeling at the interface between layers of EVOH and blend. As mentioned above, this observation indicates that good adhesion exists between the blend and EVOH layers and, as a result, it changes the failure mechanism from adhesive to cohesive.

The interactions at the interface between the blend and EVOH layers were analyzed by FTIR spectroscopy as shown in Figure 4-2. Table 4-3 lists the absorbances of the ester bands near 1710 cm^{-1} and the hydroxyl bands near 3350 cm^{-1}. We observe a continuous increase in the intensity of the ester absorbance and a decrease in that of the

hydroxyl absorbance upon increasing the amount of LDPE-g-MAH. The increase in the ester band absorbance is attributed to covalent bonding between the carbonyl groups in LDPE-g-MAH and the hydroxyl groups in EVOH. These stronger interactions lead to an increase in the adhesion between the blend and EVOH layers, which is a property supported by the increasing peel strengths shown in Figure 4-1.

4.3.2 Tensile Properties

Figure 4-3 shows the tensile properties in both the machine direction (MD) and the transverse direction (TD) as a function of the amount of LDPE-g-MAH (0 to 25 wt%). In Figure 4-3(a), we see that the tensile strength does not change significantly in either the MD or the TD upon changing the relative amount of LDPE-g-MAH. The tensile strengths of three-layer films, however, are all lower than those of the films of the individual materials (see table 4-2). These results are much different from those reported for three-layer films of LDPE/tie/PS [15] and two-layer films of LDPE/tie, Nylon 6/tie and LDPE/Nylon 6 [14]. In these previous studies, the tensile strengths of the two- or three-layer films were found to follow the additivity rule [15]. Figure 4-3(b) shows that the elongation at break increases slightly as the relative amount of LDPE-g-MAH increases. It is believed that high-elongation materials, such as LDPE or LDPE-g-MAH, as shown in Table 4-2, block transverse crack propagation in the EVOH layer, which causes the elongation to be about twice that of the separate single EVOH film in both the MD and TD [15]. Figure 4-3(c) shows that the tensile modulus increases initially — up to 10 wt% for the MD and 5 wt% for the TD — with increasing the relative amount of LDPE-g-MAH, and then it stays constant This property is due to the much higher tensile modulus of EVOH, as shown in Table 4-3, which leads to improved tensile moduli for the three-layer films as a result of strong adhesion between LDPE and

EVOH.

4.3.3 Tear Properties

Figure 4-4 presents the tear strengths of the three-layer films investigated in both the MD and TD. A continuous decrease in tear strength is observed upon increasing the relative amount of LDPE-g-MAH. This property is due to the poor tear resistance of EVOH (see Table 4-2) and the increase in adhesion, i.e., the increase of the degree of chemical bonding. The crack propagation in EVOH continues relatively easily and this failure mechanism transfers to the blend layers because of the chemical bonding in the three-layer film structures. Thus, the better the adhesion, the easier it becomes for crack growth to occur through the entire three-layer film, which results in lower tear strengths.

4.3.4 Oxygen Permeability

Figure 4-5 presents the oxygen permeabilities of the three-layer films as a function of the relative amount of LDPE-g-MAH, and shows that it is almost constant. For the sake of comparison, this figure also shows the theoretical predictions of oxygen permeabilities using the inverse additivity rule [19]:

$$\frac{1}{P_{three-layer}} = \frac{\varphi_{blend}}{P_{blend}} + \frac{\varphi_{EVOH}}{P_{EVOH}} \qquad (4.1)$$

where φ is the volume fraction and P is the oxygen permeability. Table 4-2 lists the oxygen permeabilities of the individual component materials. A good agreement exists between the experimental and theoretical data. Figure 4-6 displays the experimental and theoretical oxygen permeabilities of the three-layer films as a function of EVOH content. As expected, the permeability decreases with increasing the relative amount of EVOH, and it agrees reasonably well with the theoretical prediction.

4.3.5 Water Vapor Permeability

Figures 4-7 and 4-8 present the water vapor permeabilities of the three-layer films as a function of the relative amounts of LDPE-g-MAH and EVOH, respectively. For the sake of comparison, the two figures also show the theoretical predictions made by Equation (4.1) and data of individual component materials (see Table 4-2). In Figure 4-7, we see that the water vapor permeability of the three-layer films is almost constant with respect to the LDPE-g-MAH content, but a significant discrepancy exists between the experimental data and the theoretical prediction. Figure 4-8 shows that upon increasing the EVOH content the water vapor permeability of the three-layer films decreases slightly and the discrepancy between the experimental data and theoretical prediction becomes larger. From these observations, we conclude that a constant relative amount of EVOH leads to an almost constant discrepancy between the experimental and theoretical data, but that increasing levels of EVOH result in larger discrepancies. This feature may be due to the increased amount of intramolecular hydrogen bonding in the EVOH layer, which allows barely any water vapor to pass through the three-layer films. Figure 4-9 shows the IR absorption spectra, viewed in the region of the hydroxyl band, of the three-layer films as a function of EVOH content. With increasing EVOH content, the absorption peaks of the hydroxyl bands near 3350 cm^{-1} shift towards lower wavenumbers as a result of the increasing degree of intramolecular hydrogen bonding [22,23]. The magnitude of the band shift is proportional to the strength of hydrogen bonding. The increased strength of hydrogen bonding makes it more difficult for water vapor to pass through the films, and results in a larger discrepancy observed between the experimental data and the theoretical prediction.

4.4 Conclusions

We have fabricated three-layer films, consisting of EVOH as the internal layer and blends of low-density polyethylene and low-density ethylene grafted with maleic anhydride (LDPE-g-MAH) as external layers, by a coextruded blown-film process. By investigating the adhesion, permeability and mechanical properties, we make the following conclusions: (1) The adhesion of three-layer films, consisting of incompatible layers, can be improved by using blends of maleated low-density polyethylene and low-density polyethylene as a result of ester bond formation, which can be analyzed by FTIR spectroscopy. (2) The tensile strength does not change with increasing LDPE-g-MAH content, but it results in a slight increase in elongation of both the MD and TD. The modulus is only slightly increased at low levels of the LDPE-g-MAH content, and is almost constant in the MD and TD when the amount of LDPE-g-MAH is greater than 10 and 5 wt%, respectively. (3) The tear strengths in both the MD and TD decrease significantly with increasing LDPE-g-MAH content as a result of the greater ease of crack propagation in EVOH that is transferred to the entire three-layer film by the improved adhesion. (4) The oxygen permeabilities of the three-layer films follow the inverse additivity rule upon varying the EVOH and LDPE-g-MAH contents. The water vapor permeabilities of the three-layer films, however, did not follow this rule because increasing degrees of hydrogen bonding result in reduced permeability.

4.5 References

1. D. K. Lee, U. S. Patent 6,544,661 (2003).

2. T. J. Kraft, E. P. Socci and M. K. Akkapeddi, U. S. Patent 200,3045,640 (2003).

3. H. Siewert and M. Thielen, *Kunst. Plast. Euro.*, **88**, 48 (1998).

4. F. Hensen, Plastics Extrusion Technology, Hanser, New York, 1997.

5. A. P. Sullivan, E. Baer, A. Hiltner, G. J. Castle, C. E. Bibbons and I. D. Sand, U. S. Patent 2,002,150,704 (2002).

6. R. H. Foster, *Packaging*, **32**, 70 (1987).

7. T. Iwanami, Y. Hirai, *Tappi J.*, **66**, 1404 (1983).

8. J. M. Lagaron, A. K. Powell, and G. Bonner, *Polym. Test.*, **20**, 569 (2001).

9. H. U. Beckmann, and Ch. Herschbach, *Kunst. Plast. Euro.*, **86**, 5 (1996).

10. Z. Zhang, I. J Britt and M. A. Tung, *J. Appl. Polym. Sci.*, **82**, 1866 (2001).

11. R. Gopalakrishnan, J. M. Schultz and R. Gohil, *J. Appl. Polym. Sci.*, **56**, 1749 (1995).

12. H. Tanaka, H. Shigemoto and H. Kawachi, *J. Plast. Film Sheet.*, **12**, 279 (1996).

13. M. G. Botros, *J. Plast. Film Sheet.*, **12**, 195 (1996).

14. Y. J. Kim, C. D. Han, B. K. Song, and E. Kouassi, *J. Appl. Polym. Sci.*, **29**, 2359 (1984).

15. W. J. Schrenk and T. Alfrey, *Polym. Eng. Sci.*, **9**, 393 (1969).

16. G. W. Kamykowski, *J. Plast. Film Sheet.*, **16**, 237 (2000).

17. S. S. Valdes, F. O. Villarreal, M. L. Quintanilla, I. Y. Flores, and L. F. Ramos de Valle, *Polym. Eng. Sci.*, **38**, 127 (1998).

18. J. V. Olmos, S. S. Valdes, and I. G. Yánez Flores, *Polym. Eng. Sci.*, **39**, 1597 (1999).

19. J. B. Faisant, A. Aït-Kadi, M. Bousmina and L. Deschênes, *Polymer*, **39**, 533 (1998).

20. Automatic Manometric Gas Permeability Tester Operator Manual, Model L100-5000, Lyssy AG (2001).

21. Automatic Manometric Water Vapor Permeability Tester Operator Manual, Model

L800-5000, Lyssy AG (2001).

22. L. Dai and L. Ying, *Macromol. Mater. Eng*. **287**, 509 (2002).

23. J. C. Speakman, "The Hydrogen Bond and Other Intermolecular Forces", The Chemical Society, London, 1975.

Table 4-1 Thickness of Individual Layers of Three-layer Films with various EVOH
contents.

Sample No.	Composition (wt%) Blend[*]/EVOH	Layer Thickness (μ m) Blend/EVOH
1	92.1/7.9	136/9
2	87/13	130/15
3	82.9/17.1	125/20
4	78.8/21.2	120/25
5	75.6/24.4	116/29

* blend = LDPE (85wt%) / LDPE-g-MAH (15wt%)

Table 4-2 Properties of films for Individual Component Materials.

Property	Material		
	LDPE (130μ m)	LDPE-g-MAH (130μ m)	EVOH (20μ m)
Tensile Strength MD/TD (MPa)	24.2/21.4	23.6/20.6	63/45
Tensile Elongation MD/TD (%)	670/720	690/750	280/210
Tensile Modulus MD/TD (MPa)	205/220	220/235	1590/1610
Tear Strength MD/TD (N)	9.9/12	10.3/12.4	<0.1/<0.1
Oxygen Permeability[a] (ml-mm/m^2-24hr-atm)×10^2	1300	1250	11
Water Vapor Permeability[b] (g-mm/m^2-24hr)×10^2	9	8.7	700

a 23   , 0% relative humidity

b 38   , 90% relative humidity

Table 4-3 IR absorbance of hydroxyl and ester bands of three-layer films with different

LDPE-g-MAH contents.

LDPE-g-MAH content (wt%)	Hydroxyl Band 3350cm-1	Ester Band 1710 cm-1
0	623.9	0.461
5	610.2	0.547
7.5	600.7	0.583
10	592.8	0.616
12.5	587	0.671
15	575.7	0.714
20	560.1	0.789
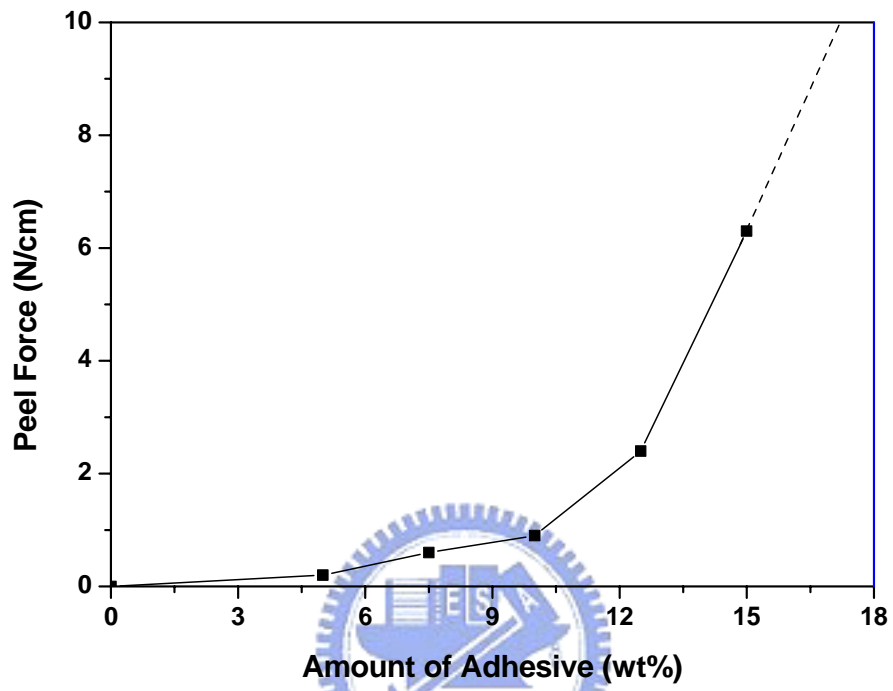
Figure 4-1 Peel Strength between LDPE/LDPE-g-MAH blend and EVOH of three-layer films as a function of LDPE-g-MAH content.
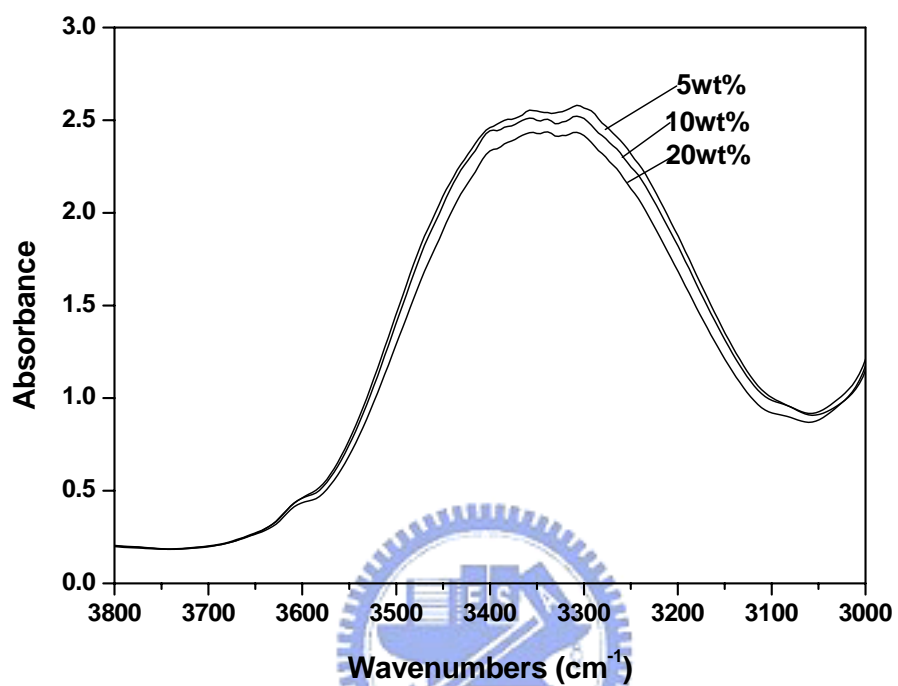
Figure 4-2(a) IR absorption spectra of three-layer films at the hydroxyl band with various LDPE-g-MAH contents.

Figure 4-2(b) IR absorption spectra of three-layer films at the ester band with various
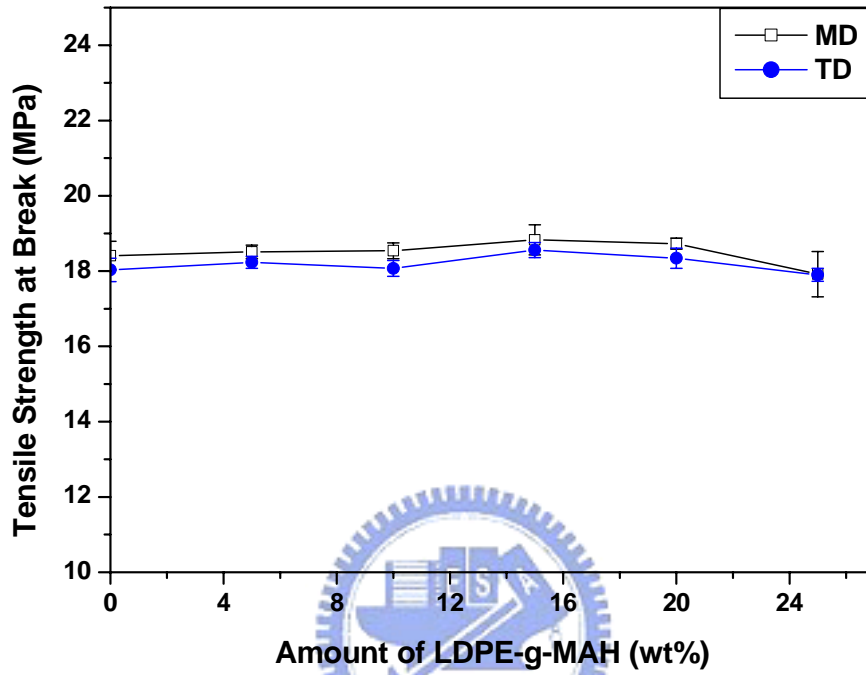
LDPE-g-MAH contents.

Figure 4-3(a) Strength at break of three-layer films as a function of LDPE-g-MAH content for both MD and TD.
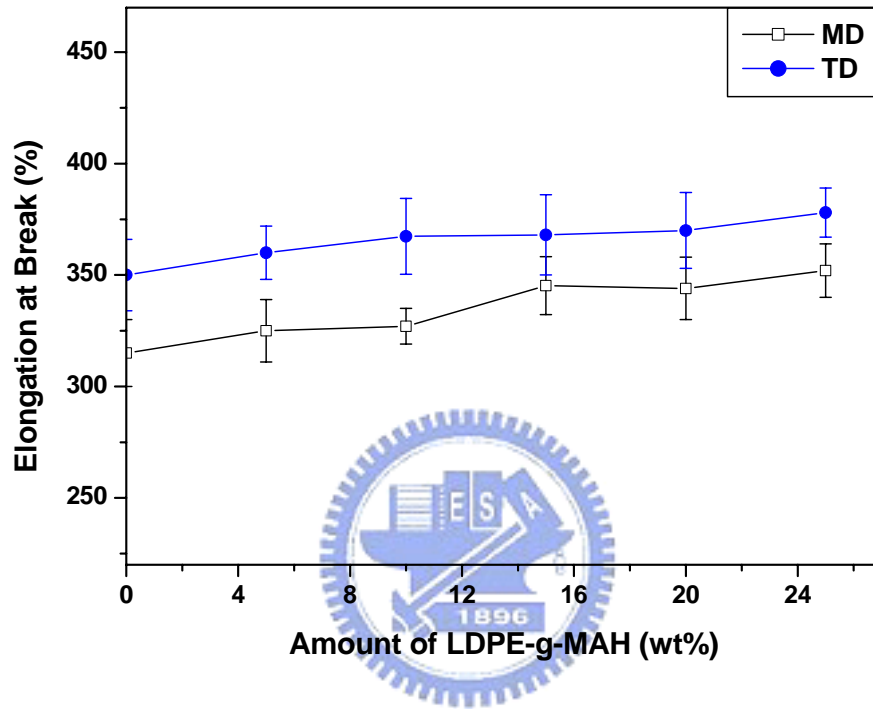
Figure 4-3(b) Elongation at break of three-layer films as a function of LDPE-g-MAH

content for both MD and TD.
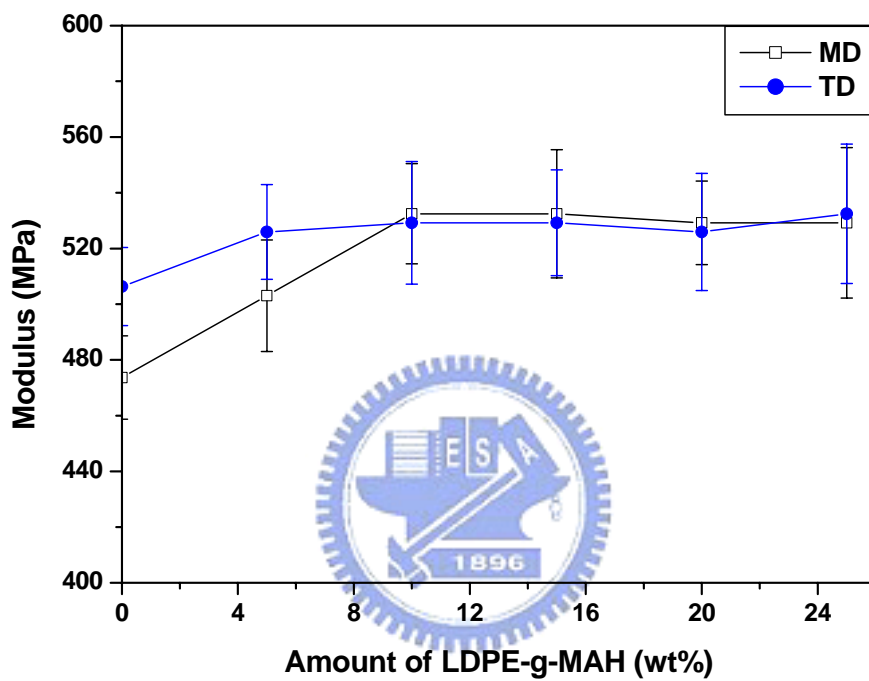
(c)

Figure 4-3(c) Modulus of three-layer films as a function of LDPE-g-MAH content for both MD and TD.
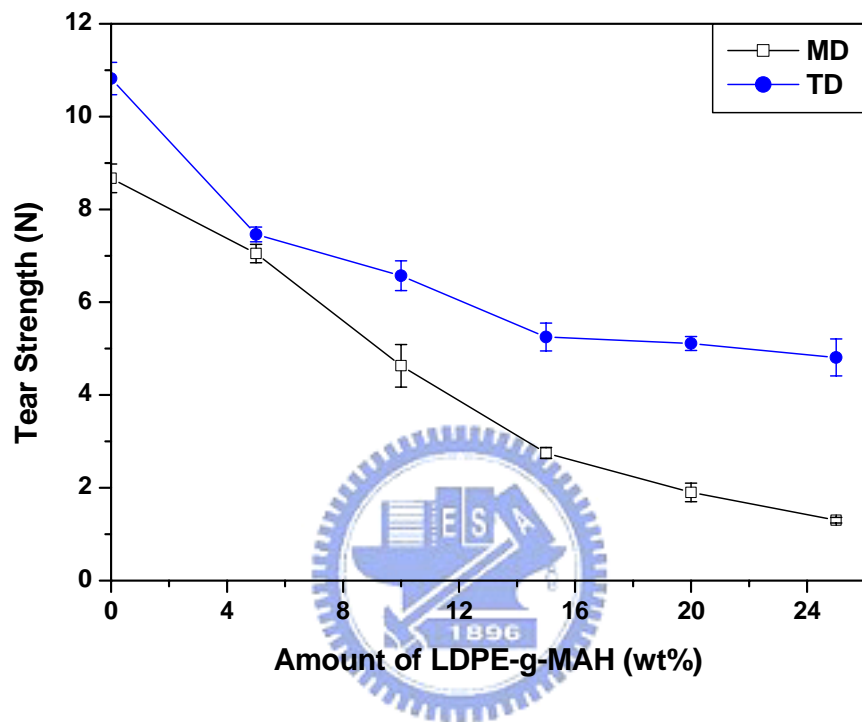
Figure 4-4 Tear strength of three-layer films as a function LDPE-g-MAH content for

both MD and TD.

Figure 4-5 Oxygen permeabilities of three-layer films as a function of LDPE-g-MAH content.
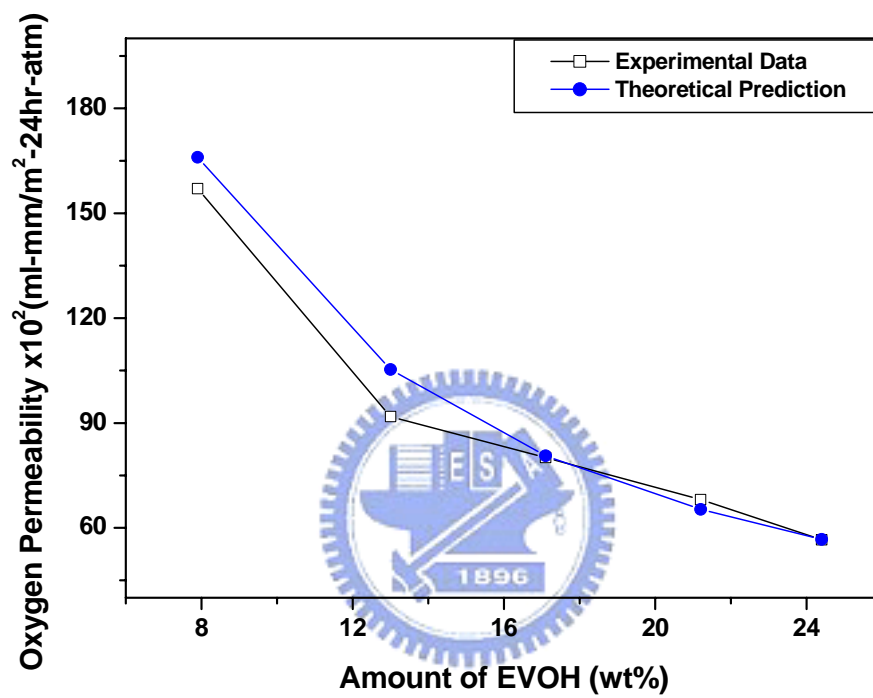
Figure 4-6 Oxygen permeability of three-layer films as a function of EVOH content.
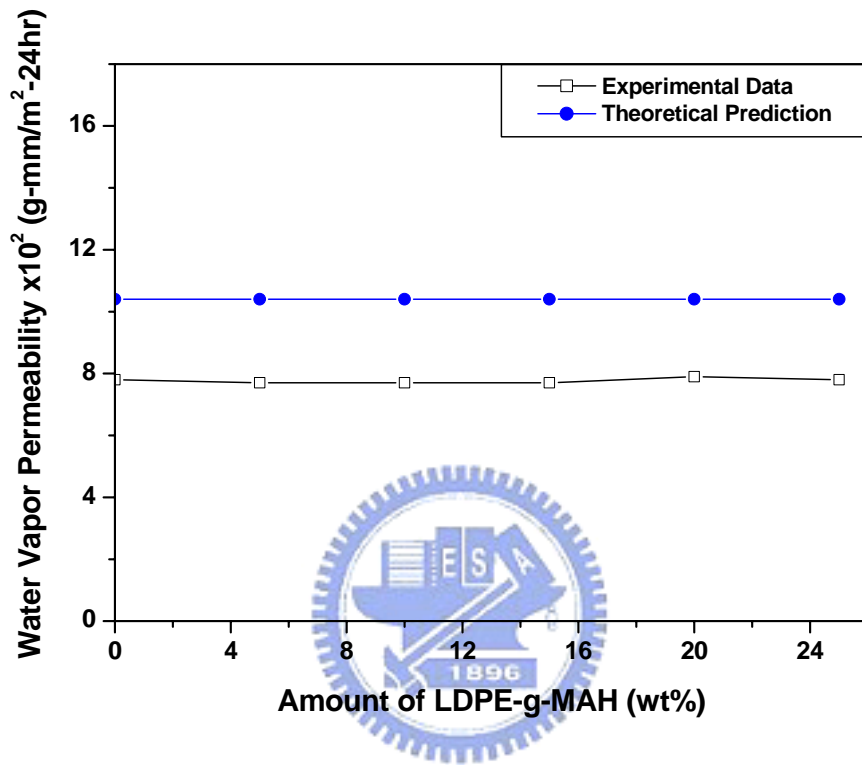
Figure 4-7 Water vapor permeability of three-layer films as a function of LDPE-g-MAH content.
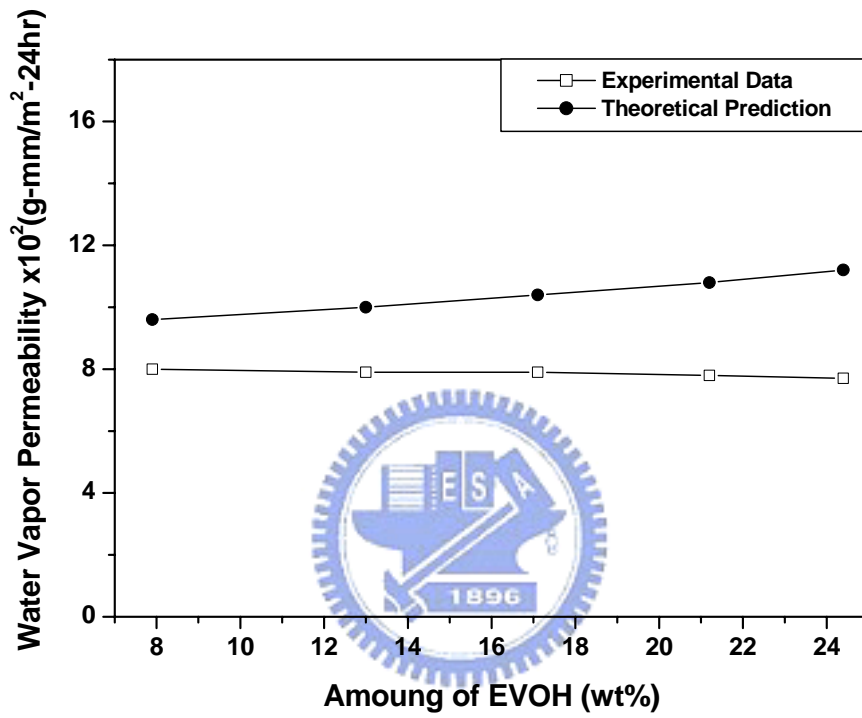
Figure 4-8 Water vapor permeability of three-layer films as a function of EVOH
content.
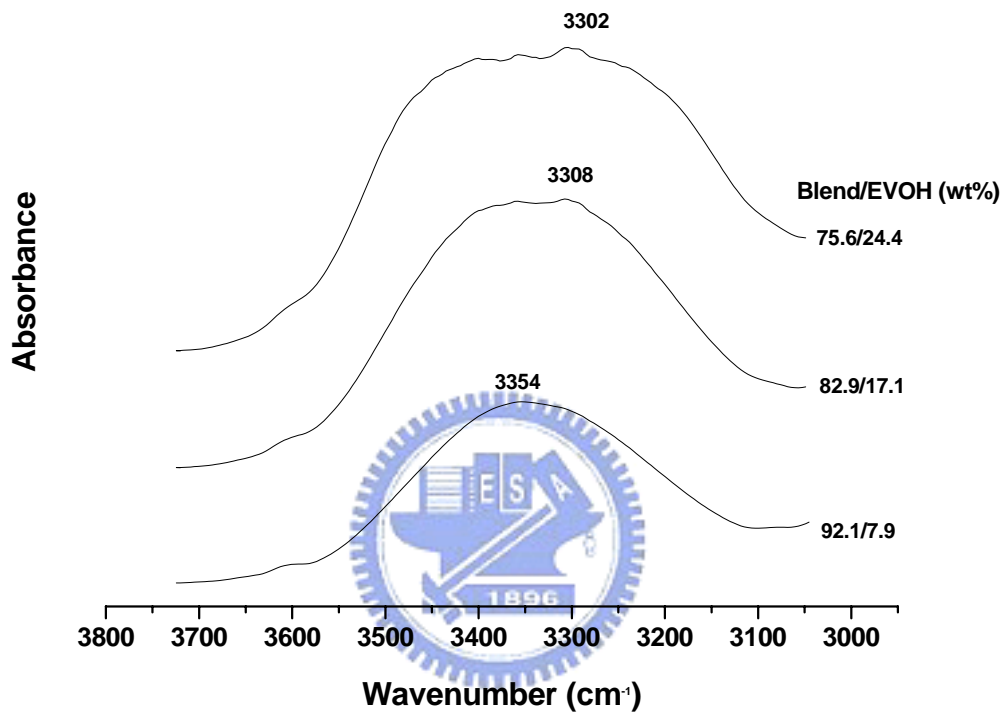
Figure 4-9 IR absorption spectra of three-layer films at the hydroxyl band with various
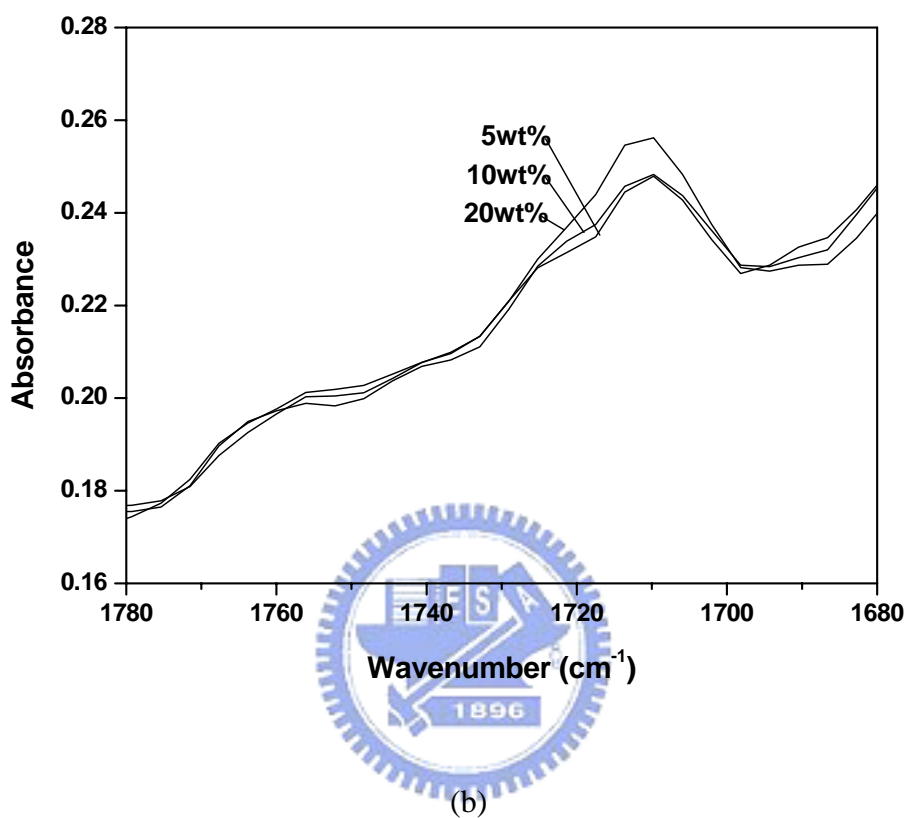
EVOH contents.

Chapter 5

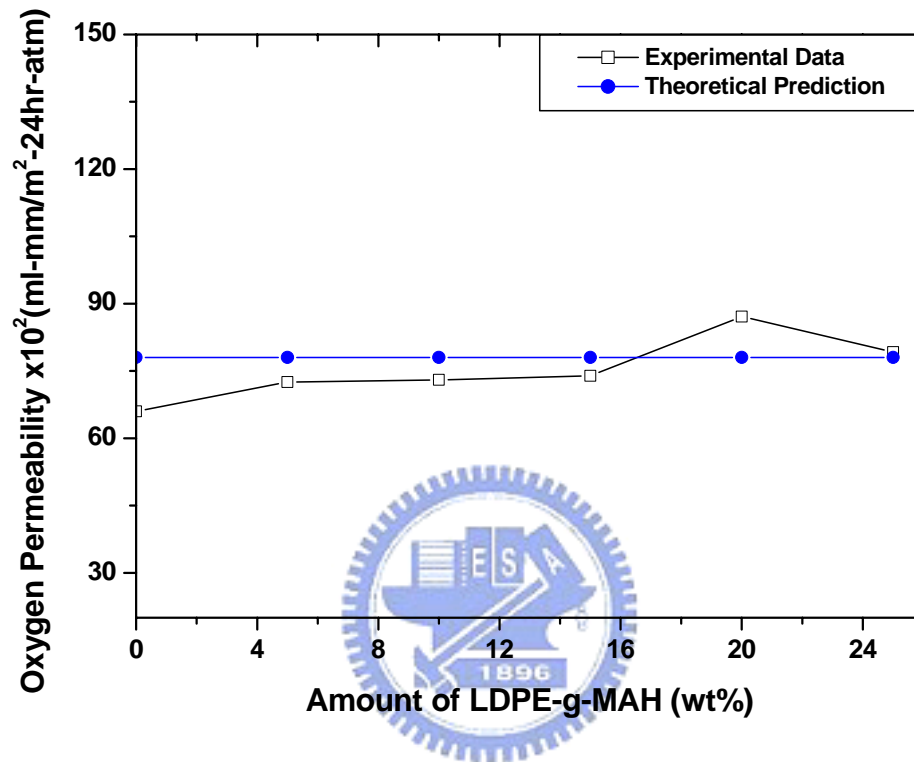## Morphological, Thermal, Barrier and Mechanical Properties of LDPE/EVOH Blends in Extruded Blown Films

5.1 Introduction

Plastic materials with good gas- and solvent-barrier properties offer a variety of advantages over metals and glasses for use in applications such as packaging films and containers. The most important requirement for the use of plastics in food packaging films is their impermeability to gases (i.e., the barrier property). Mechanical properties, especially tensile and tear properties, should also meet final product specifications. No single polymeric material, however, can offer all of the required properties and, therefore, a combination of polymers is generally employed.

Polyolefins, such as polyethylene (PE) and polypropylene (PP), are the most widely used resins applied as films for packaging because of their good mechanical and barrier properties towards moisture. Ethylene–vinyl alcohol copolymer (EVOH) has excellent gas-barrier properties and resistance to oil and organic solvents [1–4]. It is very sensitive to moisture, however, and loses its gas-barrier properties at high relative humidity because water acts as a plasticizer, weakening the hydrogen bonding between the polymer molecules [5–8]. Thus, in modern food packaging technology, it is common to coextrude multilayer films that consist of distinct layers that act as barriers to both moisture and gas. Coextruded multilayer films have been made by processing cap materials (such as PE or PP), tie resins, and the center barrier resins

[such as EVOH or PA (polyamide)] through their respective extruders and a feedblock, and then through a die to give typical five-layer films [9]. This technology, however, comes at a high cost and requires a complex degree of control, and the final product is not recyclable. A current alternative approach, employing polymer blends, appears to be beneficial for designing materials from a combination of a barrier material (EVOH) and a lower-cost matrix material (PE or PP). The blend processing can occur in a single-step operation and offers process versatility and low product cost [10,11]. The ultimate behavior of the polymer blend depends largely on the morphology of the blend. Previous studies have established that the formation of a laminar morphology in a polymer blend increases the tortuous path, which improves the barrier properties. [12–14]. The morphology of a polymer blend is determined by many factors, such as the interfacial tension, the blend composition, the viscosity ratio of the components, the blending sequence, and the processing conditions, which include the temperature, residence time, flow history, shear stress, and draw ratio [12–19].

One of the most important methods for controlling the blend morphology is modifying the interface between the phases, by addition of a compatibilizer, to obtain greater compatibility [20,34]. The compatibilizer may reduce the interfacial tension and, hence, increase the adhesion between phases and, as a result, allow a finer dispersion, a more stable morphology, and an improvement in mechanical [15, 21–24,35,36] and barrier properties [12–14]. The compatibilizer also affects the crystallization and melting behavior of the polymer blend [15,25,26].

Previous reports have described the preparation of samples of blend films that are relatively very thick—several hundreds of microns [15,19,27]—but, in most applications, films are usually required to have a thickness of about a hundred microns or less.   In this paper, we report relatively thinner film blends fabricated by an extruded blown-film process, using conventional processing conditions to produce

highly and biaxially oriented films. We investigated the effects that the compatibilizer has on the morphological, thermal, barrier, and mechanical properties of LDPE/EVOH blend films.

5.2 Experimental

5.2.1 Materials

Commercial grade low-density polyethylene [LDPE, 6030F, M. I. (g/10 min, 190 °C, 2.16 kg) = 0.27, density = 0.922 g/cm^3] was supplied by Formosa Plastic Corp. (Taiwan) in pellet form. The ethylene–vinyl alcohol copolymer was provided in pellet form [EVOH, F101A, ethylene content (mol%) = 32, M. I. (g/10 min, 190 °C, 2.16 kg) = 1.6, density = 1.19 g/cm^3] by Kuraray Co. (Japan). The compatibilizer, Modic-AP L502, was obtained from Mitsubishi Chemical Corp. (Japan). It is a low-density polyethylene-grafted maleic anhydride (LDPE-g-MAH).

5.2.2 Blend Film Preparation

In each blend, the weight ratio of LDPE to EVOH was 85:15, and the amount of the compatibilizer was 0, 0.5, 1, 2, 4, 6, 8 or 10 phr. All components were premixed by tumbling and then fed simultaneously into the single-screw extruder (diameter = 42mm, L/D = 28) attached to the blown-film die (inner diameter = 76 mm; gap thickness = 1.2 mm). The temperature profiles for the three heating sections of the extruder barrel and die were set at 190, 210, 230, and 240 °C, and the screw speed was 45 rpm. Above the exit of the die, the blend films were inflated and cooled with air and stretched by a take-off device. The ratios of take-off (take-off linear rate/linear rate of extrusion) and blow-up (diameter of bubble/diameter of blown-film die) were 8 and 2.6, respectively, and the frost-line height was 40 cm. Because of its

hygroscopic behavior, EVOH was dried carefully in a vacuum oven for 24 h at 60 °C before blending. For comparison, pure EVOH and LDPE films were prepared under the same processing conditions.

5.2.3 Morphological Analysis

We used two methods to obtain information on the different morphological behavior of the LDPE/EVOH blends upon the addition of LDPE-g-MAH. In the first method, specimens were prepared by fracturing the blend films cryogenically. The fracture surface was coated with a thin layer of gold and observed by scanning electron microscopy (SEM). In the second method, the blend films were placed between a pair of glass slides and treated in hot xylene, which resulted in selective dissolution of the LDPE matrix and separation of the EVOH dispersed phase. The separated EVOH domains were examined with an optical microscope (OM) so that we could determine the actual shape of the dispersed EVOH domains.
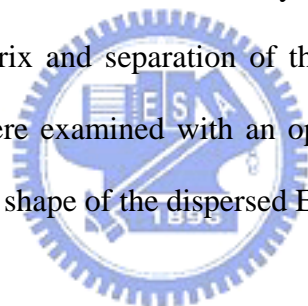
5.2.4 Thermal Analysis

Differential scanning calorimetry (DSC, TA instruments Q10) was used to study the melting temperature and crystallization of the blend films. In each heating cycle, the temperature was increased from 30 to 220 °C at a rate of 10°/min, maintained at 220 °C for a period of 5 minutes, and then cooled to 40 °C at –2°/min to erase the thermal history.

5.2.5 Permeability Measurements

The oxygen-permeability properties of blend films were measured using a Lyssy L-100-5000 Gas Permeability Tester, following the ASTM Standard Method D1434. The oxygen permeability of the blend films were measured at 23 °C with a relative
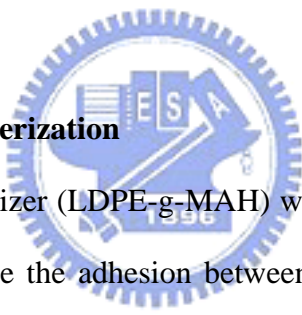
humidity of 0%. The temperature of both the testers was controlled by a water bath. The detailed procedure of tester is summarized in Ref. [29].

5.2.6 Mechanical Measurements

The mechanical measurements, including tensile and tear properties, of the blend samples were performed using a tensile tester at room temperature, following the procedures described in ASTM D882 and D1938, respectively. For both measurements, at least ten samples were tested in both the machine and transverse directions.

5.3 Results and Discussion

5.3.1 Morphological Characterization

In this study, the compatibilizer (LDPE-g-MAH) was used to reduce the interfacial tension and, hence, to increase the adhesion between the two immiscible phases of LDPE and EVOH. Furthermore, it also prevents coalescence of the dispersed particles during the melt flow through a die after the dispersed domains have been crushed by the high shear stress induced by screw rotation in the extruder [20]. Figure 5-1 shows SEM images of the morphological changes across the film thickness of the LDPE/EVOH blend films prepared with varying amounts of compatibilizer (from 0 to 8 phr). We observe more and thinner EVOH layers (laminar-like structures) when the amount of compatibilizer was increased. Figure 5-2 shows the optical micrographs of the LDPE/EVOH blend films prepared with various amounts of compatibilizer (from 0 to 10 phr). We see that the dispersed EVOH domain deforms into fibrils in the LDPE matrix when the amount of compatibilizer is small. This effect is due to efficient transfer of shear stress from the LDPE matrix to the dispersed EVOH

domain during extrusion and, subsequently, by the high drawing and cooling rates [16,28]. As the amount of compatibilizer is increased, the shape of the dispersed EVOH domain changes gradually from fibrils to small spherulites. This change is due to the fact that the increasing amount of compatibilizer results in a decrease in the interfacial tension and leads to smaller EVOH domains; it is difficult to deform the small particles during the extrusion and subsequent drawing and blowing processes [30,31].

5.3.2 Melting and Crystallization

Figures 5-3 and 5-4 show the first and second heating thermograms of LDPE/EVOH blend films having varying amounts of compatibilizer. The endothermic peak temperatures of both LDPE and EOVH are not changed significantly upon addition of the compatibilizer and remain almost constant during both heating cycles. In addition, these temperatures are roughly the same as those of the corresponding bulk polymers. The heat of fusion of LDPE remained constant upon the addition of the compatibilizer, but that of EVOH slightly increased and then remained constant when the amount of compatibilizer was greater than 4 phr. These results for LDPE are the same as those found by Lee and Kim [15], but our results for EVOH are somewhat different from their findings that the endothermic peak temperature and heat of fusion for EVOH decrease with increasing amounts compatibilizer as a result of constraint effects of the grafted EVOH in the dispersed EVOH phase. We observed no depression of either the melting temperature or the heat of fusion of EVOH. These results could be due to the existence of chemical bonds that form only at the surface of the EVOH domains, which is a situation that will not result in constraint effects of the grafted EVOH (EVOH-g-LD) or destruction of the inherent properties of EVOH.

Figure 5-5 displays the melting peak temperatures of LDPE/EVOH blend films

during the first and second heating cycles. The melting peak temperatures of the second heating cycle were higher by ca. 1 °C than those of the first for both LDPE and EVOH at all amounts of compatibilizer. The temperature difference may be due to the different cooling rates between the blown-film process and the DSC cooling process. Since the cooling rate in the DSC program is much slower than that in the blown-film process, the polymer chains of both LDPE and EVOH can crystallize better, which leads to the higher melting temperatures.

Figure 5-6 displays a comparison between the heats of fusion of the first and second heating cycles. The heats of fusion of LDPE for both heating cycles are very close, but the heat of fusion of EVOH for the first heating cycle is much higher than that of the second, which is an observation that we attribute to stress-induced crystallization resulting from stretching and molecular alignment (high and biaxial orientation) of the blown films during the blown-film process. This phenomenon explains why the heat of fusion of the uncompatibilized LDPE/EVOH blend films is slightly smaller than those of the compatibilized ones, as shown in Figures 5-3 and 5-4. The transfer of stress from the LDPE matrix to the dispersed EVOH domain in the uncompatibilized LDPE/EVOH blend is less than that of the compatibilized LDPE/EVOH blend during the extrusion and subsequently high drawing and blowing processes.

Figure 5-7 shows the cooling thermograms of LDPE/EVOH blend films having varying amounts of compatibilizer. The exothermic peak temperatures of both LDPE and EVOH do not change significantly upon addition of the compatibilizer and remain at almost a constant temperature during both the first and second heating cycles. Additionally, these temperatures are roughly equal to the values of the corresponding bulk polymers. The heats of crystallization also remain constant for both LDPE and EVOH, which is a situation that can be explained using the same

reasoning we used in discussing Figures 5-3 and 5-4.

5.3.3 Oxygen Barrier Properties

Figure 5-8 displays the effect of compatibilizer content on the oxygen permeability of LDPE/EVOH blend films, which are highly and biaxially oriented (blow-up ratio: 2.6; take-off ratio: 8). As indicated, the oxygen permeability is initially reduced upon the addition of compatibilizer. As the amount of compatibilizer increases, the oxygen permeability also increases slightly. There existed a better barrier oxygen property of blend films than that of pure LDPE as shown in Figure 5-8.

The results of oxygen permeability measurements of the compatibilized LDPE/EVOH blend films fabricated by high- and biaxial-oriented blown-film processes differ somewhat from those of PP/EVOH [19]. For PP/EVOH, there exists an optimal amount of compatibilizer for obtaining maximized barrier properties in well-developed laminar structures of blend films that were fabricated by the biaxially stretched cast-film process with a draw ratio of 3.5×3.5 at 160 °C. In our current study, although the blend films have well-developed laminar structures upon adding the compatibilizer, as shown in Figures 5-1 and 5-2, their oxygen permeabilities increase slightly as the amount of compatibilizer increases. This effect may be due to the poor miscibility between LDPE-g-MAH and LDPE/EVOH blend films fabricated by the blown-film process (highly and biaxially stretched), which results in the formation of microvoids during cooling because of the large difference in crystallization temperatures, as shown in Figure 5-7. During cooling in the blown-film process, the dispersed EVOH domain crystallizes earlier than does LDPE and becomes a heterogeneity in the LDPE matrix, which causes the stress of the matrix, induced by the high and biaxial orientation, to transfer to the EVOH domains by compatibilizer difficultly and results in a concentration of stress at the interface of the

two phases, which results in microvoids forming there. Although the EVOH domain yields more and thinner dispersed phases as the amount of compatibilizer increases, resulting in an increase in the contour length of the interface between the two phases as shown in Figure 5-2, this phenomenon increases the likelihood of microvoid formation during cooling and increases the oxygen permeability slightly.

In this study, uncompatibilized blend films were observed having poor barrier properties because oxygen molecules can diffuse easily through the microvoids formed at the interface between the two immiscible phases during the biaxially oriented blown film process.

5.3.4 Mechanical Properties

5.3.4.1 Tensile Properties

The tensile properties of our blend films in both the machine direction (MD) and the transverse direction (TD) are displayed in Figures 5-9 and 5-10. In Figure 5-9, we see that the MD tensile strength at the break of the blend films initially increases with increasing compatibilizer content of up to 1 phr, and then decreases and stays constant. Moreover, we have found that the addition of a compatibilizer to be a method for improving the mechanical properties of immiscible blends, and that the optimal compatibilizer content for maximizing MD tensile strength at the break is also a result of the morphology as shown in Figure 5-2. In Figure 5-2(c), the shapes of the dispersed EVOH domains are elongated fibrils aligned to the MD and the strength of the pure EVOH film is much higher than that of LDPE (Table 5-1). Thus, we believe that systems of LDPE/EVOH blends having low amounts of compatibilizer behave like fibril-reinforced composites [24,32,33]. As the shape of the dispersed EVOH domains changes from fibrils to spherulites, as shown in Figure 5-2, the effect of the fibril reinforcement disappears and the tensile strength decreases. The TD tensile

strength at break of the blend films increases upon increasing the compatibilizer content. Increasing the compatibilizer content results in reduction of the dispersed EVOH domain size, which leads to less stress concentrating at the interface between the dispersed phase and the matrix phase and results in increasing tensile strength in the TD. The elongation at break in the MD and TD initially increases with increasing compatibilizer content and then stays constant, as shown in Figure 5-10, which we attribute to enhancement of the interfacial adhesion between the LDPE and EVOH phases.

5.3.4.2 Tear Properties

Figure 5-11 displays the tear propagation strength in both the MD and TD. The MD tear propagation strength varies with the compatibilizer content, as does the TD tensile strength. On the other hand, the TD tear propagation strength varies with the amount of compatibilizer, as does that MD tensile strength. As a result, the failure mechanism of tear propagation in the MD and TD are like those of the tensile failure in the TD and MD, respectively. The TD tear strength has a much higher value than that of the MD, which is a phenomenon that is due to the high degree of orientation of the molecules in the MD.

5.4 Conclusions

In this study, LDPE/EVOH blend films, highly and biaxially oriented, were fabricated successfully by a blown-film process. By investigating the morphological, thermal, barrier, and mechanical properties of LDPE/EVOH blend films with respect to their compatibilizer content, we reach the following conclusions: (1) In the LDPE/EVOH binary system, the EVOH domains have fibril-like structures at low

amounts of compatibilizer and are spherulite-like at high levels. When the amount of compatibilizer increases, the EVOH domains yield more and thinner EVOH layers, which result from lower interfacial tension. (2) The melting and crystallization processes do not change significantly with the addition of the compatibilizer because there is little or no constraint effect of the grafted EVOH (EVOH-g-LD). (3) There is a large difference in the heat of fusion between the first and second heating cycles. During the blown-film process, high and biaxial orientation leads to stress-induced crystallization. The processing and thermal history is faded during the DSC isothermal program prior to the second heating cycle, which results in a lower heat of fusion than in the first. There is also a difference in the cooling rates of the blown-film process and the DSC program. The cooling rate in the DSC program ($2°$/min) is much slower than that in the blown-film process, and so the polymer chains of both LDPE and EVOH can crystallize more perfectly, which leads to higher melting temperatures. (4) Oxygen permeability of the LDPE/EVOH blend films is reduced slightly upon increasing the amount of compatibilizer as a result of the presence of microvoids between the two phases. The microvoids, which form during cooling in the blown-film process, result in more gas being able to pass through the LDPE/EVOH blend films and, hence, they increase the oxygen permeability. (5) We found that there is an optimal level of compatibilizer content (1 phr) for maximizing the MD tensile strength and elongation. On the other hand, increasing the amount of compatibilizer results in an increase in the TD tensile strength and elongation. The trend of tear strength with respect to the amounts of compatibilizer is similar to that observed for the tensile strength.

5.5 References

1. R. H. Foster, *Packaging*, **32**, 70 (1987).

2. T. Iwanami and Y. Hirai, *Tappi J.,* **66**, 1404 (1983)

3. J. M. Lagaron, A. K. Powell and G. Bonner, *Polym. Test.*, **20**, 569 (2001).

4. H. U. Beckmann and Ch. Herschbach, *Kunst. Plast. Euro.*, **86**, 5 (1996).

5. Z. Zhang, I. J. Britt and M. A. Tung, *J. Appl. Polym. Sci.*, **82**, 1866 (2001).

6. J. A. Wachtel, B. C. Tsai and C. J. Farrell, *J. Plast. Eng.*, **41**, 41 (1985).

7. B. C. Tsai and B. J. Jenkins, *J. Plast. Film Sheet.*, **4**, 63 (1988).

8. T. Iwanami and Y. Hirai, *Tappi J.*, **66**, 85 (1983).

9. G. W. Kamykowski, *J. Plast. Film Sheet.*, **16**, 237 (2000).

10. P. M. Subramanian, *Polym. Eng. Sci.*, **25**, 483 (1985).

11. P. M. Subramanian and V. Mehra, *Polym. Eng. Sci.*, **27**, 663 (1987).

12. S. Y. Lee and S. C. Kim, *Polym. Eng. Sci.*, **37**, 463 (1997).

13. R. Gopalakrishnan, J. M. Schultz and R. M. Gohil, *J. Appl. Polym. Sci.*, **56**, 1749 (1995).

14. M. R. Kamal, I. A. Jinnah and L. A. Utracki, *Polym. Eng. Sci.*, **24**, 1337 (1984).

15. S. Y. Lee and S. C. Kim, *J. Appl. Polym. Sci.*, **68**, 1245 (1998).

16. R. Gonzalez-Nunez, B. D. Favis, P. J. Carreau and C. Lavallee, *Polym. Eng. Sci.*, **33**, 851 (1993).

17. K. Min, J. L. White and J. F. Fellers, *Polym. Eng. Sci.*, **24**, 1327 (1984).

18. S. Wu, *Polym. Eng. Sci.*, **27**, 335 (1987).

19. J. H. Yeo, C. H. Lee, C. S. Park, K. J. Lee, J. D. Nam and S. W. Kim, *Adv. Polym. Tech.*, **20**, 191 (2001).

20. M. J. Folkes and P. S. Hope, *Polymer Blends and Alloys*, Blackie Academic & Professional, London, 1993.

21. R. Fayt, R. Jerome, and Ph. Teyssie, *J. Polym. Sci, Polym. Phys. Ed.*, **20**, 2209 (1982).

22. C. C. Chen and J. L. White, *Polym. Eng. Sci.*, **33**, 923 (1993).

23. R Holsti-Miettinen, J. Seppala, and O. T. Ikkala, *Polym. Eng. Sci.*, **32**, 868 (1992).

24. L. E. Nielsen and R. F. Landel, *Mechanical Properties of Polymers and Composites*, Marcel Dekker, New York, 1994.

25. O. T. Ikkala, R. M. Holsti-Miettinen and J. Seppala, *J. Appl. Polym. Sci.*, **49**, 1165 (1993).

26. H. S. Moon, B. K. Ryoo, and J. K. Park, *J. Appl. Polym. Sci.*, **32**, 1427 (1994).

27. H. Garmabi and M. R. Kamal, *J. Plast. Film Sheet.*, **15**, 120 (1999).

28. R. Gopalakrishnan, J. M. Schultz and R. M. Gohil, *J. Appl. Polym. Sci.*, **56**, 1749 (1995).

29. Automatic Manometric Gas Permeability Tester Operator Manual, Model L100-5000, Lyssy AG, 2001.

30. G. I. Taylor, *Proc. R. Soc. London, Ser. A,* **138**, 41 (1932).

31. G. I. Taylor, *Proc. R. Soc. London, Ser. A,* **146**, 501 (1934).

32. F. Avalos, M. Arroyo and J. P. Vigo, *J. Polym. Eng.,* **9**, 158 (1990).

33. M. Joshi, S. N. Maiti and A. Misra, *Polym. Compos.,* **15**, 349 (1994).

34. U. Sundararaj and C. W. Macosko, *Macromolecules*, **28**, 2647 (1995).

35. C. E. Scott and C. W. Macosko, *Polm. Eng. Sci.*, **35**, 1938 (1995).

36. C. W. Macosko, P. Guegan, A. K. Khandpur, A. Nakayama, P. Marechal and T. Inoue, *Macromolecules*, **29**, 5590 (1996).

Table 5-1 Tensile properties of pure LDPE and EVOH films for both MD (machine direction) and TD (transverse direction) (ASTM D882).

Material	Tensile Strength at Break (MPa) MD	Tensile Strength at Break (MPa) TD	Elongation at Break (%) MD	Elongation at Break (%) TD
LDPE	28	29	550	650
EVOH	60	55	270	250

(a)   (b)

(c)   (d)
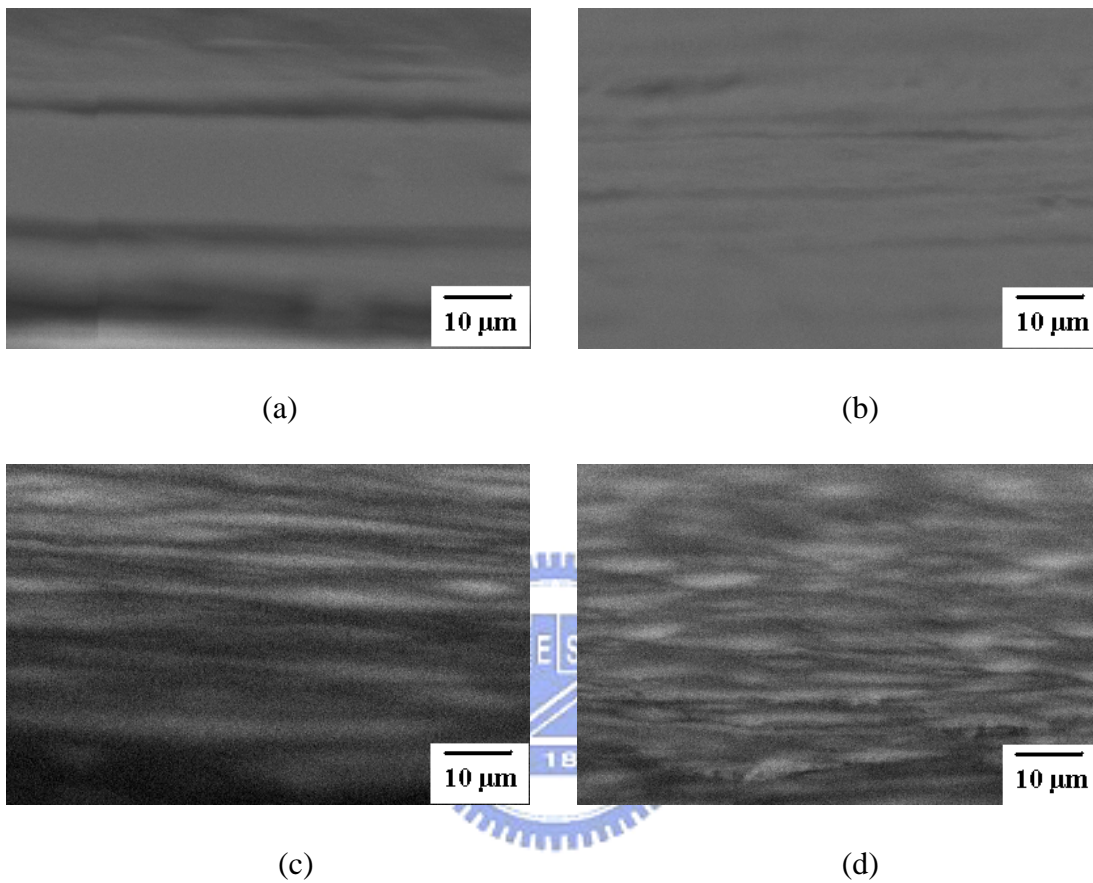
Figure 5-1 SEM micrographs of LDPE/EVOH blend films with various compatibilizer contents; (a) 0 phr, (b) 1 phr, (c) 4 phr and (d) 8 phr.
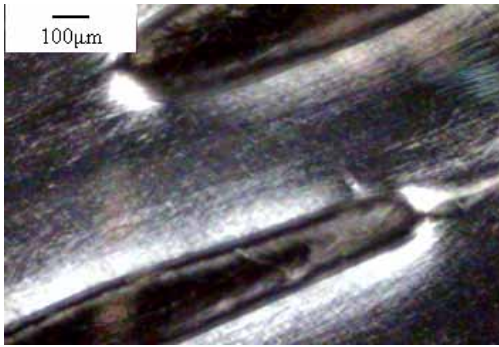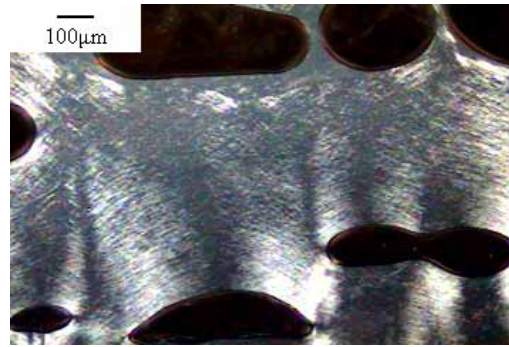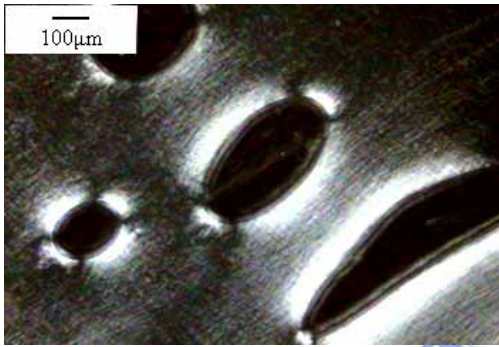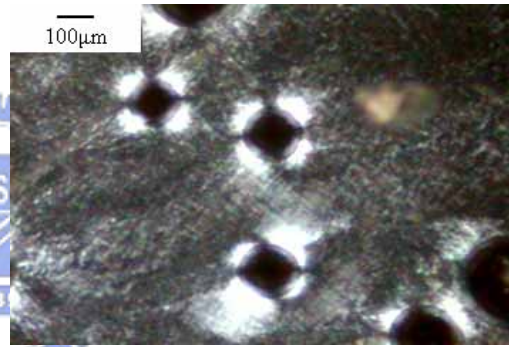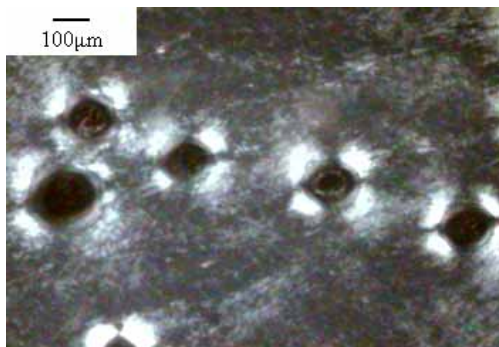
(a)　　　　　　　　　　　　　　　(b)

(c)　　　　　　　　　　　　　　　(d)

(e)

Figure 5-2 Optical micrographs of LDPE/EVOH blend films with various compatibilizer contents; (a) 0 phr, (b) 0.5 phr, (c) 1 phr, (d) 6 phr and (e) 10phr.
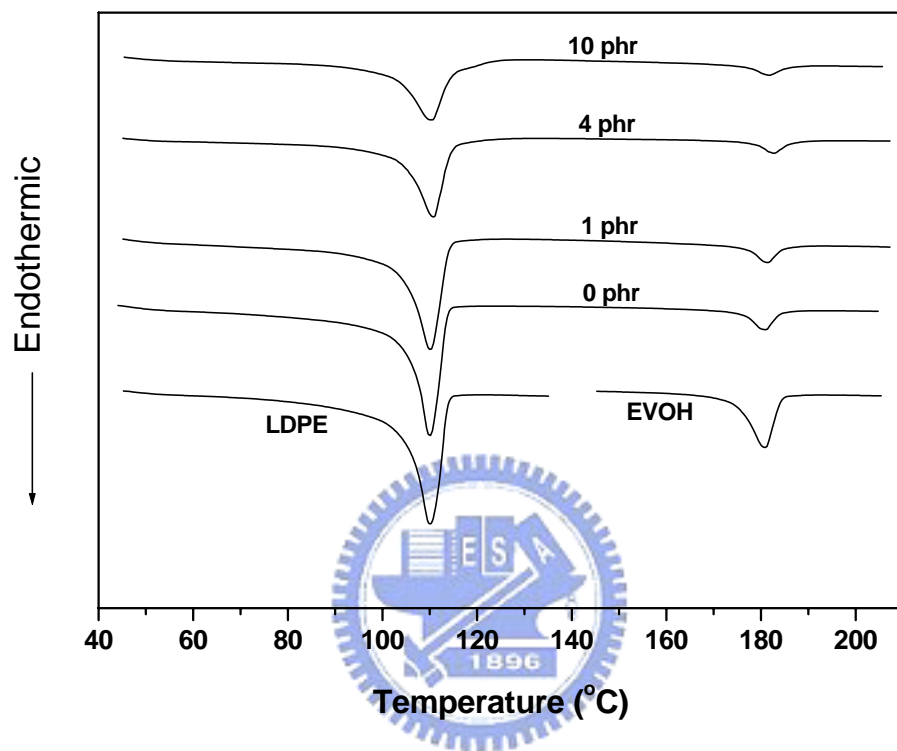
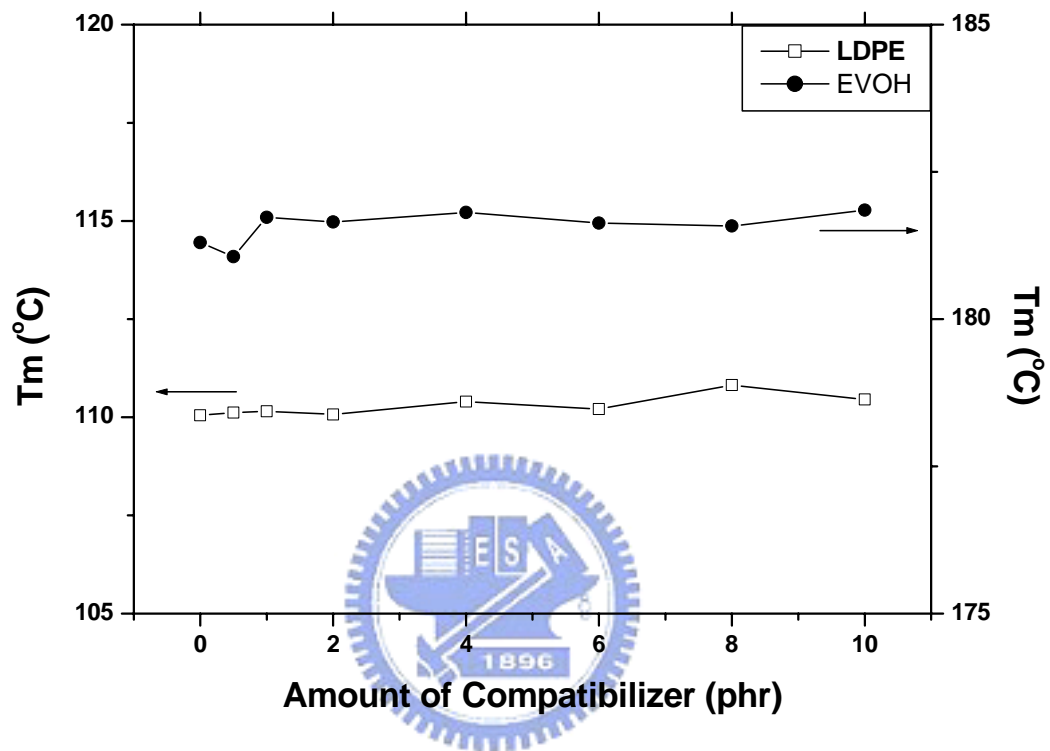Figure 5-3(a) The DSC 1st heating thermograms of LDPE/EVOH blend films with various compatibilizer contents.

Figure 5-3(b) The melting peak temperature of LDPE/EVOH blend films with various

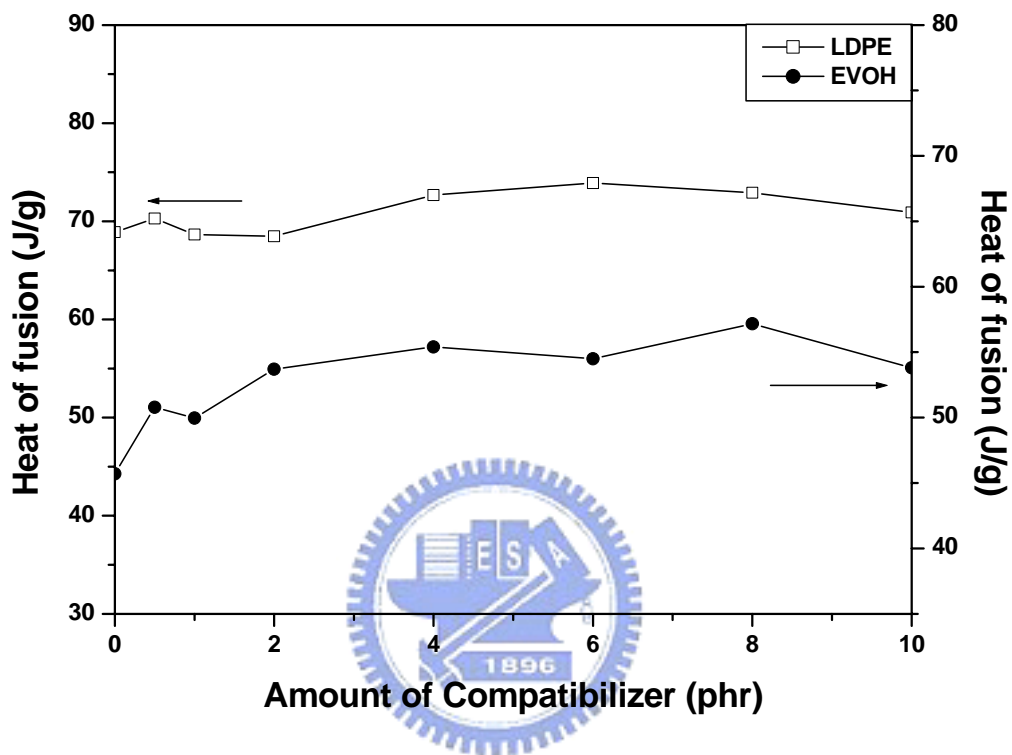compatibilizer in DSC 1st heating thermograms.

Figure 5-3(c) The heat of fusion of LDPE/EVOH blend films with various

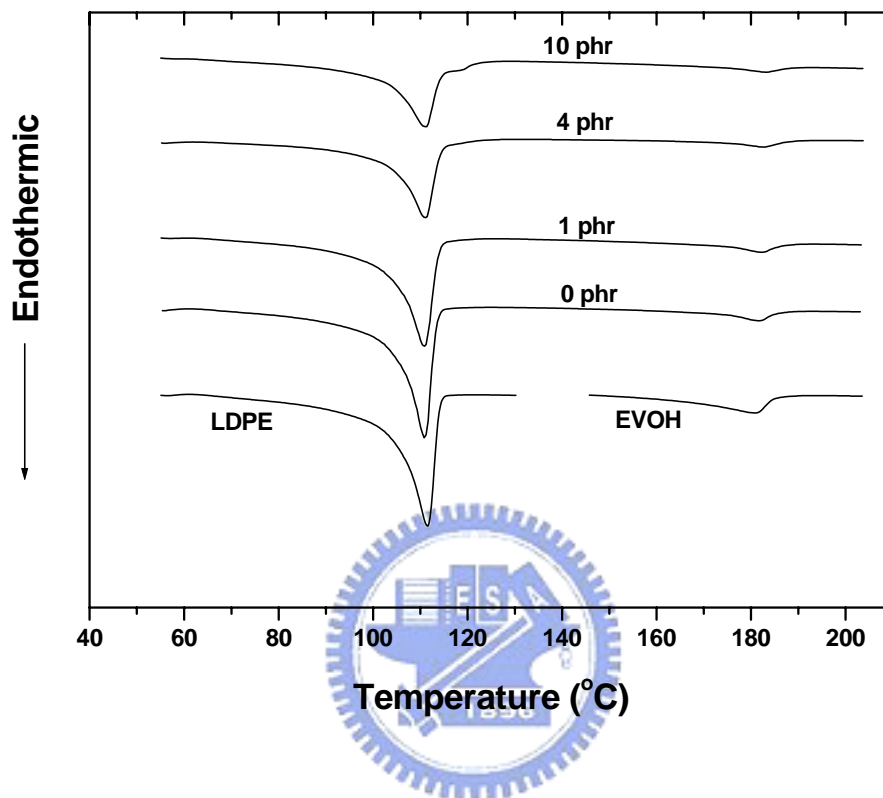compatibilizer in DSC 1st heating thermograms.

Figure 5-4(a) The DSC 2nd heating thermograms of LDPE/EVOH blend films with
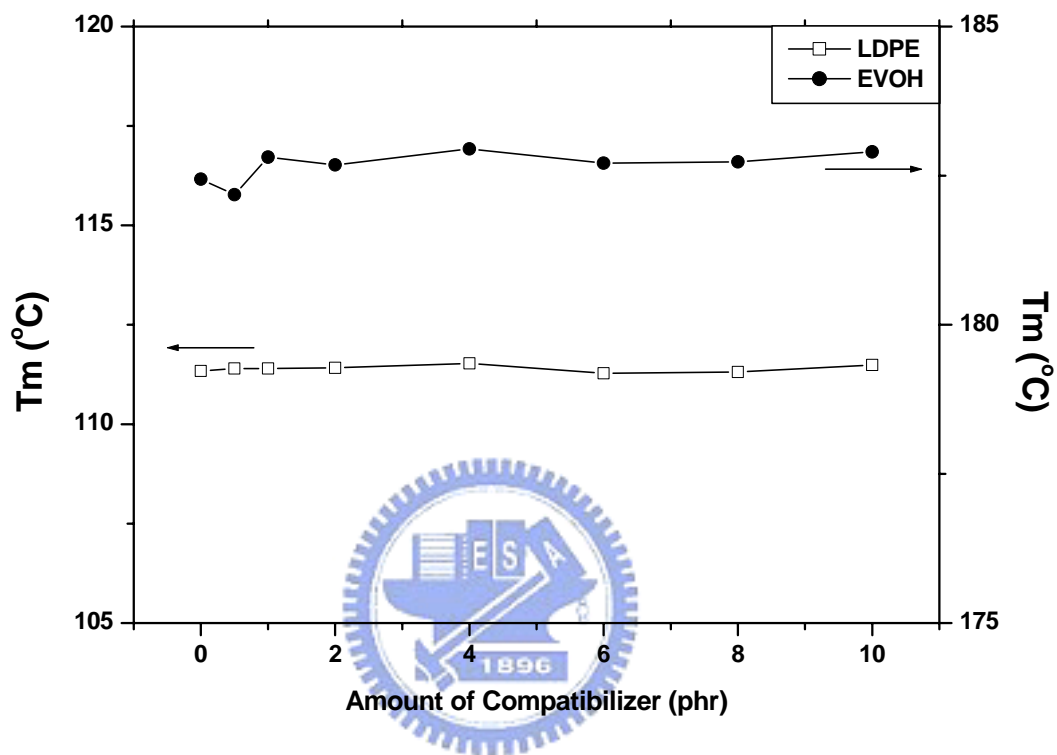
various compatibilizer contents.

Figure 5-4(b) The melting peak temperature of LDPE/EVOH blend films with various

compatibilizer in DSC 2nd heating thermograms.
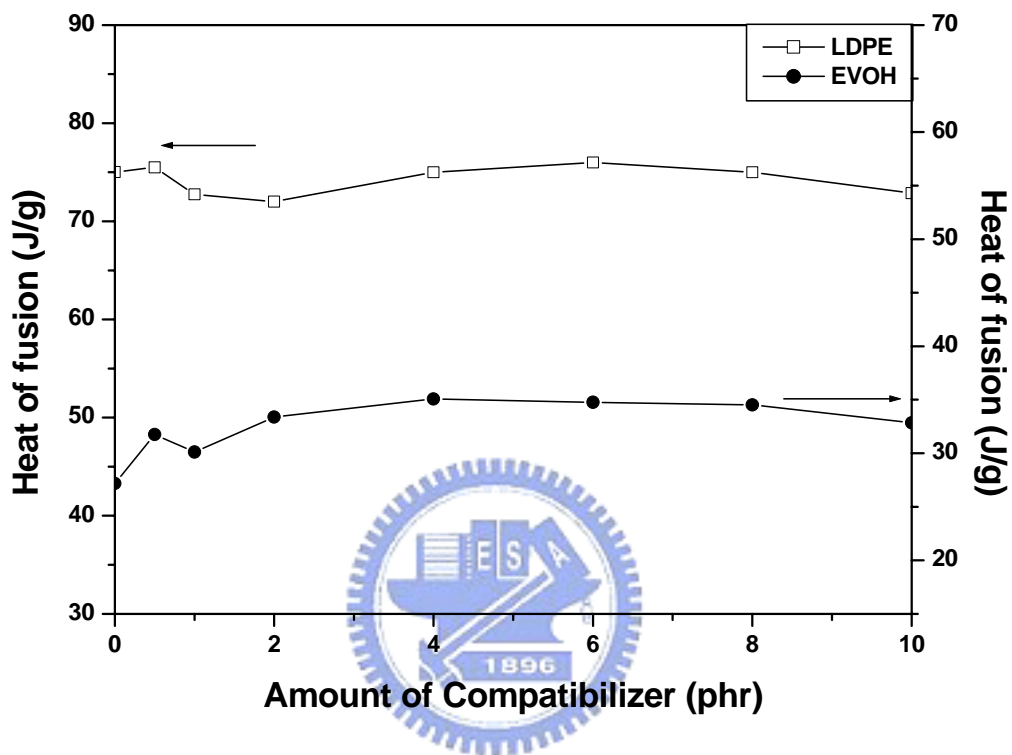
Figure 5-4(c) The heat of fusion of LDPE/EVOH blend films with various

compatibilizer in DSC 2nd heating thermograms.
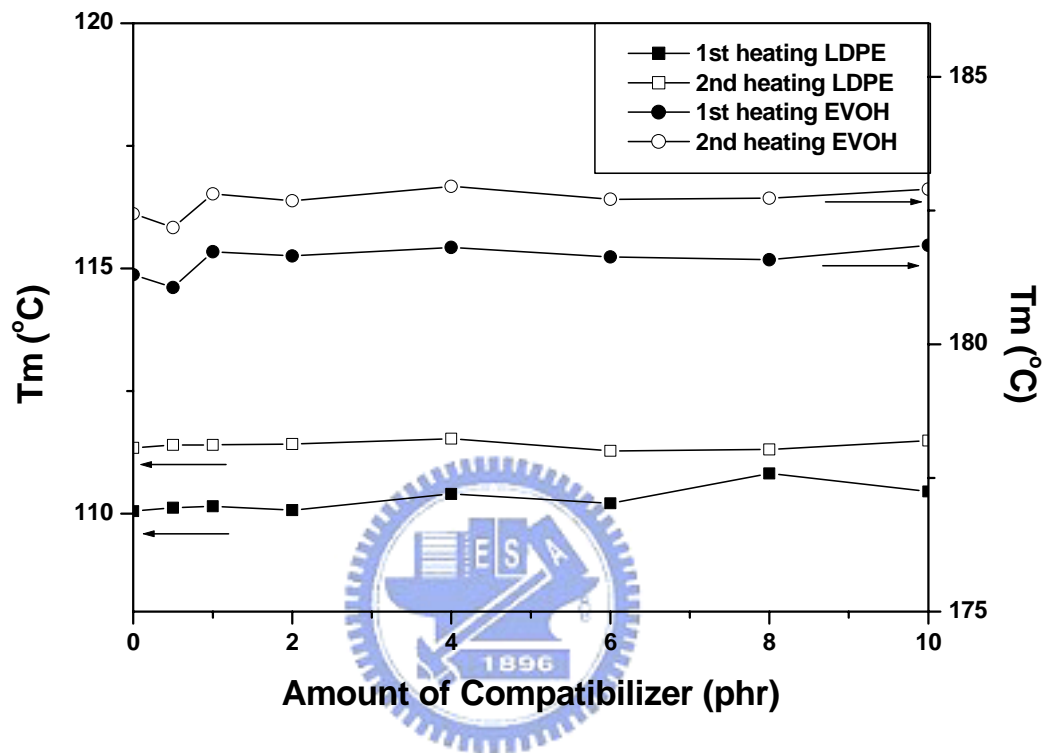
Figure 5-5 Melting peak temperatures of 1st and 2nd heating of LDPE/EVOH blend films with various compatibilizer contents.
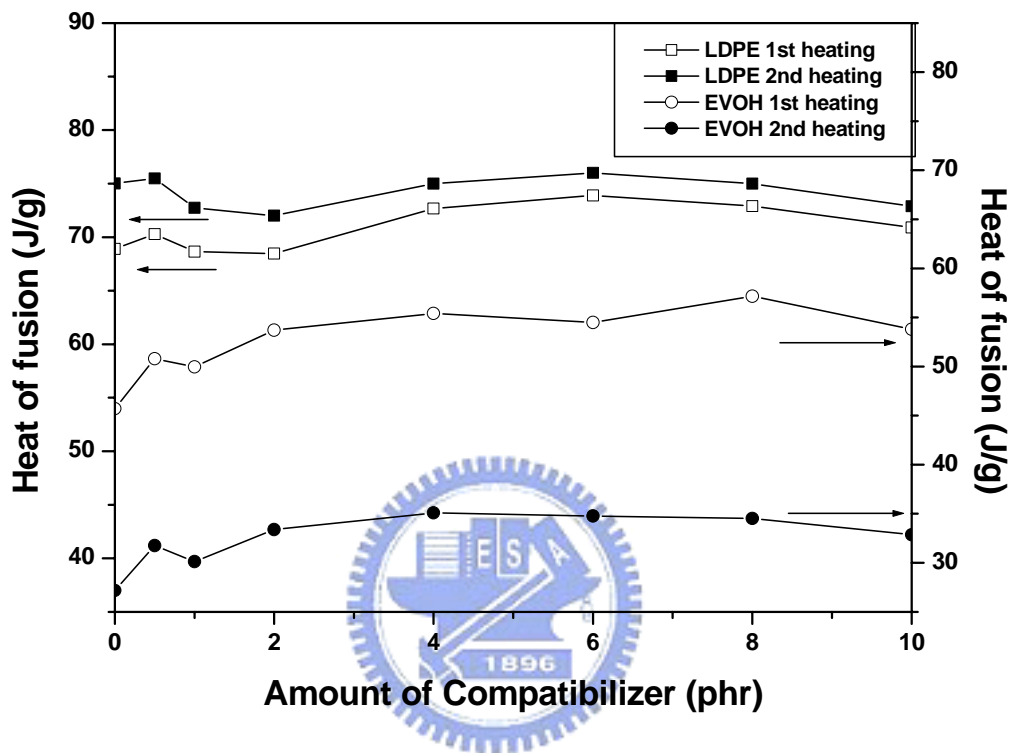
Figure 5-6 Heat of fusions of 1st and 2nd heating of LDPE/EVOH blend films with various compatibilizer contents.
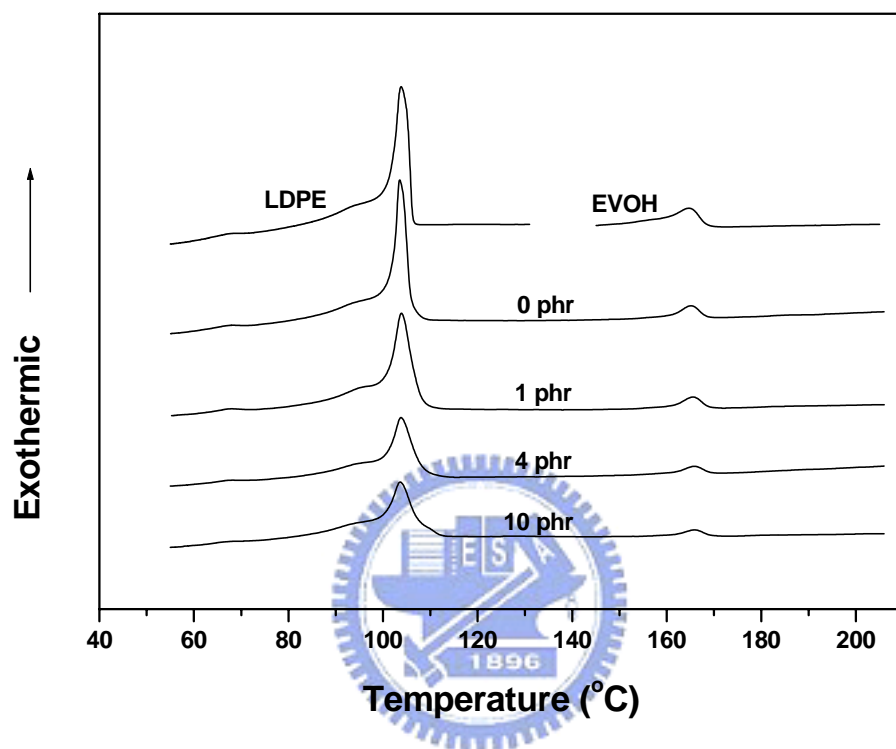
Figure 5-7(a) The DSC cooling thermograms of LDPE/EVOH blend films with various compatibilizer contents (cooling rate = 2 /min).
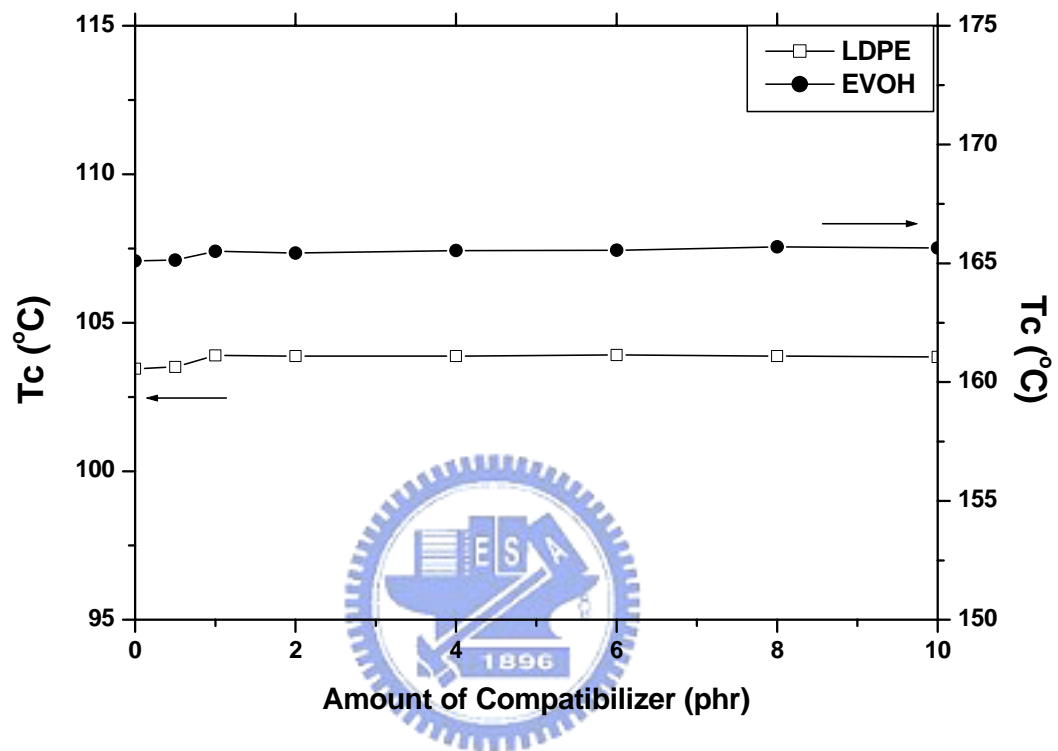
Figure 5-7(b) The crystallization peak temperature (T_c) of LDPE/EVOH blend films with various compatibilizer contents (cooling rate = 2 /min) in the DSC cooling thermograms.
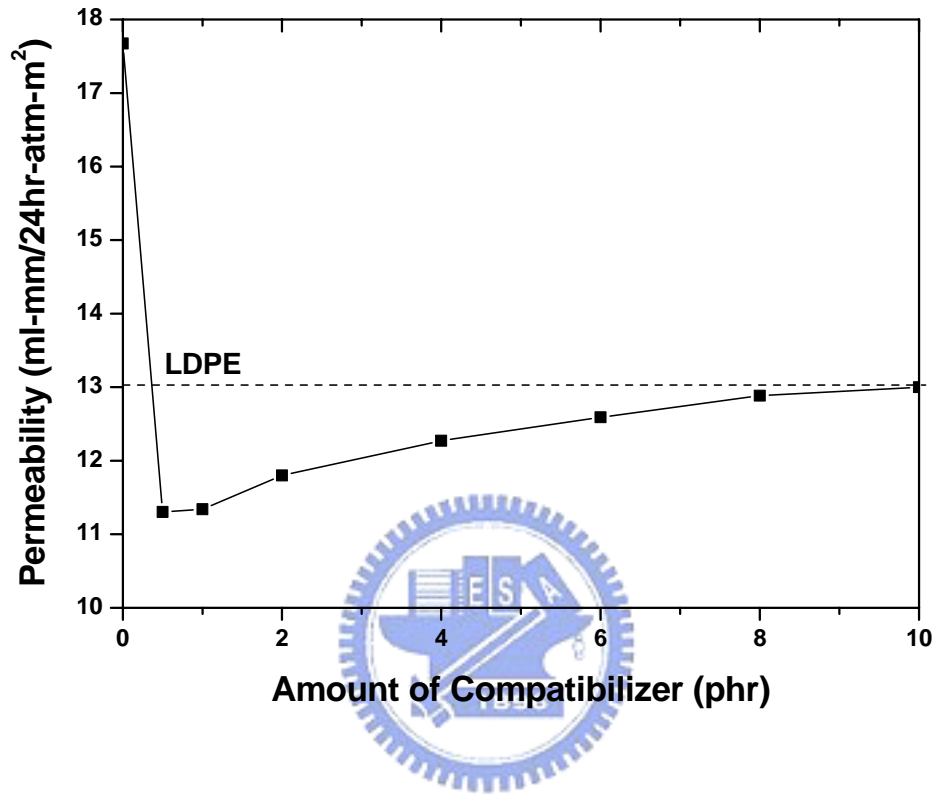
Figure 5-8 Oxygen permeability of LDPE/EVOH blend films with various compatibilizer contents. Dash line represents the oxygen permeability of LDPE.

Figure 5-9 Tensile strength at break of LDPE/EVOH blend films with various

compatibilizer contents for both MD (machine direction) and TD (transverse

direction).

Figure 5-10 Elongation at break of LDPE/EVOH blend films with various

compatibilizer contents for both MD (machine direction) and TD (transverse

direction).

Figure 5-11 Tear propagation resistance of LDPE/EVOH blend films with various

compatibilizer contents for both MD (machine direction) and TD (transverse

direction).

Chapter 6

Conclusions and Future Work

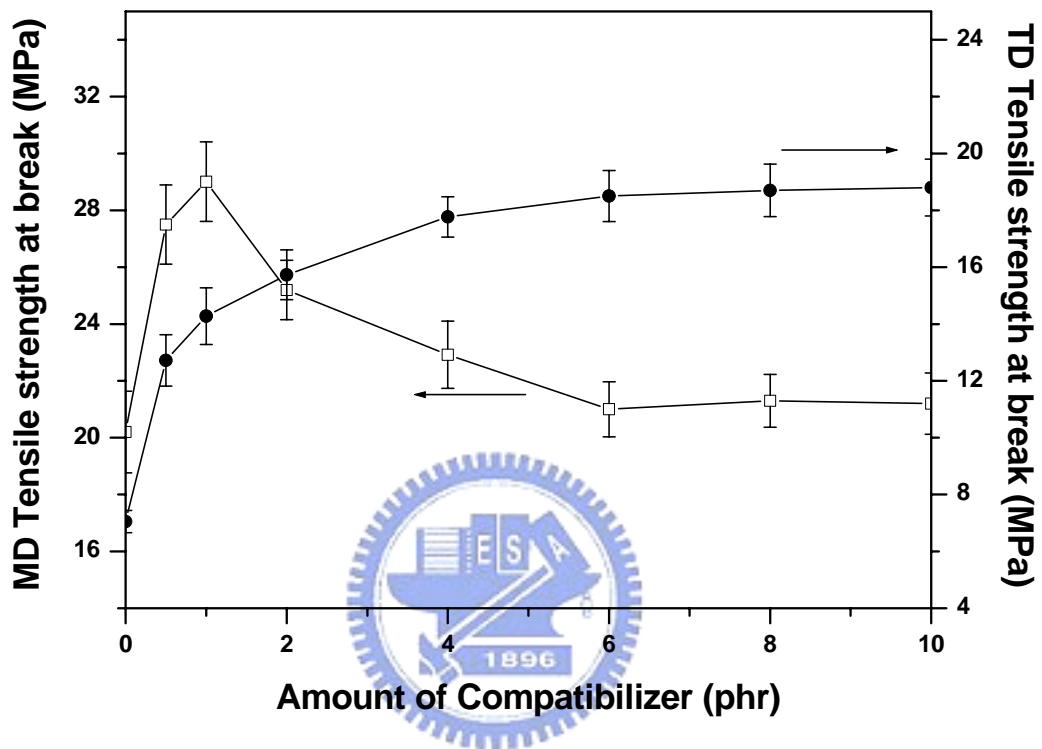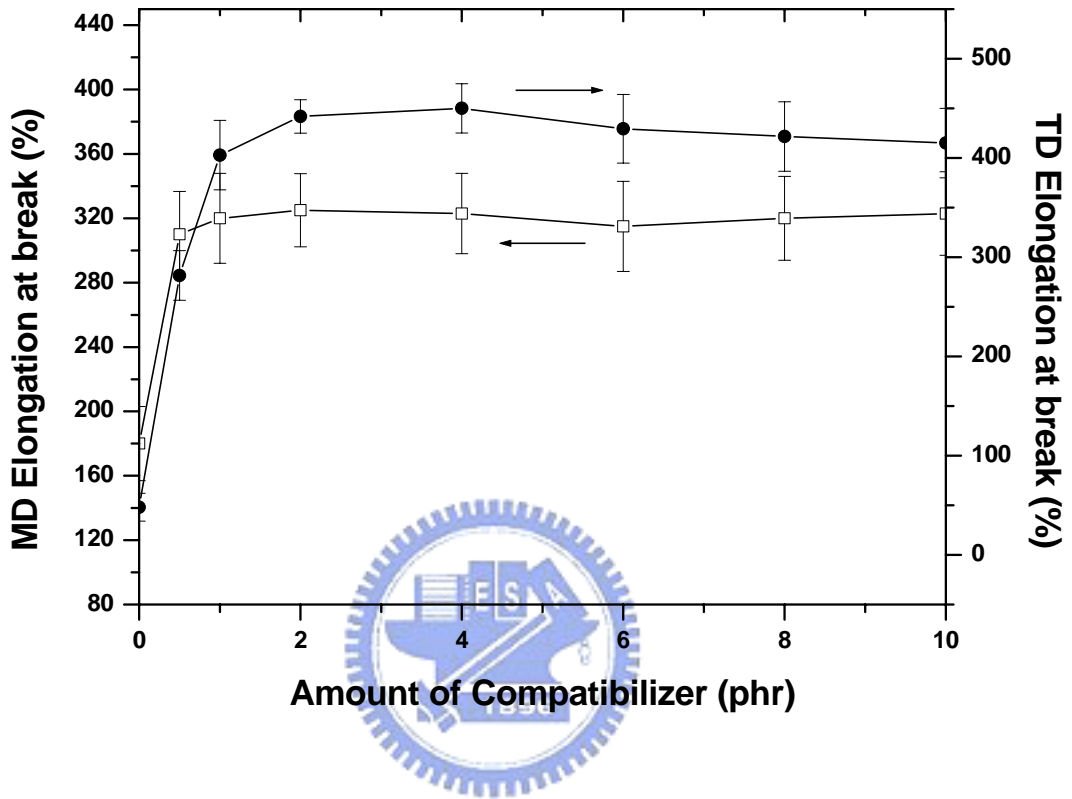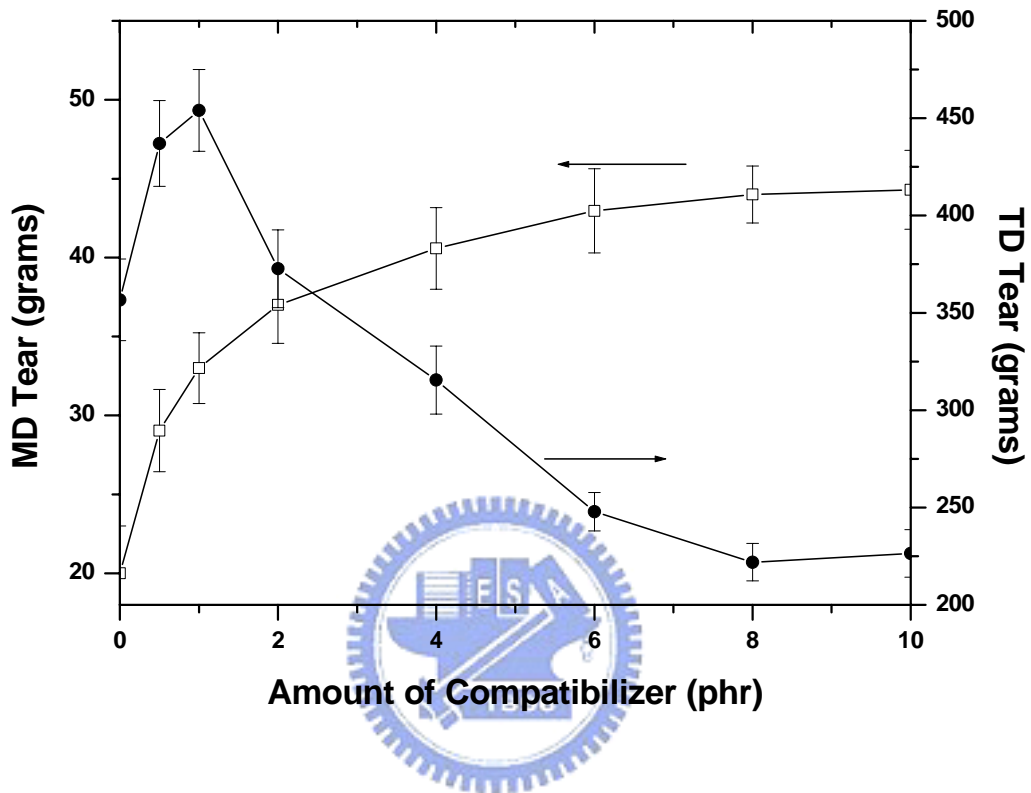In this study, we have successfully fabricated laminar polymeric films by coextrusion and blending processes. For a typical multilayer structure, HDPE/tie/PA-6 (A/B/C), which we fabricated by coextrusion, we investigated and predicted the film's permeability and tensile behavior. For another type of multilayer structure, blend/EVOH/blend (A/B/A), we investigated the adhesion, mechanical, and barrier properties. In addition, we also investigated a laminar polymeric film, LDPE/EVOH blend, which we fabricated by blending and a subsequent blown-film process, with respect to its morphological, thermal, barrier, and mechanical properties. According to the research undertaken during this study, we arise at the following conclusions:

For the HDPE/tie/PA-6 film

1. We have investigated the permeabilities of three gases, N_2, O_2, and CO_2, and water vapor. We found that predictions of both the gas and water vapor permeabilities of the three-layer films with respect to the volume fraction of PA-6, based upon those of the individual component layer films, can be made in good agreement with the experimental data when using a series model.

2. We employed a constitutive equation (equation A) to describe the tensile behavior of the films over the range of plastic deformation. The tensile behavior of the component layers and multilayer films at various crosshead speeds can be expressed precisely by using a constitutive equation that has three parameters in

the true stress–strain relationship: γ_M, m, and K.

3. We examined the relationships between the parameters of the monolayers of the component layers and those of the three-layer films by using an additive rule. By using this rule, we can also predict — with good agreements in the true stress–strain relationship — the tensile behavior of the three-layer film from that of each individual component, but a larger discrepancy exists between the modeled and experimental data at a high crosshead speed because heat is generated during the deformation process.

4. We also employed a simplified constitutive equation (equation B), which has two parameters, γ and σ_0, based on the equation A, to describe the tensile behavior of the films over the range of plastic deformation and to predict the parameters of the three-layer films from those of the monolayers of the component layers. The results are similar to those mentioned in point 3 above. The validity of the strain range for equation B (from 0.3 to 1.4), however, is much smaller than that for A (from 0.45 to 2.1).

5. In essence, we can efficiently design the compositions of a multilayer structure to achieve specific permeability and/or tensile properties by employing these model predictions before processing.

For the blend/EVOH/blend films

1. The adhesion of three-layer films, consisting of incompatible layers, can be improved by using blends of maleated low-density polyethylene and low-density polyethylene. This improvement arises as a result of ester bond formation, which we analyzed by FTIR spectroscopy.

2. The tensile strength does not change upon increasing the LDPE-g-MAH content, but it results in a slight increase in the elongation of both the MD and TD.

3. The modulus is increased only slightly at low levels of LDPE-g-MAH content, and remains almost constant in the MD and TD when the amount of LDPE-g-MAH is greater than 10 and 5 wt%, respectively.

4. The tear strengths in both the MD and TD decrease significantly upon increasing the LDPE-g-MAH content as a result of the greater ease of crack propagation in EVOH that is transferred to the entire three-layer film by the improved adhesion.

5. The oxygen permeabilities of the three-layer films follow an inverse additive rule upon varying the EVOH and LDPE-g-MAH contents.

6. The water vapor permeabilities of the three-layer films, however, do not follow this rule because increasing degrees of hydrogen bonding result in reduced permeability.

For the LDPE/EVOH blend films

1. In the LDPE/EVOH binary system, the EVOH domains have fibril-like structures at low levels of compatibilizer and are spherulite-like at high levels. When the amount of compatibilizer increases, the EVOH domains yield more and thinner EVOH layers, which result from the lower interfacial tension.

2. The melting and crystallization processes do not change significantly upon the addition of the compatibilizer because there is little or no constraint effect of the grafted EVOH (EVOH-g-LD).

3. There is a large difference in the heat of fusion between the first and second heating cycles. During the blown-film process, high and biaxial orientation leads to stress-induced crystallization. The processing and thermal history is faded during the DSC isothermal program prior to the second heating cycle, which results in a lower heat of fusion than in the first. There is also a difference in the cooling rates of the blown-film process and the DSC program. The cooling rate in

the DSC program (2°/min) is much slower than that in the blown-film process, and so the polymer chains of both LDPE and EVOH can crystallize more perfectly, which leads to higher melting temperatures.

4. Oxygen permeability of the LDPE/EVOH blend films is reduced slightly upon increasing the amount of compatibilizer, as a result of the presence of microvoids between the two phases. The microvoids, which form during cooling in the blown-film process, result in more gas being able to pass through the LDPE/EVOH blend films and, hence, they increase the oxygen permeability.

5. We found that there is an optimal level of compatibilizer content (1 phr) for maximizing the tensile strength and elongation in the MD. On the other hand, increasing the amount of compatibilizer results in an increase in the tensile strength and elongation in the TD. The trend of tear strength with respect to the amounts of compatibilizer is similar to that observed for the tensile strength.
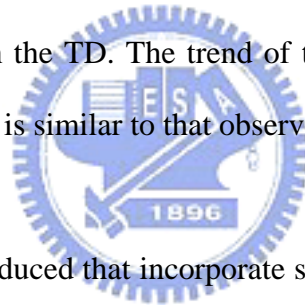
Laminar structures can be produced that incorporate several or tens of layers by using coextrusion and blending processes. In recent years, laminar structures that require hundreds or thousands of layers have been fabricated to produce unique properties. Among these properties are enhancements in mechanical, barrier, and optical properties. Microlayer technologies are being developed that use layer generators to produce laminar structures comprising hundreds or thousands of layers. In microlayer structures, the layers are very thin and this situation can easily lead to instability between each layer; such instability can result in the poor performance of the final product. Thus, technologies for the design of layer generators and for the control of processing conditions remain a significant challenge.

List of Publications

1. <u>Chi-Hsien Huang</u>, Jiann-Shing Wu, Chun-Chin Huang, and Li-Shin Lin, **"Adhesion, Permeability and Mechanical Properties of Multilayered Blown Films using Maleated Low-Density Polyethylene Blends as Adhesion-Promoting Layers"**, Polymer Journal, Vol. 35, No. 12, P. 978 (2003).

2. <u>Chi-Hsien Huang</u>, Jiann-Shing Wu, and Chun-Chin Huang, **"Predicting the Permeability and Tensile Properties of Multilayer Films from the Properties of the Individual Component Layers",** Polymer Journal, Vol. 36, No. 5, P. 1 (2004).

3. <u>Chi-Hsien Huang</u>, Jiann-Shing Wu, and Chun-Chin Huang, **"Morphological, Thermal, Barrier and Mechanical Properties of LDPE/EVOH Blends in Extruded Blown films"**, Journal of Polymer Research, Vol. 11, No. 1, P. 75 (2004).

4. <u>Chi-Hsien Huang</u>, Jiann-Shing Wu, and Chun-Chin Huang, **"Predicting the Permeability and Tensile Behavior of HDPE/tie/PA-6 Three-layer Films",** Polymer International, accepted.

5. <u>Chi-Hsien Huang</u>, Jiann-Shing Wu, and Chun-Chin Huang, **"Tensile Behavior of HDPE, PA-6 and HDPE/tie/PA-6 three-layer Films",** Polymer, submitted.

6. 黃俊欽，<u>黃啟賢</u>，"共擠押製程之界面探討"，第 24 屆中華民國高分子研討會論文專輯，高分子加工，民國 90 年。

7. 黃俊欽，<u>黃啟賢</u>，白方正，"PA/HDPE 雙層膜共擠押技術之研究"，第 25 屆中華民國高分子研討會論文專輯，高分子加工，民國 91 年。

8. 黃俊欽，<u>黃啟賢</u>，"共擠押成形之界面可視化探討"，第 25 屆中華民國高分子研討會論文專輯，高分子加工，民國 91 年。

9. 黃俊欽，<u>黃啟賢</u>，"微層共押技術及微米多層膜之特性研究"，第 26 屆中華民國高分子研討會論文專輯，高分子加工，民國 92 年。

Introduction to Author

Information

English Name: Chi-Hsien Huang

Chinese Name: 黃啟賢

Birthday: 6/24/1976

Address: 4F, No. 164-9, Zhongzheng Rd., Keelung 202, Taiwan, R. O. C.

Email: chhuang.ac87g@nctu.edu.tw

Education

1991.9-1994.6   Yan Ping High School, Taipei, Taiwan, R. O. C.

1994.9-1998.6   **B. E.**, Department of Chemical Engineering, National Tsing Hua University, Hsinchu, Taiwan, R. O. C.

1998.9-1999.6   **M. S.**, Department of Applied Chemistry, National Chiao Tung University, Hsinchu, Taiwan, R. O. C.

1999.9-2004.6   **Ph.D.**, Department of Applied Chemistry, National Chiao Tung University, Hsinchu, Taiwan, R. O. C.